

Contents

Introduction	1
1 Standard Model and Supersymmetry	2
1.1 The Standard Model	2
1.1.1 Quantum Field Theories	2
1.1.2 Fundamental interactions	3
1.1.3 The Higgs mechanism	7
1.2 The limitations of the Standard Model	11
1.2.1 The Higgs hierarchy problem	11
1.2.2 Dark matter	13
1.2.3 More open issues	13
1.3 Supersymmetry	15
1.3.1 Supersymmetric theories	16
1.3.2 The Minimal Supersymmetric Standard Model (MSSM)	18
1.3.3 SUSY as a solution to the hierarchy problem	23
1.3.4 SUSY models with spontaneous R -parity breaking	26
2 LHC and ATLAS	29
2.1 The Large Hadron Collider	29
2.1.1 Particle accelerators	30
2.1.2 Physics at hadron colliders	31
2.1.3 The purpose of the LHC	33

2.1.4	The CERN accelerator complex and the LHC	34
2.2	The LHC experiments	37
2.2.1	General-purpose experiments	39
2.3	The ATLAS detector	40
2.3.1	Coordinate system and event display	41
2.3.2	Magnet system	43
2.3.3	Inner Detector	44
2.3.4	Calorimeter system	47
2.3.5	Muon Spectrometer	51
2.3.6	Trigger and Data Acquisition	53
3	Event simulation and reconstruction	56
3.1	Monte Carlo simulation of ATLAS events	56
3.1.1	Simulation of physics processes	57
3.1.2	Monte Carlo generators	61
3.1.3	Detector simulation	62
3.2	Object reconstruction	62
3.2.1	Online trigger objects	63
3.2.2	Tracks and primary vertices	66
3.2.3	Electrons and photons	68
3.2.4	Muons	69
3.2.5	Jets	71
3.2.6	<i>b</i> -tagging	75
3.2.7	Missing transverse momentum	79
4	<i>b</i>-tagging performance studies with Monte Carlo simulations	81
4.1	Analysis strategy	81
4.1.1	Workflow and object definitions	82
4.1.2	Monte Carlo samples	83
4.1.3	Systematic uncertainties	84

4.2	Results on <i>b</i> -tagging performance	86
4.2.1	Nominal performance	87
4.2.2	Relation between <i>b</i> -hadron and <i>b</i> -jet momentum	88
4.2.3	Systematic uncertainties on <i>b</i> -tagging efficiency	91
4.2.4	Final remarks	93
5	Third generation SUSY searches in ATLAS	97
5.1	SUSY searches	98
5.1.1	Experimental challenges	98
5.1.2	Benchmark models	99
5.1.3	Phenomenology of third generation squarks	100
5.2	Backgrounds and Monte Carlo simulations	105
5.2.1	Background processes	106
5.2.2	Monte Carlo samples	108
5.3	Analysis strategy	110
5.3.1	Data sample and event selection	111
5.3.2	Object definition	113
5.3.3	Monte Carlo corrections	116
5.3.4	Systematic uncertainties	117
5.3.5	Signal Regions	121
5.3.6	Background estimation	122
5.4	Statistical analysis	124
5.4.1	Parameter estimation	125
5.4.2	Hypothesis testing	126
5.4.3	Standard fits in SUSY analyses	130
6	Search for bottom squarks with two-body RPC decays	131
6.0.1	Signal models	131
6.0.2	Discriminating variables	133
6.0.3	Data driven estimates of the <i>Z</i> background	138

7	Search for top squarks with RPV decays in b-ℓ pairs	139
8	Conclusions	140
A	Single electron trigger rate	141
B	Additional b-tagging efficiency plots	142

Introduction

blablabla.....

Chapter 1

Standard Model and Supersymmetry

This chapter provides a theoretical introduction to the physics topics discussed in the thesis. Section 1.1 presents the main features of the Standard Model of the elementary particles, while Section 1.2 is dedicated to a discussion of the open problems in particle physics that are calling for an extension of the theory. Supersymmetry is introduced in Section 1.3, which includes a discussion of the main motivations for light third generation squarks at the TeV scale.

1.1 The Standard Model

The Standard Model of the elementary particles is the theory that describes the phenomenology of fundamental fields and interactions. It includes all the particles that have been directly observed in high energy physics experiments, classifying them based on their mass, spin and interaction properties.

1.1.1 Quantum Field Theories

The Standard Model is a paradigm of a Quantum Field Theory (QFT), a major theoretical construction of the 20th century that unifies the principles of special relativity and quantum mechanics. Elementary particles are described as excitations of quantum fields embedded in a four-dimensional Minkowski spacetime, so they can be classified based on

their behaviour under Poincaré transformations: fermions are particles with half-integer spin, $\frac{1}{2}$ in units of \hbar , while bosons have integer spin, 0 for scalars and 1 for vectors. Another relevant property of the fields is their mass, that determines the propagation of the particles in the spacetime in absence of interactions.

The theory makes use of the Lagrangian formalism, where all the necessary information to derive the field dynamics is included in a Lagrangian density function \mathcal{L} :

$$\mathcal{L}_{tot} = \mathcal{L}_{free} + \mathcal{L}_{int} \quad (1.1)$$

In the above equation the full expression of \mathcal{L} is split into a kinetic term and an interaction term, which describe the spacetime evolution of the free fields and the way in which they are coupled.

1.1.2 Fundamental interactions

Once the spacetime properties of the fields are defined, the following step is to examine their interactions. At the present state of knowledge, any interaction observed in nature can be reduced to four fundamental forces: weak and strong interactions, electromagnetism and gravity. Among these only the latter is not included in the Standard Model, but its measured strength is extremely low compared to the others, so its impact is negligible in any realistic particle physics experiment.

As discussed in detail in Ref. [1], all the interaction terms of the Standard Model can be derived by imposing that the Lagrangian is invariant under special local transformations of the fields known as gauge transformations. When the field content of the theory is established, the choice of a particular gauge symmetry fixes the structure of the couplings between the fermions and new spin-1 vector fields, commonly referred to as gauge fields or mediators of the force. The new fields are introduced in order to preserve the invariance of the Lagrangian under the gauge transformation, so there is a direct correspondence between the imposed symmetry and the properties of the interaction. The full gauge symmetry group of the Standard Model is

$$SU(3)_C \otimes SU(2)_L \otimes U(1)_Y \quad (1.2)$$

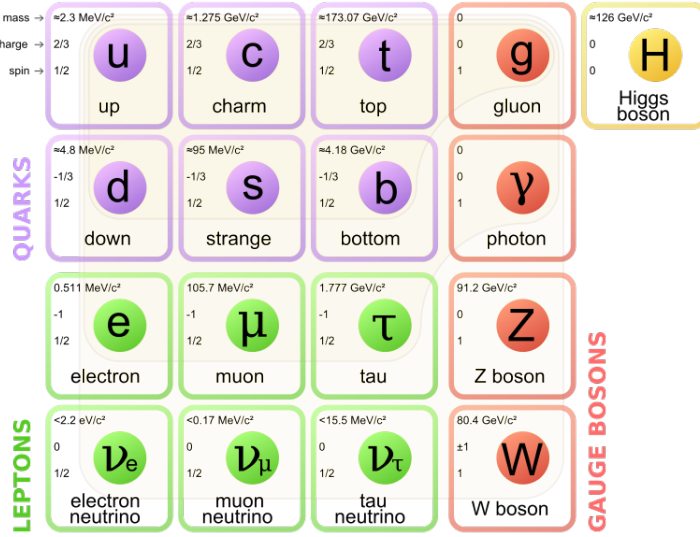


Figure 1.1: Elementary particles in the Standard Model.

where $SU(3)_C$ is the color symmetry of the strong interaction and $SU(2)_L \otimes U(1)_Y$ is the electroweak symmetry.

Having identified four fundamental forces allows to add an extra classification of the elementary fields. Fermions are referred to as leptons if they only interact via electromagnetic and weak (electroweak) force, while they are called quarks if they also experience the strong interaction. A crucial difference between the two types of objects, that emerges as a consequence of the different properties of electroweak and strong force, is that only elementary leptons can be observed as free particles, while quarks are always observed in bound states called hadrons. Hadrons are known as mesons if they are bosons, such as pions or kaons, while they are called baryons if they are fermions, with the most common examples being protons or neutrons. Figure 1.1 shows the presently known elementary particles of the Standard Model, classifying them in quarks, leptons, gauge bosons and an additional scalar boson, the Higgs.

Electroweak force

The first fundamental interaction described by the Standard Model is the electroweak force, which appears in the theory as a unified description of electromagnetic and weak

forces. The electroweak force is based on the $SU(2)_L \otimes U(1)_Y$ symmetry group [2–4] introduced by Glashow, Weinberg and Salam to combine the features of Quantum Electrodynamics (QED) and of a formal description of the Fermi theory of weak interactions where the $SU(2)_L$ structure had first emerged. The L of the $SU(2)_L$ group stands for *left*: only the left chiral components of the fermion fields (spinors) carry a weak isospin charge and therefore experience the weak interaction.

When the $SU(2)_L \otimes U(1)_Y$ symmetry is imposed in the Lagrangian four vector bosons are obtained: three W_i^μ bosons originating from the $SU(2)_L$ part and one B^μ boson originating from $U(1)_Y$. Mass eigenstates are then derived by mixing the four gauge bosons as follows:

$$\begin{aligned} W_\pm^\mu &= \frac{W_1^\mu \mp iW_2^\mu}{\sqrt{2}} \\ A^\mu &= B^\mu \cos \theta_W + W_3^\mu \sin \theta_W \\ Z^\mu &= W_3^\mu \cos \theta_W - B^\mu \sin \theta_W \end{aligned} \quad (1.3)$$

In the equations above the mediators of electromagnetic and weak interactions, the photon A , the Z and the two W^\pm bosons, appear as linear combinations of the eigenstates of $SU(2)_L$ and $U(1)_Y$. The last two rows contain a fundamental parameter of the Standard Model, the Weinberg angle θ_W , whose value has been accurately measured by various high energy physics experiments at different energy scales. In addition, to obtain the correct quantum numbers of each Standard Model particle, the hypercharge Y introduced in the $SU(2)_L \otimes U(1)_Y$ group needs to be related to the electric charge Q and the weak isospin T_3 through the Gell Mann-Nishijima equation:

$$Q = \frac{Y}{2} + T_3 \quad (1.4)$$

As extensively tested in the experiments, W^\pm bosons carry an electric charge of $Q = \pm 1$ and are only coupled to left handed fermions through their weak isospin charge T_3 . Z bosons are instead electrically neutral and couple differently to left and right handed fermions: for left handed fermions the coupling depends on both T_3 and Q , while for right handed fermions it is only proportional to Q .

Strong force

Together with the electroweak force, the Standard Model provides a full description of strong interactions. The corresponding field theory, Quantum Chromodynamics (QCD), is based on the $SU(3)_C$ symmetry group, which introduces eight vector boson mediators known as gluons [5]. The charge associated with the $SU(3)$ symmetry is the colour, C, and the elementary fermions that carry it are the quarks in Figure 1.1. Unlike photons in QED, gluons carry colour charge as a result of the non-abelian character of $SU(3)_C$. This implies that they are allowed to couple with each other, with significant impact on the phenomenological properties of the interaction.

The QCD Lagrangian and the masses of the quarks can be used to compute the scale evolution of the coupling constant α_s , that can be expressed as a function of the transferred energy μ :

$$\alpha_s(\mu^2) = \frac{12\pi}{(33 - 2n_f) \log\left(\frac{\mu^2}{\Lambda_{QCD}^2}\right)} \quad (1.5)$$

where n_f is the number of quarks with mass below μ and $\Lambda_{QCD} \sim 200$ MeV is a characteristic scale of the theory. When the quark content of the Standard Model is considered, equation 1.5 shows that the coupling constant α_s decreases as a function of the characteristic scale of the interactions. On the other hand, the coupling diverges rapidly when μ decreases and approaches Λ . This implies that the theory is only perturbative at high energy scales, because the necessary condition $\alpha_s \ll 1$ is only true for $\mu \gg \Lambda_{QCD}$. In addition, three more essential features of QCD emerge:

- *Asymptotic freedom*: $\alpha_s \rightarrow 0$ as $\mu \rightarrow \infty$, so in the high energy limit the strength of the interaction becomes negligible and quarks behave as free particles [6].
- *Confinement*: at low energies (or large distances) the coupling strength increases rapidly, keeping the quarks strongly bound to each other and implying that only colour singlet states can be observed as free particles.
- *Hadronisation*: when two coloured objects are split, the extraction of a new pair of hadrons from the vacuum soon becomes energetically preferable with respect to

a further increase in distance.

Hadronisation is responsible for the production of jets at high energy physics experiments, where quarks of gluons with high momentum form cascades of hadronic particles that terminate only when no more energy is left to extract more objects from the vacuum.

1.1.3 The Higgs mechanism

The theory of electroweak and strong interactions describes the experimental data with remarkable precision. However, a major limitation comes from the fact that its fundamental premises, gauge invariance and chiral symmetry, are not compatible with the presence of mass terms in the Lagrangian. If no extra feature is added, a Lagrangian with the interactions described in Section 1.1.2 predicts all the Standard Model particles to be massless, in clear contrast with the experimental evidence.

The problem of introducing the masses of the particles without spoiling gauge and chiral symmetries can be solved by a spontaneous symmetry breaking mechanism [7–9]. The idea is to postulate the existence of an electrically neutral scalar complex field, the Higgs field, whose interaction with the other particles is responsible for their masses. The Lagrangian is expanded with an additional term

$$\mathcal{L}_\phi = (D^\mu \phi)^\dagger (D_\mu \phi) - V(\phi^\dagger \phi) \quad (1.6)$$

where ϕ is the Higgs field, a weak isospin doublet with hypercharge $Y = 1$, and D_μ is the covariant derivative that contains the electroweak gauge fields W_i^μ and B^μ . The first component of ϕ has electric charge +1 while the second is neutral, and the full expression is given by

$$\phi = \begin{pmatrix} \phi^\dagger \\ \phi^0 \end{pmatrix} = \frac{1}{\sqrt{2}} \begin{pmatrix} \phi_1 + i\phi_2 \\ \phi_3 + i\phi_4 \end{pmatrix} \quad (1.7)$$

The term V in the Lagrangian 1.6 is the Higgs potential and has the form

$$V(\phi^\dagger \phi) = \mu^2 \phi^\dagger \phi + \lambda (\phi^\dagger \phi)^2 \quad (1.8)$$

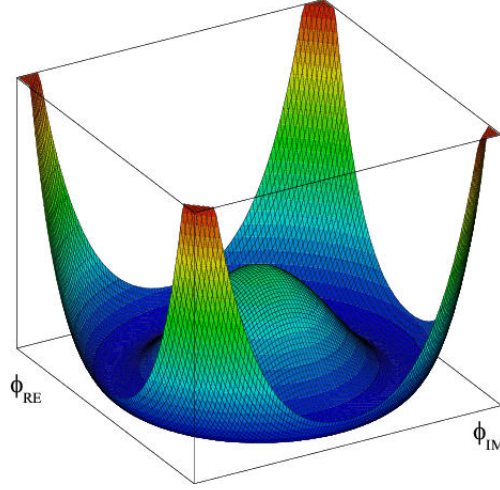


Figure 1.2: Shape of the Higgs potential for a one-dimensional complex field ϕ with $\lambda > 0$ and $\mu^2 < 0$.

where μ and λ are new parameters that identify a mass term and a self-interaction term of the field ϕ . The potential is symmetric under rotations in the ϕ space and its shape depends on the sign of the two parameters. When considering $\lambda > 0$ and $\mu^2 < 0$, a characteristic shape with a continuum of minima is obtained, as shown in Figure 1.2. Due to the form of the potential, the field is forced to select an arbitrary minimum that breaks the rotational (gauge) invariance. The conventional choice is $\langle \phi_3 \rangle = v$ and $\langle \phi_1 \rangle = \langle \phi_2 \rangle = \langle \phi_4 \rangle = 0$, where v is a parameter with the dimension of an energy known as the vacuum expectation value of the Higgs field:

$$v \equiv \sqrt{\frac{-\mu^2}{\lambda}} \quad (1.9)$$

The above choice allows to write a perturbation of the field ϕ around the minimum as

$$\phi = \frac{1}{\sqrt{2}} \begin{pmatrix} 0 \\ v + H(x) \end{pmatrix} \quad (1.10)$$

where three degrees of freedom are removed and the remaining one describes a scalar field with excitations around the vacuum expectation value v . If the expression 1.10 is used in the Lagrangian 1.6, the mass terms of the bosons appear from the expansion of

the covariant derivative D_μ coupled to the Higgs field, yielding:

$$m_W = \frac{gv}{2} \quad m_Z = \frac{v}{2} \sqrt{g^2 + g'^2} \quad m_A = 0 \quad (1.11)$$

where g and g' are the couplings strengths of the $SU(2)_L$ and $U(1)_Y$ groups, related to the Weinberg angle by

$$\sin(\theta_W) = \frac{g'}{\sqrt{g^2 + g'^2}} \quad (1.12)$$

It is interesting to notice that the spontaneous symmetry breaking mechanism is predicting a relation between the masses of W and Z bosons, $m_W = m_Z \cos(\theta_W)$, that is consistent with the experimental measurements.

Once the masses of the gauge bosons are established, the following step is to consider the case of the fermions. A mass term in its simplest form, $m\bar{\psi}\psi = m(\bar{\psi}_L\psi_R + \bar{\psi}_R\psi_L)$, is not gauge invariant because the left handed components of the fermions are $SU(2)_L$ doublets while the right handed components are singlets, so they transform in a different way. The solution is to introduce the Higgs field in the term as

$$\mathcal{L}_f = -\lambda_f(\bar{\psi}_L\phi\psi_R + \bar{\psi}_R\phi\psi_L) \quad (1.13)$$

where the gauge invariance is preserved thank to the presence of two $SU(2)$ doublets. In the case of leptons doublets, (ν_ℓ, ℓ) , the term can be rewritten using Higgs field expansion from Equation 1.10:

$$\begin{aligned} \mathcal{L}_\ell &= -\lambda_\ell \left[(\bar{\nu}_\ell \bar{\ell})_L \begin{pmatrix} 0 \\ v + H \end{pmatrix} \ell_R + \bar{\ell}_R (0, v + H) \begin{pmatrix} \nu_\ell \\ \ell \end{pmatrix}_L \right] \\ &= -\frac{\lambda_\ell v}{\sqrt{2}} \bar{\ell} \ell - \frac{\lambda_\ell H}{\sqrt{2}} \bar{\ell} \ell = -m_\ell \bar{\ell} \ell - \frac{m_\ell}{v} H \bar{\ell} \ell \end{aligned} \quad (1.14)$$

where the two terms that appear describe the mass of the leptons and their interaction with the Higgs, both related to the vacuum expectation value v and the Yukawa couplings λ_ℓ . Equation 1.13 can also be used for the masses of down-type quarks, but additional terms are needed for up-type quarks and possibly for neutrinos. The new terms can have the same structure of Equation 1.13, but they require the complex conjugate of the the

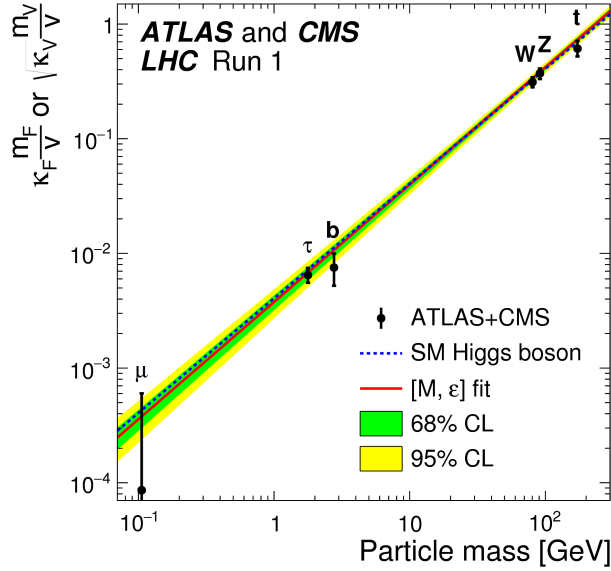


Figure 1.3: Strength of the Higgs boson couplings to the Standard Model particles as a function of their masses [10]. The linear fit shows that the measured values are consistent with the expectations within uncertainties.

Higgs field defined as

$$\phi_c \equiv -i\tau_2\phi^* = -\frac{1}{\sqrt{2}} \begin{pmatrix} v + H \\ 0 \end{pmatrix}$$

In summary, the spontaneous symmetry breaking mechanism is based on the introduction of a new Higgs field with four degrees of freedom, shown in Equation 1.7. Three degrees of freedom are then used to generate the mass terms of the W^\pm and Z bosons, as a result of the choice of vacuum (Equation 1.10). The remaining one appears as a new scalar, the Higgs boson, with Yukawa couplings to the Standard Model particles and with mass given by the quadratic term of the potential in Equation 1.8:

$$m_H^2 = 2\mu^2 = 2\lambda v^2 \quad (1.15)$$

The observation of the Higgs boson

The discovery of a new scalar particle with mass around 125 GeV, compatible with the properties of the Higgs boson, was announced by the ATLAS [11] and CMS [12] Collaborations on July 4th, 2012. Since then the Higgs has been measured in multiple decay channels, yielding no significant deviation with respect to the Standard Model predictions. The mass is now known with a precision of about 0.2% [13, 14] and the signal strength in the different channels is consistent with the predictions for Yukawa couplings, as shown by the combined ATLAS and CMS summary plot in Figure 1.3. The couplings are compatible with a linear fit over several orders of magnitudes, providing strong evidence of the validity of the electroweak symmetry breaking mechanism. The precision of the measurements is limited by the capabilities of the LHC experiments, where some decay channels are particularly challenging due to the combination of low signal cross section and large backgrounds. Improving their accuracy is a major goal of the experimental community, because any deviation with respect to the predictions would indicate the presence of new physics beyond the Standard Model.

1.2 The limitations of the Standard Model

The Standard Model provides an accurate and self-consistent description of fundamental interactions, extensively tested in high energy physics experiments. Despite its major successes, however, there are several reasons to believe that the present theory is not complete. This section describes the most compelling issues that call for an extension of the Standard Model, highlighting the problems related to the Higgs mass scale and the absence of a dark matter candidate.

1.2.1 The Higgs hierarchy problem

A major problem of the Standard Model arises from the large difference between the scale of the Higgs boson mass, 10^2 GeV, and the Planck scale, 10^{19} GeV, at which quantum gravity effects are expected to dominate with respect to the other interactions [15–17].

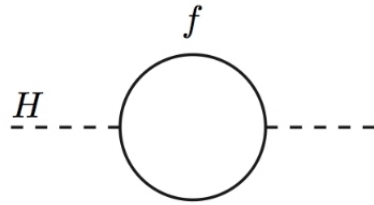


Figure 1.4: Fermion loop correction to the Higgs boson mass.

In the theory, the value of the Higgs boson mass can be computed as the sum of two components:

$$m_H^2 = m_{H_0}^2 + \delta m_H^2 \quad (1.16)$$

where m_{H_0} is the bare mass, a free parameter of the Lagrangian, and δm_H is a radiative correction that depends on the Higgs couplings to other particles. Due to the structure of the Yukawa couplings, it is easy to show that a major correction is given by the diagram in Figure 1.4, where a fermion loop is added to the Higgs propagator. For a fermion with coupling λ_f the size of the correction is given by

$$\delta m_H^2|_f = -\frac{|\lambda_f|}{8\pi^2} \Lambda_{\text{NP}}^2 + \dots \quad (1.17)$$

where Λ_{NP} is the highest mass scale in the theory. Due to the quadratic dependence on Λ_{NP} , the correction δm_H is strongly sensitive to any particle with mass beyond the electroweak scale. In particular, the reasonable assumption that new physics exists at the Planck scale implies that δm_H is of the order of 10^{19} GeV, pushing m_H far from the measured value of ~ 125 GeV. The only way to predict the value of m_H at the electroweak scale is to fine tune the bare parameter m_{H_0} in Equation 1.16 such that it almost perfectly cancels the large radiative correction. The Higgs mass is thus obtained as the difference between two terms of 10^{19} GeV each.

The large discrepancy between the measured scale of the Higgs boson mass and the Planck scale is known as the Higgs hierarchy problem. The Standard Model solution based on the tuning of m_{H_0} is in contrast with the argument of naturalness, according to which these fine cancellations should not occur unless they arise from a specific fea-

ture of the theory. For example, the light masses of fermions and vector bosons are not concerning because their value is protected by chiral and gauge symmetries, which imply that any radiative correction can only be proportional the mass itself ($\delta m_\psi \propto m_\psi$ and $\delta A^2 \propto A^2$). The case of the scalar Higgs boson is special because no symmetry is protecting the mass, which can then receive larger corrections as the one in Equation 1.17. A possible solution to the problem is to postulate the existence of an extra symmetry that provides a natural explanation to the discrepancy between the electroweak and Planck scales. This is what happens in supersymmetric extension of the Standard Model, as described in Section 1.3.3.

1.2.2 Dark matter

Astrophysical observations have identified a variety of systems where the amount of ordinary matter, estimated through the light that it emits, is incompatible with the gravitational pattern. These results suggest the presence of an extra type of matter, dark matter, that must contribute to the gravitational effects without yielding any extra luminosity [18]. To do so, dark matter particles need to be metastable or stable, massive, weakly interacting and electrically neutral. Since none of the Standard Model particles satisfy these criteria, the evidence of dark matter is a clear indication that the present theory is incomplete.

Searches for dark matter can be conducted in different ways, including collider experiments where the new particles may be produced in the final states of exotic physics processes. As described in Section 1.3, supersymmetric theories can embed dark matter candidates in many different ways, making them extremely interesting to search for at the LHC.

1.2.3 More open issues

Along with the hierarchy problem and the absence of a dark matter candidate, there is more evidence that motivates the need for physics beyond the Standard Model. In the

list below I briefly discuss some open issues that are being addressed by the scientific community:

- *Grand Unification*: Following the success of the electroweak theory, where weak force and electromagnetism are successfully described as the low energy limit of a single interaction, theorists have been exploring the possibility of a further unification that incorporates also the strong force. For this purpose, it is necessary to examine the evolution (*running*) of the coupling constants of each Standard Model interaction as a function of the energy scale [19]. As seen in Section 1.1.2 in the case of α_s (Equation 1.5), the value of the constants has a non-trivial dependence on the energy scale determined by the number of degrees of freedom of the theory. In the Standard Model, the evolution of the coupling constants of electromagnetic, weak and strong interactions is not converging to a common value, as shown by Figure 1.5a. This is in contrast with the idea of a unification of the interactions, that requires a unique coupling strength at a Grand Unification scale μ_{GUT} . The necessary behaviour can be recovered by introducing Supersymmetry, which varies the particle content of the theory and modifies the scale dependence of the constants such that the three curves can intersect (Figure 1.5b).
- *Neutrino sector*: The Standard Model predicts the existence of three types of massless neutrinos that can only convert into their corresponding charged lepton via electroweak interactions. However, the recent discovery of neutrino oscillations violates lepton flavour conservation and indicates that at least two of the three species must have non-zero mass [21]. Both these properties imply that the neutrino sector of the Standard Model is not complete, calling for a deeper understanding of the underlying physics.
- *CP violation*: In the Standard Model the only measured source of CP violation is a complex phase in the CKM matrix [22], which is not sufficient to explain the relative abundance of matter and antimatter in the universe [23]. In order to solve this puzzle, additional sources of CP violation are expected to appear in new physics

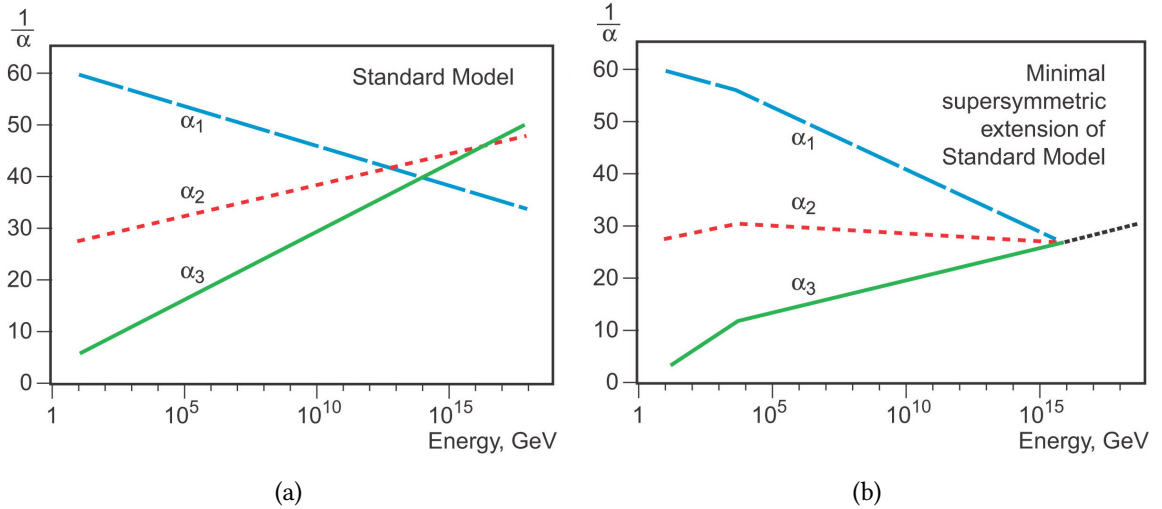


Figure 1.5: Evolution of the coupling constants of electromagnetic, weak and strong interactions as a function of energy in the Standard Model (a) and in a supersymmetric extension (b) [20].

scenarios.

- *Gravity:* As previously discussed in this chapter, no description of gravity is included in the Standard Model. The development of a quantum description of gravity is an ultimate goal of the scientific community.

1.3 Supersymmetry

This section provides an introduction to supersymmetric extensions of the Standard Model [24, 25], showing that they can solve many of the outstanding issues in high energy physics. The section begins with a theoretical introduction to supersymmetric Lagrangians, while in the second part the Minimal Supersymmetric Standard Model (MSSM) is introduced, highlighting the classes of models that are most relevant for this thesis.

1.3.1 Supersymmetric theories

Supersymmetry (SUSY) is a type of spacetime symmetry that extends the Poincaré group of the Standard Model with a new transformation between bosonic and fermionic states. In the Standard Model two distinct types of symmetry are implemented:

- *Spacetime symmetries*, that form the Poincaré group and cause the conservation of four-momentum and angular momentum.
- *Gauge symmetries* or *local symmetries*, that result in the conservation of the associated charges.

A fundamental theorem by Coleman and Mandula [26] states that local and spacetime symmetries can only be combined as direct products, as it happens in the Standard Model, otherwise the theory would be unable to predict scattering amplitudes with non-zero probability. This seems to imply that there is no way to introduce new hybrid types of symmetries, because the interactions between the fields would no longer be described. However, it can be shown that the Coleman-Mandula theorem does not apply to symmetries generated by fermionic transformations, where an operator Q acts on a state and modifies its spin by $\frac{1}{2}$. These special types of symmetries are known as supersymmetries, and the corresponding transformations are given by:

$$\begin{aligned} Q |\text{boson}\rangle &= |\text{fermion}\rangle \\ Q |\text{fermion}\rangle &= |\text{boson}\rangle \end{aligned} \tag{1.18}$$

The spin difference between the initial and final state of the transformation implies that the operator Q must be a spin- $\frac{1}{2}$ object. If we let Q_α ($\alpha = 1, 2$) and Q_β^\dagger be the components of the generator Q and of its hermitian conjugate Q^\dagger , their anticommutator is given by

$$\{Q_\alpha, Q_\beta^\dagger\} = 2\gamma_{\alpha\beta}^\mu p_\mu \tag{1.19}$$

where p_μ is the Lorentz four-momentum and γ^μ are the Dirac matrices. Other important commutators are:

$$\begin{aligned} [M^{\rho\sigma}, Q_\alpha] &= -i(\sigma^{\rho\sigma})_\alpha^\beta Q_\beta \\ \{Q_\alpha, Q_\beta\} &= \{Q_\alpha^\dagger, Q_\beta^\dagger\} = 0 \\ [p^\mu, Q_\alpha] &= [p^\mu, Q_\alpha^\dagger] = 0 \end{aligned} \quad (1.20)$$

where $M^{\rho\sigma}$ is the generator of the Lorentz transformations. From the last line it can be seen that the generator Q commutes with $p^2 = m^2$, which implies that fermion-boson pairs related by the transformation have the same mass. In supersymmetric extensions of the Standard Model the commutators of Q with the generators of the gauge transformations must also vanish, in order to preserve the existing structure of the theory. Fermions and bosons related by Q must then have the same $SU(3)_C \otimes SU(2)_L \otimes U(1)_Y$ quantum numbers, which is not the case for any pair of particles in the Standard Model, indicating that none of the known objects can be regarded as the superpartner of any other. Since supersymmetry needs to apply to all fields in the theory, it follows that minimal extensions of the Standard Model require the introduction of a new superpartner for each particle, incrementing the number of elementary states by at least a factor 2.

Superfields

The Standard Model particles and their superpartners are organised in supermultiplets that contain two bosonic and two fermionic degrees of freedom. The fermions are described by Weyl spinors [27] with two polarisations, and for each of them there is a corresponding bosonic state. When the operators Q and Q^\dagger act on the supermultiplets, they transform the bosonic components into the fermionic ones and vice versa. Depending on the spin of the particles involved, the supermultiplets can be classified as follows:

- *Chiral supermultiplets* contain spin- $\frac{1}{2}$ fermions with left and right handed components, f_L and f_R , and two spin-0 partners known as scalar fermions or sfermions. The two scalars are conventionally labelled \tilde{f}_L and \tilde{f}_R , where the tilde is used to

identify SUSY particles and the L and R labels are referred to the chirality of the partners.

- *Gauge supermultiplets* contain vector bosons, assumed to be massless, and two spin- $\frac{1}{2}$ Weyl fermions known as gauginos.
- *Gravitational supermultiplets* include the spin-2 graviton and a spin- $\frac{3}{2}$ partner, the gravitino.

1.3.2 The Minimal Supersymmetric Standard Model (MSSM)

This paragraph describes the simplest supersymmetric extension of the Standard Model, known as Minimal Supersymmetric Standard Model (MSSM), where a new superpartner is added for each standard particle. The MSSM preserves the $SU(3)_C \otimes SU(2)_L \otimes U(1)_Y$ gauge symmetry of the Lagrangian, so the quantum numbers of particles and superpartners are the same. The field content of the theory is the following:

- A chiral supermultiplet $q_{L,R}-\tilde{q}_{L,R}$ for each quark in the Standard Model.
- A chiral supermultiplet $\ell_{L,R}-\tilde{\ell}_{L,R}$ for each lepton family.
- A gauge supermultiplet for each vector boson in the Standard Model and its spin- $\frac{1}{2}$ partner: $B_0-\tilde{B}_0$, $W_i-\tilde{W}_i$, $g-\tilde{g}$.
- Two chiral supermultiplets, $H_u-\tilde{H}_u$ and $H_d-\tilde{H}_d$, that embed the Standard Model Higgs and give mass to bosons and fermions through the usual spontaneous symmetry breaking mechanism. Among the total of eight degrees of freedom only three are involved in the symmetry breaking, so the remaining five can appear as observable states:
 - H^\pm : two charged Higgs states.
 - A^0 : a CP-odd neutral Higgs.
 - h^0 and H^0 : two neutral CP-even Higgs fields, one of which must be the Standard Model Higgs boson.

SUSY Lagrangian and R -parity

Once the field content is defined it is possible to examine the most general expression of the SUSY Lagrangian, that contains a larger number of terms with respect to the Standard Model. Some of these terms violate the conservation of lepton and baryon number, which is instead prohibited in the Standard Model, so they enable processes like proton decay that are heavily constrained by experimental data. In order to remove them from the SUSY Lagrangian, a solution is to introduce a new quantum number known as R -parity [28] that can be expressed as a function of baryon and lepton numbers, B and L , and of the spin S :

$$P_R \equiv (-1)^{3(B-L)+2S}. \quad (1.21)$$

With the above definition, R -parity provides a simple classification of the particles:

- Standard Model particles $\rightarrow P_R = 1$
- SUSY particles $\rightarrow P_R = -1$

In SUSY models where R -Parity is conserved, the Lagrangian terms that violate lepton and baryon number are automatically forbidden. The structure of the remaining terms implies that any Feynman diagram must only include vertices with an even number of SUSY particles, with relevant consequences on the phenomenology:

- SUSY particles must be produced in pairs.
- The decay of a SUSY particle must contain an odd number of SUSY particles.
- The Lightest Supersymmetric Particle (LSP) must be stable.

SUSY breaking

As seen in Section 1.3.1, supersymmetric extensions of the Standard Model require that particles and superpartners are mass-degenerate. This is clearly incompatible with the experimental data, because so far no evidence of SUSY particles has been found. The lack of observations indicates that SUSY, if it exist, must be broken in a way that makes

the superpartners significantly heavier than the Standard Model particles.

In the absence of experimental hints, the mechanism responsible for SUSY breaking can only be guessed based of generic arguments. As discussed in Ref. [29], a spontaneous breaking is not possible within the framework of the MSSM without the introduction of at least one extra field, with little or no indication about its properties. For this reason, a standard approach is to keep the field content of the theory to the minimum and introduce extra terms that break the symmetry explicitly, obtaining a Lagrangian of the form:

$$\mathcal{L} = \mathcal{L}_{\text{SUSY}} + \mathcal{L}_{\text{soft}} \quad (1.22)$$

where the *soft* label indicates that the new terms must not spoil the renormalisability of the theory, and should be regarded as a perturbation of the supersymmetric part of the Lagrangian. In practice, the soft term is parametrising our ignorance about the exact mechanism responsible for the SUSY breaking, describing its consequences without specifying its origin. The inclusion of the soft term increases the number of free parameters of the theory to 105 in addition to the ones of the Standard Model. The phenomenology is strongly dependent on them, so it is common to classify the different models based on assumptions about their values.

Mass eigenstates

As a result of the SUSY breaking, the masses of the superpartners become free parameters and can be different from those of the Standard Model particles. SUSY particles with the same quantum numbers can also mix, so the mass eigenstates are not necessarily the same as the interaction eigenstates introduced in the previous paragraph. The list below provides an overview of the mass eigenstates in the MSSM, that are also summarised in Table 1.1:

Sleptons and squarks Contrarily to what happens for standard particles, the left and right handed superpartners of quarks and leptons are not constrained to have equal mass. It is hence possible to define a mixing matrix that rotates the interactions

eigenstates \tilde{q}_L - \tilde{q}_R into mass eigenstates \tilde{q}_1 - \tilde{q}_2 , where by convention \tilde{q}_1 is the lightest. The structure of the mixing matrices is similar for squark and sleptons, and its expression in the case of third generation squarks [30] is given by:

$$\mathcal{M}_{\tilde{q}}^2 = \begin{pmatrix} m_{\tilde{q}_L}^2 & a_q m_q \\ a_q m_q & m_{\tilde{q}_R}^2 \end{pmatrix} \quad (1.23)$$

with

$$m_{\tilde{q}_L}^2 = M_{Q_3}^2 + m_Z^2 \cos 2\beta (I_3^{qL} - e_q \sin^2 \theta_W) + m_q^2, \quad (1.24)$$

$$m_{\tilde{q}_R}^2 = M_{\{U,D\}_3}^2 + m_Z^2 \cos 2\beta e_q \sin^2 \theta_W + m_q^2, \quad (1.25)$$

$$a_q m_q = \begin{cases} (A_t - \mu \cot \beta) m_t & (\tilde{q} = \tilde{t}) \\ (A_b - \mu \tan \beta) m_b & (\tilde{q} = \tilde{b}) \end{cases} \quad (1.26)$$

In the above equations I_3^q is the third component of the weak isospin, e_q the fractional electric charge of the quark q and m_Z is the mass of the Standard Model Z boson. In addition, μ is the higgsino mass parameter in the MSSM and $\tan \beta$ is the ratio between the vacuum expectation values of H_u and H_d . The remaining parameters are introduced in $\mathcal{L}_{\text{soft}}$: M_{Q_3, U_3, D_3} are the third components of the mass matrices of left and right handed squarks, corresponding to the third generation, while $A_{t,b}$ are the coefficients of their trilinear coupling terms. The impact of the mixing is particularly relevant for the partners of the heavy flavour families, stop ($\tilde{t}_{1,2}$) and sbottom ($\tilde{b}_{1,2}$), due to the presence of the mass of the Standard Model fermions in the off-diagonal terms of the matrix.

Gluinos Since gluons and gluinos carry colour charge, no mixing can occur and the mass eigenstates correspond to the interaction eigenstates.

Neutralinos and charginos The charged Higgs states mix with the superpartners of the gauge bosons, the gauginos, yielding two pairs of positively or negatively charged spin- $\frac{1}{2}$ mass eigenstates known as charginos, $\tilde{\chi}^\pm$. The mixing matrix is

$$\begin{pmatrix} M_2 & \sqrt{2}m_W \sin \beta \\ \sqrt{2}m_W \cos \beta & \mu \end{pmatrix} \quad (1.27)$$

Names	Spin	P_R	Gauge Eigenstates	Mass Eigenstates
Higgs bosons	0	+1	$H_u^0 \ H_d^0 \ H_u^+ \ H_d^-$	$h^0 \ H^0 \ A^0 \ H^\pm$
squarks	0	-1	$\tilde{u}_L \ \tilde{u}_R \ \tilde{d}_L \ \tilde{d}_R$ $\tilde{s}_L \ \tilde{s}_R \ \tilde{c}_L \ \tilde{c}_R$ $\tilde{t}_L \ \tilde{t}_R \ \tilde{b}_L \ \tilde{b}_R$	(same) (same) $\tilde{t}_1 \ \tilde{t}_2 \ \tilde{b}_1 \ \tilde{b}_2$
sleptons	0	-1	$\tilde{e}_L \ \tilde{e}_R \ \tilde{\nu}_e$ $\tilde{\mu}_L \ \tilde{\mu}_R \ \tilde{\nu}_\mu$ $\tilde{\tau}_L \ \tilde{\tau}_R \ \tilde{\nu}_\tau$	(same) (same) $\tilde{\tau}_1 \ \tilde{\tau}_2 \ \tilde{\nu}_\tau$
neutralinos	1/2	-1	$\tilde{B}^0 \ \tilde{W}^0 \ \tilde{H}_u^0 \ \tilde{H}_d^0$	$\tilde{N}_1 \ \tilde{N}_2 \ \tilde{N}_3 \ \tilde{N}_4$
charginos	1/2	-1	$\tilde{W}^\pm \ \tilde{H}_u^\pm \ \tilde{H}_d^\pm$	$\tilde{C}_1^\pm \ \tilde{C}_2^\pm$
gluino	1/2	-1	\tilde{g}	(same)

Table 1.1: Particle content of the Minimal Supersymmetric Standard Model [31].

in the (W^\pm, H^\pm) basis, where M_1 and M_2 are gaugino mass parameters from $\mathcal{L}_{\text{soft}}$, m_W is the mass of the W boson, and β and μ are defined as in Equations 1.23-1.26. In a similar way, four neutral spin- $\frac{1}{2}$ particles called neutralinos ($\tilde{\chi}_i^0$ with $i = 1, 2, 3, 4$) result from the mixing of the charge-neutral interaction eigenstates from the Higgs and gauge sectors. The 4×4 mixing matrix in the (B, W^0, H_d, H_u) basis is

$$\begin{pmatrix} M_1 & 0 & -m_Z \cos \beta \sin \theta_W & m_Z \sin \beta \sin \theta_W \\ 0 & M_2 & m_Z \cos \beta \cos \theta_W & m_Z \sin \beta \cos \theta_W \\ -m_Z \cos \beta \sin \theta_W & m_Z \cos \beta \cos \theta_W & 0 & \mu \\ m_Z \sin \beta \sin \theta_W & -m_Z \sin \beta \cos \theta_W & -\mu & 0 \end{pmatrix} \quad (1.28)$$

where the same parameters of the previously defined matrices are appearing.

Phenomenological MSSM

The number of free parameters in the MSSM after SUSY breaking can be reduced under the following assumptions:

- The only source of CP violation in the theory is the Cabibbo-Kobayashi-Maskawa (CKM) matrix.
- No flavour changing neutral currents exist at tree level, implying that the sfermion mass matrices and trilinear coupling matrices must be diagonal.
- Universality applies to the first and second generation of the sfermions, whose masses are assumed to be degenerate.

As a result, the free parameters of the theory can be reduced to 19: the ratio $\tan \beta$ between the VEVs of the two Higgs doublets, the mass of the pseudoscalar Higgs M_A , the Higgs-Higgsino mass parameter μ , five mass parameters for 1st and 2nd generation sfermions and five more for 3rd generation sfermions, three mass parameters for gluino, Bino and Wino and three more parameters for third generation trilinear couplings. This simplified version of the theory is known as phenomenological Minimal Supersymmetric Standard Model, pMSSM.

1.3.3 SUSY as a solution to the hierarchy problem

The MSSM can address many of the outstanding issues of the Standard Model, including the Higgs hierarchy problem [32]. As discussed in Section 1.2.1, the problem originates from the divergent radiative corrections to the Higgs mass shown in Figure 1.4, that make the value of m_H extremely sensitive to any new physics at high energy scales. Supersymmetry introduces additional loops [31] involving the scalar partners of the fermions, as the one in Figure 1.6, so an extra radiative correction appears for both right and left handed superpartners:

$$\delta m_H^2|_s = +\frac{|\lambda_s|}{16\pi^2} \Lambda_{\text{NP}}^2 + \dots \quad (1.29)$$

where $\lambda_s \equiv \lambda_f$ is the Yukawa coupling of the sfermions to the Higgs. Thanks to the fact that the couplings are the same, the two scalar contributions cancel exactly the divergent correction caused by the fermion loop, whose expression is defined in Equation 1.17. This implies that even hypothetical fermions with mass of the order of the Planck scale would not have an impact on the Higgs mass, so the measured value $m_H \sim 125$ GeV can be obtained without any unnatural tuning of the parameters. In other words, supersymmetry is forcing λ_f and λ_s to be the same and, by doing so, it is removing the quadratic divergence in Λ_{NP} .

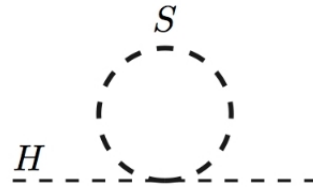


Figure 1.6: Scalar loop correction to the Higgs mass that cancels the fermion loop in Figure 1.4.

At higher order in perturbation theory, it can be shown that both fermions and scalars coupled to the Higgs yield corrections of the form:

$$\delta m_H^2|_X = \pm \frac{\lambda_X}{16\pi^2} m_X^2 \log \left(\frac{\Lambda_{\text{NP}}}{m_X^2} \right) + \dots, \quad X = f, s \quad (1.30)$$

where there Λ_{NP} appears in a logarithm but a quadratic dependence on the mass is introduced, and the sign is again opposite for scalars and fermions. In realistic models where SUSY is broken the above terms do not cancel, yielding a non-zero correction to the Higgs mass due to the mass difference between the standard particles and their partners:

$$\delta m_H^2|_{s+f} = \frac{\lambda}{16\pi^2} \left[m_f^2 \log \left(\frac{\Lambda_{\text{NP}}}{m_f^2} \right) - m_s^2 \log \left(\frac{\Lambda_{\text{NP}}}{m_s^2} \right) \right] \quad (1.31)$$

In order to keep the size of the correction under control, the difference between the masses of standard and SUSY particles with large couplings λ to the Higgs must not be too large. The exact threshold on the mass difference is arbitrary, and is determined by

the amount of fine tuning that one is willing to accept without regarding the model as unnatural.

In the case of the top quark and its partner, the stop (\tilde{t}), the correction in Equation 1.31 can be expressed as a function of the parameters of $\mathcal{L}_{\text{soft}}$ [33]:

$$\delta m_H^2|_{\text{stop}} \simeq -\frac{3y_t^2}{8\pi^2} (m_{Q_3}^2 + m_{U_3}^2 + |A_t|^2) \log\left(\frac{\Lambda_{\text{NP}}}{\text{TeV}}\right) \quad (1.32)$$

where m_{Q_3} and m_{U_3} are the third components of the mass matrices of left and right squarks and the trilinear coupling coefficient, as introduced in Equations 1.23-1.26, and the dependence on the mass in the logarithm is neglected.

In the MSSM, an even stronger constraint is placed on the Higgsino mass parameter μ , which is related to the Higgs mass at tree level and therefore should be close to the measured value of m_H :

$$\frac{m_H^2}{2} = -|\mu|^2 + \dots + \delta m_H^2 \quad (1.33)$$

Finally, the gluino mass parameter M_3 is also constrained because it enters a 2-loop correction to the Higgs mass at 2-loop level:

$$\delta m_H^2|_{\text{gluino}} \simeq -\frac{2y_t^2}{\pi^2} \left(\frac{\alpha_s}{\pi}\right) |M_3|^2 \log^2\left(\frac{\Lambda_{\text{NP}}}{\text{TeV}}\right) \quad (1.34)$$

The above arguments can be used to classify the mass eigenstates of the pMSSM. Higgsinos, third generation squarks and gluinos form the natural SUSY spectrum, while the rest of the sparticles can in principle be heavier without spoiling the naturalness of the theory, so they are referred to as decoupled SUSY.

The full spectrum of a natural pMSSM model is shown in Figure 1.7. If the μ parameter in the mixing matrices of charginos and neutralinos (Equations 1.27-1.28) is assumed to be significantly smaller than the others, three light Higgsino-like mass eigenstates are predicted. Due to the structure of the squark mixing matrix (Equation 1.23) the constraints on m_{Q_3} m_{U_3} imply that the left handed third generation squarks and the right handed \tilde{t} must also be light, with favoured decays into Standard Model top or bottom quarks plus one of the three Higgsinos. Gluinos are light because of the constraint on M_3 , while the lightest Higgsino is assumed to be the LSP and provides a good candidate for dark matter.

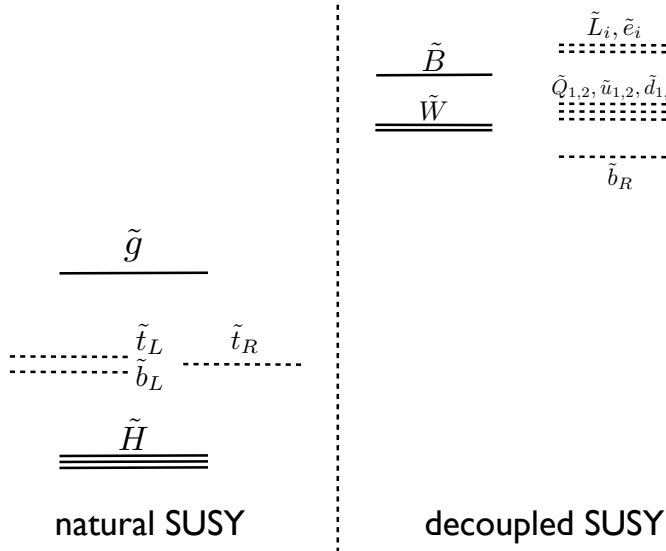


Figure 1.7: Natural pMSSM mass spectrum [33]. The particles on the left side are constrained by naturalness arguments, while the remaining ones are decoupled.

1.3.4 SUSY models with spontaneous R -parity breaking

The imposition of R -parity, as described in Section 1.3.2, is an *ad-hoc* adjustment to the theory which is needed to remove unwanted terms from the Lagrangian. A formal way to embed it in the MSSM is to enlarge the gauge symmetry group to $SU(3)_C \otimes SU(2)_L \otimes U(1)_Y \otimes U(1)_{B-L}$, where the additional $U(1)_{B-L}$ group naturally includes R -parity conservation. The caveat is that the $U(1)_{B-L}$ symmetry is not observed at the electroweak scale, so a breaking mechanism must be assumed and RPV terms can appear as a consequence.

A minimal way to break $U(1)_{B-L}$ spontaneously, without spoiling experimental constraints such as the limits on the proton decay, is to assume that right-handed scalar neutrinos (sneutrinos) develop a non-zero vacuum expectation value (VEV) [34]. This gives rise to a class of models that can be referred to as minimal $B - L$ MSSM, with at least three major phenomenological features:

- The introduction of RPV terms implies that the Lightest Supersymmetric Particle

(LSP) can carry colour or electric charge without causing a conflict with astrophysical data, because a prompt decay into Standard Model particles is possible.

- Since the spontaneous breaking of $U(1)_{B-L}$ happens through the VEV of right handed neutrinos, the branching ratio of the LSP decays can be directly related to the neutrino mass hierarchy and to the value of the mixing angle θ_{23} .
- Once the LSP is chosen, its decays are fixed by the theory as a result of the coupling structure of the minimal MSSM.

The nature of the LSP is not determined by the properties of the minimal $B - L$ MSSM, but the distinctive trait of the theory is that it allows such particle to be colour charged. It can be shown that gluinos cannot be LSPs without spoiling the unification of gauge coupling parameters, so the most interesting LSP candidates to examine are the squarks. Moreover, third generation squarks are well motivated to be lighter than the others, so it is reasonable to focus the attention on the stop and sbottom. Considering the case of the stop, the decay is determined by the structure of the MSSM couplings:

$$\tilde{t}_1 \rightarrow b\ell, \quad \ell = e, \mu, \tau \quad (1.35)$$

and the branching ratios into electrons, muons and τ leptons depend on the many parameters of the theory.

As anticipated, it is possible to correlate the branching ratio of the stop decay with the neutrino mass hierarchy and the mixing parameter $\sin^2(\theta_{23})$. Figure 1.8 from Ref. [34] shows a full scan of the branching ratios in the $\text{BR}(e)$ - $\text{BR}(\tau)$ plane as a function of the free parameters of the theory, for given neutrino mass hierarchies and for $\sin^2(\theta_{23}) = 0.446$ or $\sin^2(\theta_{23}) = 0.587$. Interestingly, this implies that the experimental measurement of the branching ratio of a stop LSP within the minimal $B - L$ MSSM would provide useful information to discriminate between the neutrino mass hierarchies and the two possible values of $\sin^2(\theta_{23})$.

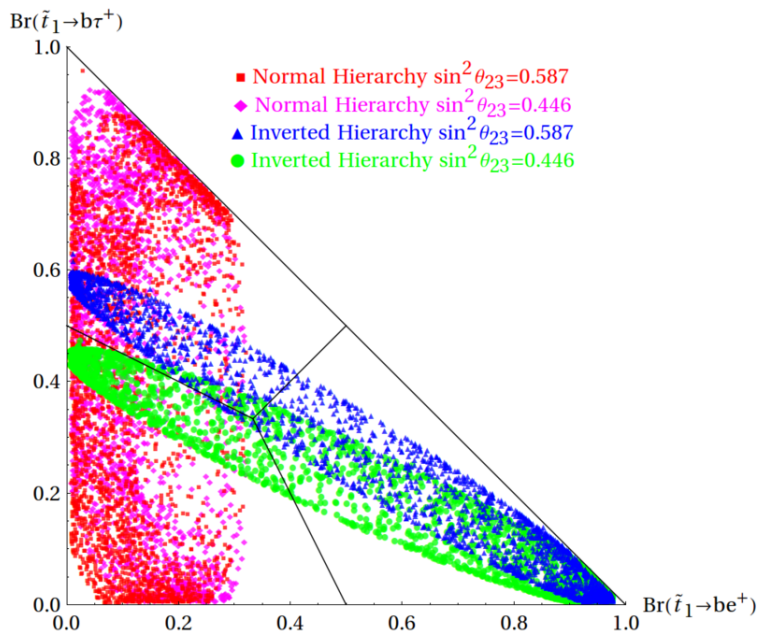


Figure 1.8: Scan of the branching ratio of the stop decay into $b-e$, $b-\mu$ and $b-\tau$ as a function of free parameters of the minimal $B - L$ MSSM, for a fixed mass hierarchy and for a fixed value of $\sin^2(\theta_{23})$. The scan parameters in the plot include the mass of the \tilde{t}_1 , ranging from 400 GeV to 1 TeV. The values of $\sin^2(\theta_{23})$ are taken from NuFIT-v1.2 [35].

Chapter 2

LHC and ATLAS

This thesis focuses on the analysis of proton-proton collisions delivered by the LHC accelerator [36] at CERN during the 2015 and 2016 operation at $\sqrt{s} = 13$ TeV, and recorded by the ATLAS detector [37]. This chapter provides an overview of the experimental setup, starting from a discussion of the CERN accelerator complex (Section 2.1) and continuing with a description of ATLAS and its components (Section 2.3).

2.1 The Large Hadron Collider

The European Organisation for Nuclear Research (CERN) hosts the largest particle accelerator in the world, the Large Hadron Collider (LHC), in a 27 km long underground tunnel situated at the border between Switzerland and France. The LHC is able to accelerate two beams of protons in opposite direction, delivering collisions at a maximum centre of mass energy $\sqrt{s} = 14$ TeV¹. The collisions take place in four interaction points, where particle physics detectors are employed to reveal and measure the fundamental physics processes that take place.

¹The design energy $\sqrt{s} = 14$ TeV has not been reached yet due to technical limitations. In the data taking period relevant for this thesis, the LHC operated at $\sqrt{s} = 13$ TeV.

2.1.1 Particle accelerators

In a circular collider, the trajectory of the beams is maintained by an array of dipole magnets that produce a bending field orthogonal to their direction of motion. The relativistic relation

$$p = 0.3BR \quad (2.1)$$

expresses the momentum p of the particles (in GeV) as a function of the magnetic field B (in Tesla) and the radius R of the accelerator (in meters). The rate of physics collisions delivered by the accelerator is measured by the instantaneous luminosity:

$$\mathcal{L}_{\text{inst}} \equiv \frac{1}{\sigma} \frac{dN}{dt} \quad (2.2)$$

where dN/dt is the rate of occurrence of a benchmark physics process and σ is its total cross section. The instantaneous luminosity is measured in inverse barn per second ($b^{-1}s^{-1}$ where $1 b \equiv 10^{-24} \text{ cm}^2$) and its value is independent of the particular process considered, so it can be expressed as a function of beam parameters:

$$\mathcal{L}_{\text{inst}} = f \frac{n_1 n_2}{4\pi\sigma_x\sigma_y}. \quad (2.3)$$

In the above expression f is the revolution frequency, n_1 and n_2 are the numbers of particles in the colliding bunches and $4\pi\sigma_x\sigma_y$ is their transverse area at the interaction point, described by the gaussian widths σ_x and σ_y . The total amount of data delivered by the accelerator is given by the integrated luminosity:

$$\mathcal{L}_{\text{tot}} = \int_{t_1}^{t_2} \mathcal{L}_{\text{inst}} dt \quad (2.4)$$

with integral taken over the relevant period of operation. One of the advantages of circular colliders is that the beams are kept in their trajectory for long periods of time, so the individual proton bunches can be repeatedly used for collisions instead of decelerating them after a single crossing.

The main limitation of circular colliders is the synchrotron radiation that charged particles emit when they experience transverse acceleration. The associated rate of energy loss can be expressed as

$$\frac{dE}{dt} = k \frac{E^4}{m^4 R^2} \quad (2.5)$$

where k is a dimensional constant, m is the mass of the accelerated particles and R is the radius of curvature of their trajectory. Since it is inversely proportional to m^4 , the energy loss is extremely significant for light particles such as electrons or positrons, while for protons it is reduced by a factor $(m_e/m_p)^4 \sim 10^{-12}$. At electron-positron circular colliders, synchrotron radiation is the main effect that determines the maximum energy reach. Hadron colliders are less affected by this phenomenon, and the limiting factor for their energy is the maximum magnetic field that can be produced by the bending magnets.

2.1.2 Physics at hadron colliders

In general, circular accelerators are designed to provide head-on collisions of two beams with equal energy E . If the colliding particles are elementary (i.e. they have no internal sub-structure) the centre of mass frame of the interactions corresponds to the laboratory frame, so the total energy of the collisions is simply given by $\sqrt{s} = 2E$. This is the case at electron-positron colliders but not at hadron colliders, where the physics processes of interest are produced by the scattering of individual partons (quarks or gluons) that carry an unknown fraction x_1 and x_2 of the hadron momentum [38]. A scheme of a hard scattering process at a hadron collider is given in Figure 2.1, where all the main elements are highlighted. In each collision, the partonic centre of mass energy $\sqrt{\hat{s}}$ is smaller than the energy of the full hadron-hadron system \sqrt{s} , and can be expressed as:

$$\sqrt{\hat{s}} = x_1 x_2 \sqrt{s}, \quad (2.6)$$

where x_1 and x_2 vary on an event-by-event basis following probability density functions $f_i(x_1, Q^2)$ and $f_j(x_2, Q^2)$. These quantities, known as parton distribution functions (PDFs), are measured by fitting dedicated experimental observables to collision data from various physics processes at different energy scales [39]. The total cross section of a generic physics process $ij \rightarrow X$ can be expressed as:

$$\sigma_{ij} = \int dx_1 dx_2 f_i(x_1, Q^2) f_j(x_2, Q^2) \hat{\sigma}_{ij \rightarrow X}, \quad (2.7)$$

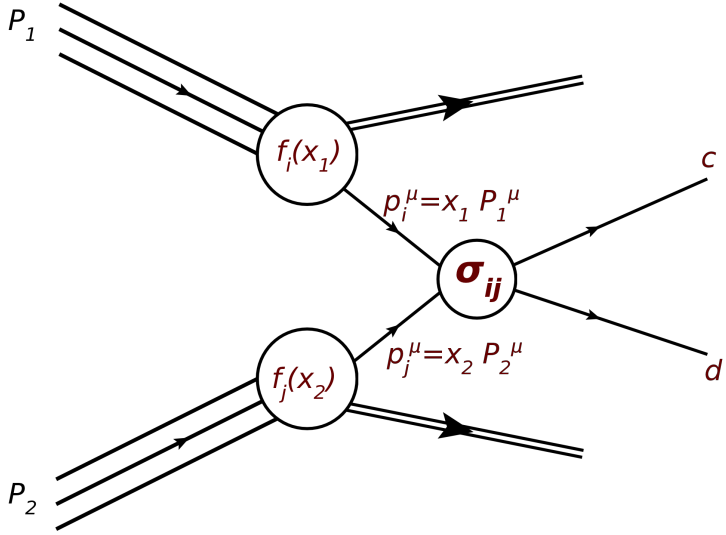


Figure 2.1: Hard scattering process involving two partons i and j whose momenta p_i and p_j are a fraction x_1 and x_2 of the total momenta of the protons. [40]

where the contribution of the PDFs and the partonic cross section $\hat{\sigma}$ are factorised.

It should be noted that, since x_1 and x_2 can have different values, the physics objects X produced by the hard interaction carry an unknown boost in the direction of the beam axis. In addition, the final state contains extra objects produced by the partons that are not involved in the hard scattering, characterised by low transverse momentum and small production angles with respect to the beam. These underlying objects are a major source of background at hadron colliders.

Underlying hadronic activity in the events can also be generated by proton-proton collisions where no hard scattering takes place. From a comparison between the total cross sections of inelastic collisions and of any other Standard Model process (see Figure 5.2) it follows that the majority of the interactions yield only soft hadronic objects in the final state, while the hard scattering happens at lower rates. For every crossing between proton bunches, it is possible to compute the average number of interactions $\langle \mu \rangle$, commonly referred to as pileup, as a function of the instantaneous luminosity, the number of circulating bunches n_b , their frequency f and the total cross section of inelastic scattering of

the protons σ_{inel} :

$$\langle \mu \rangle = \frac{\sigma_{\text{inel}} \mathcal{L}_{\text{inst}}}{n_b f}. \quad (2.8)$$

As described in Section 2.1.4, the amount of pileup at the LHC is significant and its effects need to be kept under control when performing physics analyses.

2.1.3 The purpose of the LHC

The construction of the Large Hadron Collider (LHC) at CERN was approved in December 1994 to replace the existing electron-positron accelerator, the LEP [41], after the completion of its physics programme. At the time, the largest machines in operation were the Tevatron [42], a proton-antiproton collider located at the Fermilab National Laboratory in the US, and the LEP itself, whose 27 km underground tunnel is now used for the LHC. The LEP experiments were designed to provide precise measurements of electroweak processes [43], thanks to the large number of Z and W bosons produced by the electron-positron collisions with low background rates. In parallel, the Tevatron was exploring the energy frontier, leading to the discovery of the top quark [44, 45] in proton-antiproton collisions at an energy of 1.8 TeV (subsequently increased to 1.96 TeV). Despite the reach of the Tevatron, however, the general consensus of the scientific community was that a more energetic machine would be needed to search for new physics up to the TeV scale [46], including the Standard Model Higgs boson. Indeed, the Higgs was eventually not observed neither at the LEP [47] nor at the Tevatron [48, 49], so its discovery became a primary goal of the LHC experiments.

In terms of operation, the new accelerator was expected to deliver collisions at an unprecedented centre of mass energy, larger by one order of magnitude with respect to the Tevatron and by two orders of magnitude with respect to the LEP. To achieve this goal, the only possible option was to build a hadron collider, because electron-photon machines are limited by the emission of synchrotron radiation (Equation 2.5). A relevant choice to make was whether to design a proton-antiproton collider, following the strategy of the Tevatron, or a proton-proton machine with two identical beams. The advantage of using antiproton beams is that in proton-antiproton collisions the cross sec-

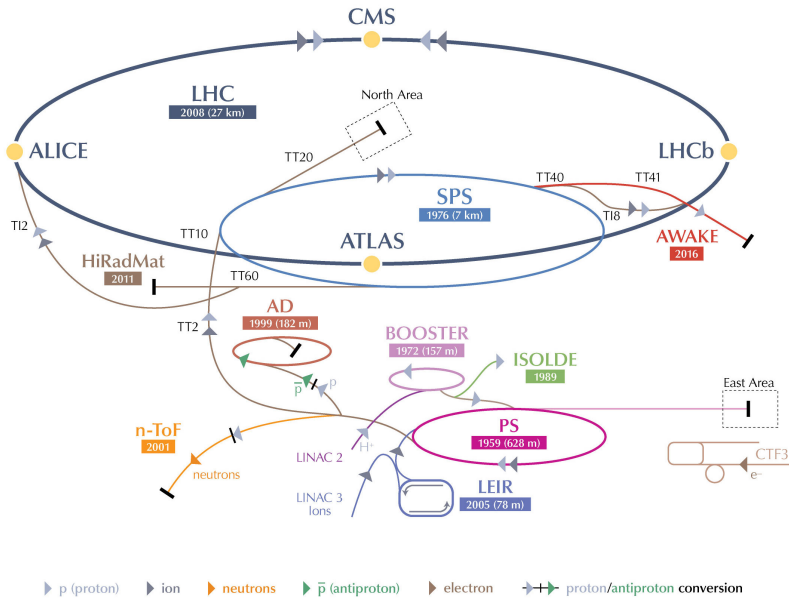


Figure 2.2: Scheme of the experimental facilities of CERN, showing the accelerator complex and the associated experiments.

tion of processes initiated by quark-antiquark annihilation increases, due to the higher antiquark content of antiprotons. However, at the characteristic centre of mass energy of the LHC the dominant production modes of the most relevant physics processes are initiated by gluons, which are equally present in protons and antiprotons. Since antiproton beams are difficult to produce at high intensities, it was chosen to run the LHC with two proton beams.

Finally, the LHC was also designed to deliver collisions of lead ions, with a dedicated physics programme aimed at studying the thermodynamical properties of QCD and the quark-gluon plasma. This programme is beyond the scope of this thesis, so the operation with lead ions is not further described.

2.1.4 The CERN accelerator complex and the LHC

Figure 2.2 shows the full infrastructure of the CERN laboratory that prepares the proton beams for the injection in the LHC at an energy of 450 GeV [50]. Protons are produced through the ionisation of a hydrogen source, then they are accelerated to 50 MeV by a

	Design	2015	2016
\sqrt{s} [TeV]	14	13	13
Maximum n_b	2808	2244	2220
Average $\langle \mu \rangle$	-	13.7	24.9
Maximum $\langle \mu \rangle$	19	28.1	52.2
Peak $\mathcal{L}_{\text{inst}}$ [$10^{33} \text{cm}^{-2}\text{s}^{-1}$]	10	5.0	13.8
\mathcal{L}_{tot} for physics [fb^{-1}]	-	3.2	32.8

Table 2.1: Performance parameters of the LHC during the 2015 and 2016 operation as measured by the ATLAS experiment [53], compared to the design values from Ref. [54].

linear accelerator called LINAC 2. They are then injected in the first circular machine, the Proton Synchrotron Booster (PSB), that increases their energy up to 1.4 GeV and prepares them for the following step, the Proton Synchrotron (PS). The PS is the oldest accelerator of CERN still in operation: it was built in 1959 and today it is used to accelerate the protons from 1.4 to 26 GeV. The next stage is the Super Proton Synchrotron (SPS), where the W bosons were discovered in 1983 by the UA1 and UA2 Collaborations [51, 52]. The SPS is now used to increase the energy of the protons up to 450 GeV, so that they can finally be injected in the LHC.

The LHC operation

The design report [54] published in 2004 describes the expected performance of the LHC before its construction, summarised in Table 2.1 in comparison with the 2015 and 2016 runs. The centre of mass energy is designed to be $\sqrt{s} = 14$ TeV with a maximum instantaneous luminosity of $\mathcal{L}_{\text{inst}} = 10^{34} \text{cm}^{-2}\text{s}^{-1}$, to be obtained with a beam split into 2808 bunches of $\sim 10^{11}$ protons each. During the first years of operation some of the performance parameters have been reached or even exceeded, while others are still below the targets, including the center of mass energy \sqrt{s} .

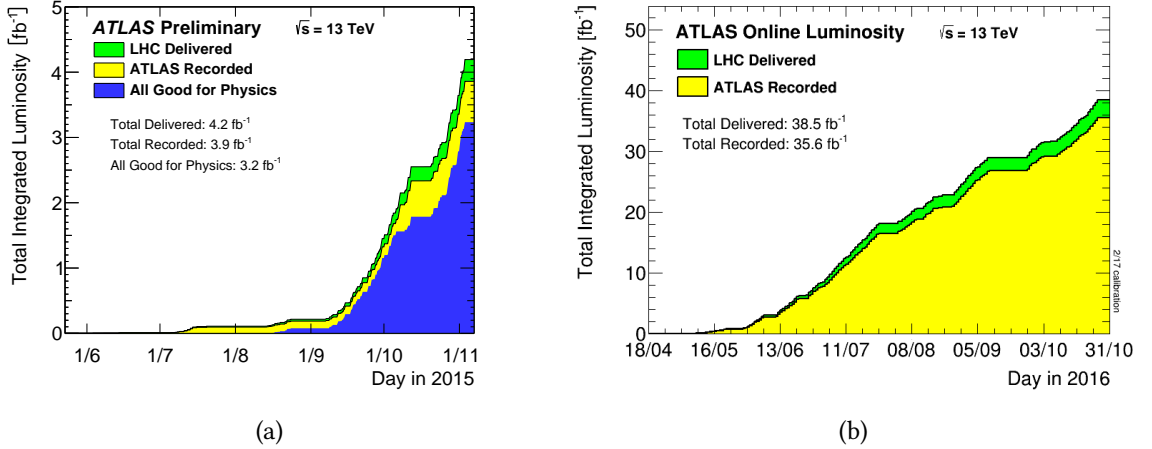


Figure 2.3: Total integrated luminosity delivered by the LHC and recorded by the ATLAS detector in 2015 (a) and 2016 (b). For 2015 the figure includes the histogram obtained after further quality criteria are applied to the data to make them available for physics analyses. The majority of the dataset analysed in this thesis are part of the 2016 dataset.

The first run of the LHC (Run 1) began when the first beams circulated in the machine on September 10th, 2008. After 9 days of operation a serious incident was caused by the excessive heating of a superconductive cable in the connection between two magnets, causing severe damage to a sector of the accelerator. After a necessary shutdown period of one year, the first proton collisions took place in fall 2009 at the minimum centre of mass energy $\sqrt{s} = 900 \text{ GeV}$. In 2010 and 2011 the LHC delivered two extended periods of data taking at $\sqrt{s} = 7 \text{ TeV}$ reaching $\mathcal{L}_{\text{inst}} = 2 \times 10^{32} \text{ cm}^{-2} \text{ s}^{-1}$ and $\mathcal{L}_{\text{inst}} = 3.65 \times 10^{33} \text{ cm}^{-2} \text{ s}^{-1}$ respectively. In 2012 the energy of the collisions was raised to $\sqrt{s} = 8 \text{ TeV}$, reaching a maximum $\mathcal{L}_{\text{inst}} = 8 \times 10^{33} \text{ cm}^{-2} \text{ s}^{-1}$ and accumulating a total integrated luminosity $\mathcal{L}_{\text{tot}} = 20 \text{ fb}^{-1}$. At the end of Run 1 the LHC had almost reached the design value of the instantaneous luminosity, while the centre of mass energy was still significantly below the target due to the limitations in the performance of the magnets that emerged after the incident of 2008.

After a long shutdown period of two years, the second run of the LHC (Run 2) began in

spring 2015 at $\sqrt{s} = 13$ TeV, close to the design value of the centre of mass energy. Table 2.1 shows how the machine performed during the first two years of Run 2, during which the data analysed in this thesis were collected. The cumulative integrated luminosity versus time recorded by the ATLAS experiment is presented in Figures 2.3a and 2.3b for 2015 and 2016 respectively. Figure 2.4a shows the distribution of the average number of interactions per bunch crossing $\langle \mu \rangle$ (see Equation 2.8) during the 2015 and 2016 runs: the increase in instantaneous luminosity in 2016 caused a larger amount of pileup in the experiments. Finally, in Figure 2.4b the peak luminosity is plotted for every fill of the 2016 run, during which the performance of the LHC has significantly exceeded the design targets.

At the time of writing Run 2 is still ongoing. In 2017 the LHC delivered an additional dataset comparable to the one of 2016, reaching new record values of instantaneous luminosity and $\langle \mu \rangle$ at $\sqrt{s} = 13$ TeV. Another year of data taking is scheduled for 2018, after which a second long shutdown will begin. Since the analyses presented in this thesis are only using the data from the 2015 and 2016 runs, the more recent datasets are not further discussed.

2.2 The LHC experiments

The LHC serves seven different experiments, all located along its ring. The main experiments, ATLAS [37], CMS [55], LHCb [56] and Alice [57], are built in correspondence with the four interaction points where the collisions take place, as indicated by the yellow circles in figure 2.2. In addition there are three smaller experiments, TOTEM [58], LHCf [59] and MoEDAL [60]. A short description of their main purpose is provided below:

ATLAS and CMS are the two largest detectors at the LHC. They are both general-purpose experiments, designed with different technologies to search for the Higgs boson and to explore the energy frontier at the TeV scale.

LHCb is a forward detector optimised to the study the decays of B and D mesons in

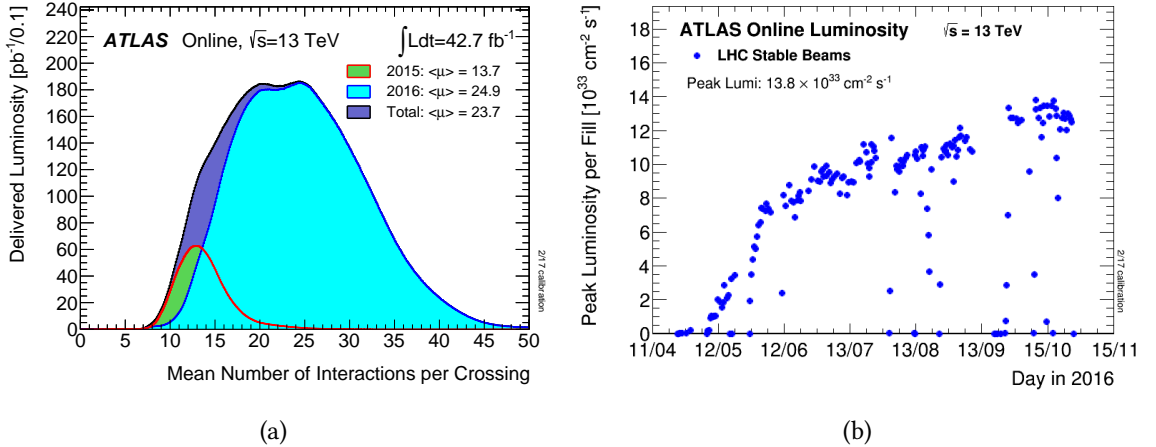


Figure 2.4: Distribution of the average number of interactions per bunch crossing $\langle \mu \rangle$ (see Equation 2.8) during the 2015 and 2016 runs (a) and maximum instantaneous luminosity for every fill in the 2016 run (b) as measured by the ATLAS detector.

proton-proton collisions, providing precision tests of the Standard Model parameters with special attention to CP violation.

ALICE is an asymmetric detector optimised for lead ion collisions. Its purpose is to study the properties of QCD phase transitions and quark gluon plasma.

TOTEM is a smaller experiment mounted next to the CMS detector along the LHC tunnel. It is used to monitor the LHC luminosity by providing measurements of the total, elastic and diffractive cross-section of proton-proton collisions in the forward region, at small angles with respect to the beam.

LHCf is a second forward detector located at both sides of the ATLAS cavern. Its purpose is to simulate cosmic ray shower processes by using particles scattered at small angles with respect to the beam axis.

MoEDAL is mounted next to the LHCb detector and is used to search for direct evidence of magnetic monopoles or highly ionising Stable Massive Particles (SMPs).

2.2.1 General-purpose experiments

The purpose of ATLAS and CMS detectors is to investigate the existence of new particles at heavy mass scales, with particular attention to the Higgs boson. Since the experimental signature of new physics beyond the Standard Model is unknown, both detectors are designed to identify as many different types of objects as possible, in order to maximise the chances of a discovery.

An essential feature of general-purpose detectors is hermeticity. Hermetic detectors are designed to observe all possible products of the collisions by covering the largest possible area around the interaction region. They are split in multiple sub-systems that provide the necessary information to identify and distinguish the different types of particles, with fine granularity in order to determine their position. If all particles with non-negligible interaction properties are measured with sufficient precision, hermetic detectors can reveal the presence of invisible objects such as neutrinos or dark matter by reconstructing the resulting momentum imbalance in the transverse plane, known as missing transverse momentum (E_T^{miss}).

ATLAS and CMS must also satisfy general requirements common to all experiments at the LHC. The accelerator provides a collision rate of about 40 MHz, setting the scale of the speed of response that the detector components must have to discriminate between subsequent events. A complex trigger and data acquisition system is needed to select the events where interesting physics objects are produced, saving the relevant information to permanent storage for offline analysis. Another important feature is resistance to radiation, especially for the detector components located at small distance from the interaction region.

ATLAS and CMS implement the above requirements using different technologies, in order to provide independent measurements of the same physics phenomena. Their overall performance is similar and the agreement between their results is a fundamental test of their reliability.

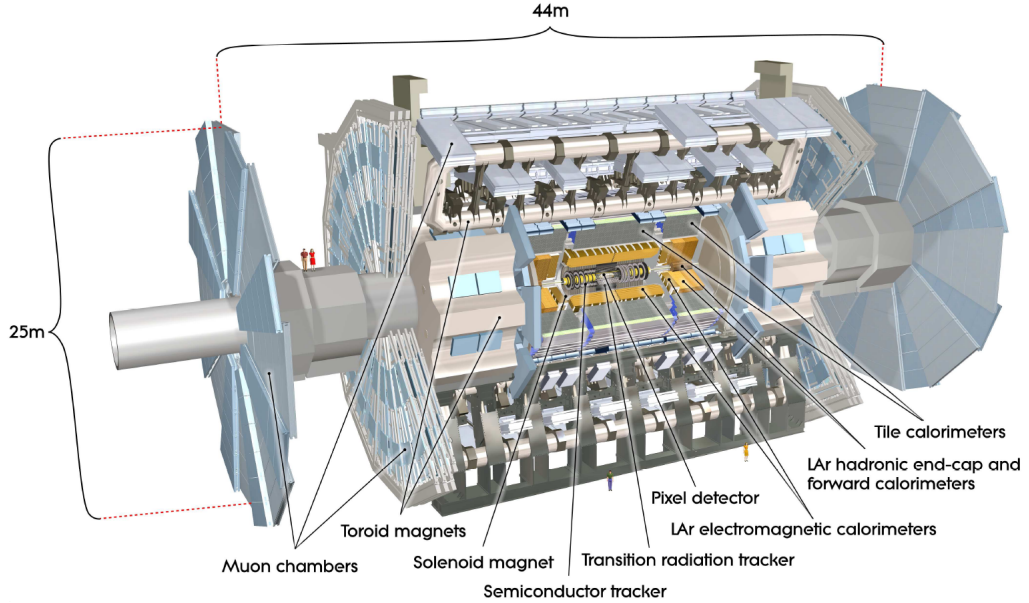


Figure 2.5: Overview of the ATLAS detector and its components.

2.3 The ATLAS detector

ATLAS (A Toroidal Lhc ApparatuS) is the largest detector at the LHC. The full system weights approximately 7 kTons and has a cylindrical symmetry around the beam axis, with a transverse diameter of 25 m and a longitudinal length of 44 m. The original design of the detector was proposed in 1994 [61], then its components were developed and assembled in parallel with the construction of the LHC accelerator.

A schematic representation of the detector is shown in Figure 2.5, including an overview of its main subsystems. The apparatus is designed to meet the requirements of a general-purpose experiment, with special attention to the products of hard scattering with large transverse momentum (p_T) with respect to the beam axis. The detector consists of a set of concentric layers surrounding the interaction region, and can be divided into four major components. The Inner Detector (see Section 2.3.3) reconstructs the ionisation tracks of charged particles and can be used to identify their production and decay vertices. Two calorimeters (Section 2.3.4) are then employed to measure the energy of electromagnetic and hadronic objects, while a Muon Spectrometer (Section 2.3.5) is placed in the outermost layer to identify muons that travel through the detector. A magnet system

(Section 2.3.2) made of two independent components is employed to bend the trajectories of charged particles in the Inner Detector and Muon Spectrometer, allowing the measurement of their momenta. In order to maximise the hermeticity of the detector, each sub-system is made of components that are parallel to the beam axis (barrels) and orthogonal to it (end-caps).

2.3.1 Coordinate system and event display

In ATLAS the direction of the beam defines the z axis of a right-handed cartesian reference frame, with origin located at the centre of the interaction region. The transverse section of the detector is mapped by the x and y coordinates, with the x axis pointing towards the centre of the LHC ring and the y axis pointing in upward direction. Due to the symmetry of the system, it is natural to introduce cylindrical coordinates replacing x and y with the polar angle θ and the azimuthal angle ϕ . For massive particles, the rapidity y can be introduced:

$$y = \frac{1}{2} \log \frac{E + p_z}{E - p_z} \quad (2.9)$$

where E is the energy and p_z is the longitudinal projection of the momentum of the particle. The above expression is additive under Lorentz boosts in the z direction, so any difference Δy is Lorentz invariant. This feature is particularly convenient at the LHC, where the particles are produced with an unknown longitudinal boost due to the variable fraction of momentum carried by the partons (see Section 2.1.2). An alternative quantity is the pseudorapidity η , which is equivalent to the rapidity in the limit of massless objects:

$$\eta = -\log \left[\tan \left(\frac{\theta}{2} \right) \right]. \quad (2.10)$$

Due to its simplicity, in ATLAS it is common to use η to indicate the polar angle, with $|\eta| = 0$ corresponding to the centre of the detector ($\theta = \pi/2$) and $|\eta| = \pm\infty$ in the forward regions ($\theta = 0, \pi$).

Figure 2.6 shows a scheme of the transverse section of the ATLAS detector, illustrating the characteristic signatures of the main types of particles:

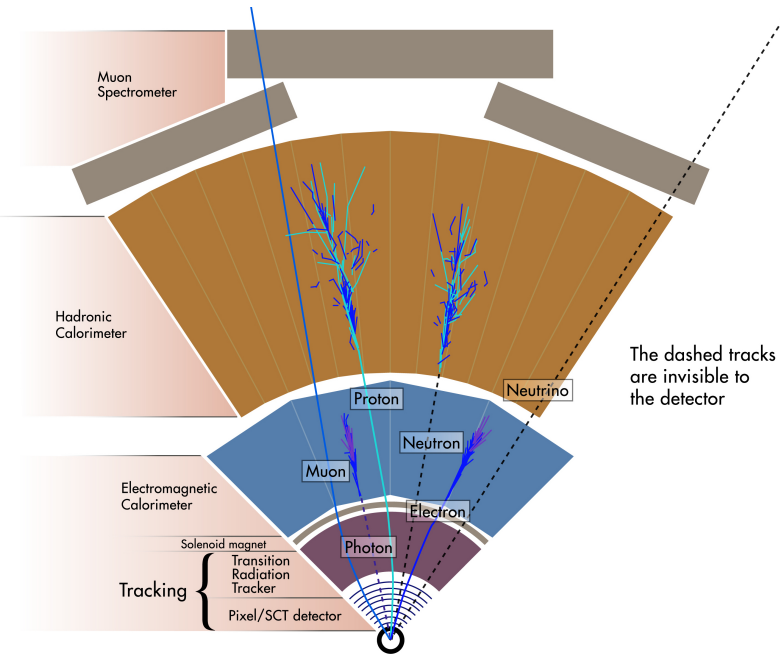


Figure 2.6: Simplified representation of the experimental signatures of the main types of particles in the ATLAS detector.

Photons are neutral objects, so they appear as showers in the electromagnetic calorimeter with no associated ionisation track in the Inner Detector.

Electrons are identical to photons in the calorimeter, but they also produce a track in the Inner Detector.

Neutrons leave no signature in the ID and generate hadronic showers that can start either in the hadronic calorimeter (as in Figure 2.6) or, with sizeable probability, also in the electromagnetic calorimeter (see Section 2.3.4).

Protons add an Inner Detector track to the characteristic signature of neutral hadrons.

Muons travel through each layer of the detector yielding ionisation tracks in the Inner Detector and in the Muon Spectrometer.

Neutrinos leave no signal in the detector, so their presence can only be inferred by reconstructing momentum imbalance in the transverse plane.

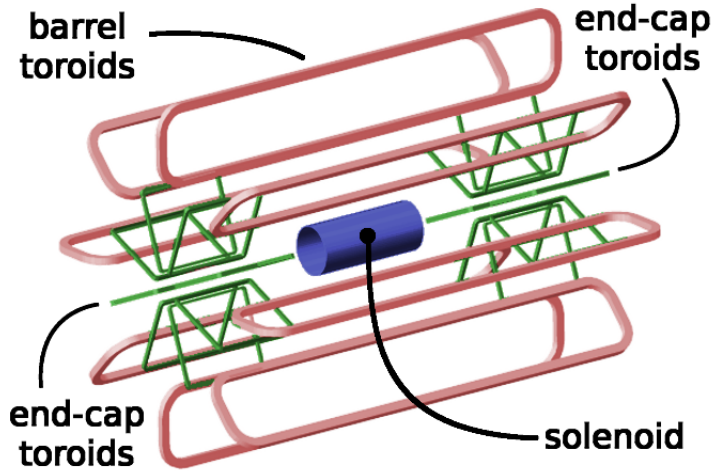


Figure 2.7: ATLAS magnet system.

2.3.2 Magnet system

The ATLAS magnet system [62], shown in Figure 2.7, provides the bending field that curves the trajectories of charged particles in the Inner Detector and in the Muon Spectrometer. It is composed of two independent components: a solenoid, located around the Inner Detector, and an outer system consisting in a set of barrel and end-cap toroids, that provide the magnetic field to the Muon Spectrometer. The layout of the magnet system distinguishes ATLAS from CMS, where a single solenoid magnet is employed [63], and has driven the design of the remaining parts of the detector.

Solenoid The solenoid magnet surrounds the Inner Detector described in Section 2.3.3, providing a magnetic field of 2 T using a nominal current of 7.73 kA that runs through 9 km of superconducting NbTi wires. The total length of the solenoid is 5.8 m, while the internal radius is 1.2 m and the thickness is only 4.5 cm, in order to minimise the amount of material placed in front of the calorimeters.

Toroids The barrel and end-cap toroids of ATLAS are both made of 8 identical magnets, that surround the calorimeter system with an azimuthal symmetry around the axis of the detector. The barrel system is 25.3 m long and has an outer diameter of 20.1 m, while the end-caps have a length of 5.3 m and 10.7 m of diameter. The peak

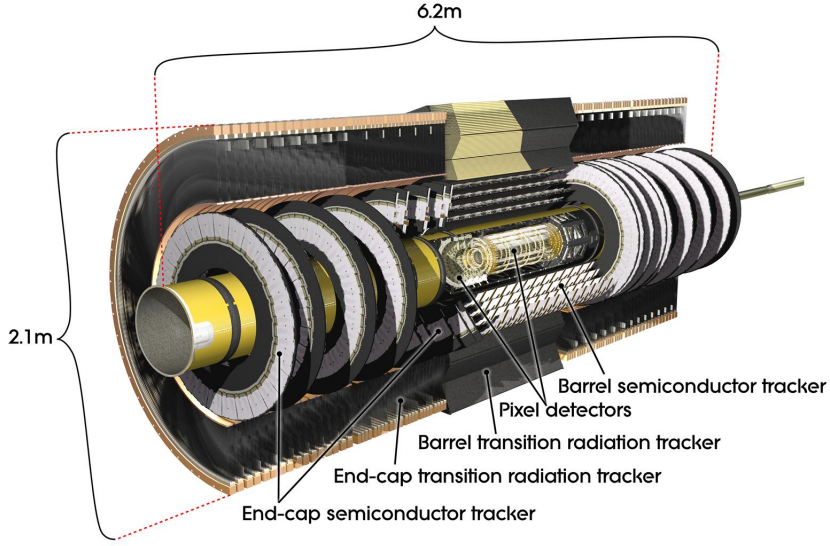


Figure 2.8: Transverse view of the barrel components of the ATLAS Inner Detector.

field produced by both barrel and end-cap toroids is 4 T, obtained with a nominal current of 20.5 kA.

2.3.3 Inner Detector

The Inner Detector (ID) [64] is located at the core of the ATLAS experiment, immediately around the interaction region where the collisions take place. Its purpose is to reconstruct the tracks of charged particles in the events, with a pseudorapidity coverage $|\eta| < 2.5$. As shown in Figure 2.8, the system is organised in cylindrical layers where the particles interact and release a localised signal. Due to the large multiplicity of particles produced by proton collisions, each layer needs to be finely segmented in order to provide an accurate measurements of the position of the hits, with enough precision to distinguish the individual tracks. Since the system is placed in proximity of the beam, it is also important to ensure that the hardware components are able to resist the high dose of radiation that they receive during the operation. Finally, the amount of material in the ID needs to be small in order to minimise the particle interactions before the calorimeter, that degrade the quality of the energy measurement.

The ID is split in three different subdetectors: a silicon Pixel detector, that includes an Insertable B-Layer (IBL) installed before the beginning of Run 2 in 2015, a Semi-Conductor Tracker (SCT) and a Transition Radiation Tracker (TRT). Each of them has a cylindrical symmetry, with the usual barrel and end-cap structure. Overall, the Inner Detector measures 6.2 m in length and 2.1 m in diameter.

Pixel detector

The Pixel detector [65] is the innermost part of the ID, designed to provide tracking information with the finest level of granularity. As shown in Figure 2.9, the barrel part is made of four cylindrical layers of modules: the IBL [66, 67] (at 33.25 mm of distance from the beam axis), the b-layer or L0 (50.5 mm), the L1 (88.5 mm) and the L2 (122.5 mm). The end-caps consist of three circular disks, that contribute to achieve the desired longitudinal acceptance $|\eta| < 2.5$. The silicon pixels have a different segmentation in the $R\text{-}\phi$ and z directions: the smallest size in the $R\text{-}\phi$ plane is 50 μm , while the minimum longitudinal size is 250 μm in the IBL and 400 μm in the other layers. Due to the cost of the technology, it was chosen to use the Pixels only in the innermost layers of the ID, where it is essential to maximise the spacial resolution.

Semi-Conductor Tracker

The SCT [68, 69] is the intermediate part of the ID, consisting of four barrel layers and two end-caps with nine disks each. The components of the SCT are made of silicon, but the pixels are replaced by strips of 80 $\mu\text{m} \times 12\text{ cm}$ to cover a larger area of space compared to the innermost layers. The strips are parallel to the direction of the beam in the barrels, while they are disposed radially in the end-caps. The individual layers are made of a pair of strip sensors, arranged at a relative angle of 40 mrad. This geometrical solution allows to obtain a good measurement of the position of the hits in the longitudinal direction, despite the significant length of the strips. The SCT is able to provide a spacial resolution of 16 μm in the $R\text{-}\phi$ plane and of 580 μm in the z direction.

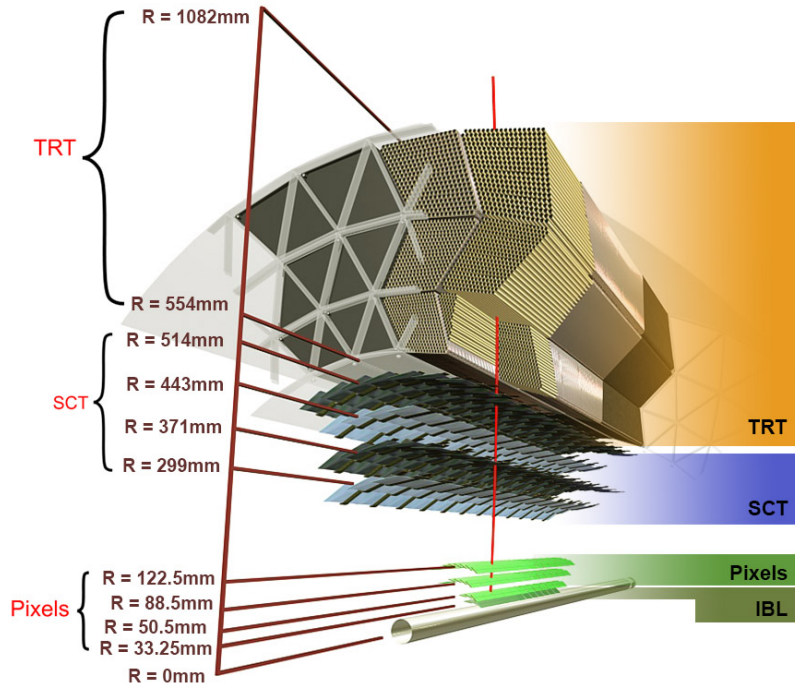


Figure 2.9: Transverse view of the ATLAS Inner Detector, showing the different layers.

Transition Radiation Tracker

The TRT [70, 71] occupies the external layer of the ID, with radius between 55.4 cm and 108.2 cm. Unlike the inner layers, this system is based on the use of straw detectors with 4 mm of diameter and maximum length of 144 cm, filled with a mixture of Xenon (70%), CO₂ (27%) and Oxygen (3%). Similarly to the SCT strips, the straw tubes are located in a barrel, where they are parallel to the beam direction, and in two end-caps, where they are arranged radially. Each straw is crossed by a thin tungsten wire that serves as anode, so the device operates as a small drift chamber that measures the ionisation produced by the charge particles that cross it. A crucial feature of the TRT is that the region between the tubes is occupied by radiating material, where the particles emit x-rays proportionally to their relativistic γ factor. These photons are known as transition radiation, because they are generated when the particles cross the boundary between two media with different dielectric constants. The transition radiation is absorbed by the Xenon atoms in the tubes, and it is significantly larger for electrons than for heavier

objects, because their average γ factor is greater. As a result, the TRT is able to provide a useful measurement to discriminate between electrons and other types of particles. Thanks to its geometry, the TRT yields a large number of hits (~ 30) for each track in the $R\text{-}\phi$ direction, with a longitudinal acceptance $|\eta| < 2$ and a spacial resolution of about $130 \mu\text{m}$.

2.3.4 Calorimeter system

The calorimeter system of ATLAS surrounds the the Inner Detector and the solenoid magnet and provides a measurement of the energy of electrons, photons and hadrons, that generate showers of particles as a result of their interaction with the materials. The characteristic parameters describing the depth of electromagnetic and hadronic showers are the radiation length X_0 and the interaction length λ_I with $\lambda_I \gg X_0$ for all common materials². The detectors are designed to provide a full containment of the showers, and they are segmented in cells in order to obtain localised measurements of the energy deposits.

As shown in Figure 2.6, ATLAS employs two different types of calorimeters: the inner component is the Electromagnetic Calorimeter (ECAL) dedicated to electrons and photons, while the outer part is the Hadronic Calorimeter (HCAL) optimised for strongly interacting particles. The ECAL and HCAL are based on a sampling technology, in which the material that absorbs the incoming particles is distinct from the one that measures their energy. In addition, both calorimeters are non-compensating, which means that they have a different signal response to electrons and hadrons, so a dedicated scale factor must be applied to calibrate the two components of the showers at the same energy scale. In order to increase the longitudinal acceptance of the detector, two Forward Calorimeters (FCAL) are mounted on the opposite end-caps close to the beam pipe.

²The radiation length X_0 is defined as the mean distance over which an electron reduces its energy by a factor $1/e$, while the interaction length λ_I is the mean distance travelled by a hadron before being subjected to an inelastic nuclear interaction.

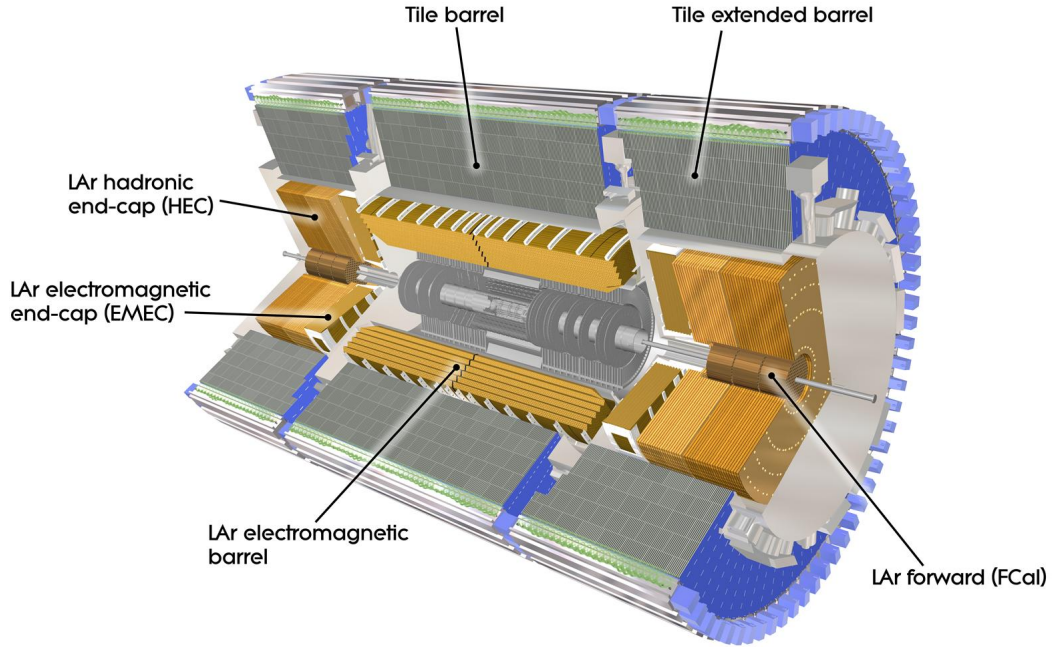


Figure 2.10: Section of the calorimeter system of the ATLAS, highlighting the different components of the ECAL and the HCAL.

Electromagnetic calorimeter

The ECAL [72] is a sampling calorimeter that employs lead (Pb) plates as absorbers and liquid argon (LAr) ionisation chambers with copper electrodes as active components. The system is divided into a central barrel, with an acceptance $|\eta| < 1.475$, and two end-caps with range $1.375 < |\eta| < 3.2$. The lead plates are arranged radially with a characteristic accordion geometry, that provides a full azimuthal coverage and avoids the presence of cracks in the ϕ direction. The choice of LAr is motivated by its linear response combined with large signal yields and good resistance to radiation damage, while a limiting factor comes from its poor time resolution (400 ns), longer than the distance between two subsequent events.

The ECAL is finely segmented in cells in the $\eta\text{-}\phi$ direction and it is composed of three layers, each with specific properties and purposes. The first layer has a thickness of $4.3 X_0$ and a fine granularity in the $\eta\text{-}\phi$ plane, which is needed to obtain a precise measure-

ment of the initial development of the showers. Thanks to its segmentation, this layer plays a key role in the discrimination between showers produced by single photons and showers that originate from the decay of neutral pions (π_0) into two photons. The second layer measures $16 X_0$ in thickness, and provides additional information which is used to determine the position and direction of the showers. The third layer has a depth of $2 X_0$ and is used to measure the leakage of electromagnetic showers beyond the ECAL, contributing to the discrimination between electromagnetic and hadronic showers. The ECAL is completed by a presampler layer of LAr with no passive material, which is placed in the solenoid magnet in order to measure the particle interactions in the inner parts of the detector.

In total, the ECAL has a thickness of $22 X_0$ in the barrel for particles with $\eta = 0$, which grows as a function of pseudorapidity reaching $33 X_0$ in the barrel and up to $38 X_0$ in the end-caps. The longitudinal segmentation of the components of the ECAL produces a few crack regions where the nominal performance is deteriorated. This happens at $\eta = 0$ due to a 4 mm gap in the central barrel, at $1.37 < |\eta| < 1.52$ due to the transition between barrel and end-caps, and at $|\eta| = 2.5$ where there is a small gap between two end-cap crowns.

Hadronic calorimeter

The HCAL is dedicated to the measurement of the hadronic showers, that are only partially contained by the ECAL. As shown in Figure 2.10, the full system consists of a barrel, two extended barrels and two Hadronic End-Caps (HEC).

The barrel and extended barrels form the Tile Calorimeter (TileCal) [73], which uses steel tiles as absorbers and plastic scintillators as active material. The barrel covers the central pseudorapidity region $|\eta| < 1.0$, while the extended barrels have a range $0.8 < |\eta| < 1.7$, with a partial overlap aimed at reducing the impact of the cracks. Similarly to the ECAL barrels, both central and extended barrels of TileCal are divided into three layers, with an approximate thickness of 1.5, 4.1 and 1.8 interaction lengths in the central component and of 1.5, 2.6 and 3.3 interaction lengths in the extended ones. Finally, the HEC is

composed of two independent end-caps made of LAr and copper (Cu), that increase the pseudorapidity coverage of the detector to $1.5 < |\eta| < 3.2$.

Figure 2.11 from Ref. [37] shows the cumulative amount of material, in units of interaction length λ_I , as a function of the pseudorapidity η in the various layers of the detector. The total thickness is at least $10 \lambda_I$ in all pseudorapidity regions, with peaks and dips caused by the transition between different components.

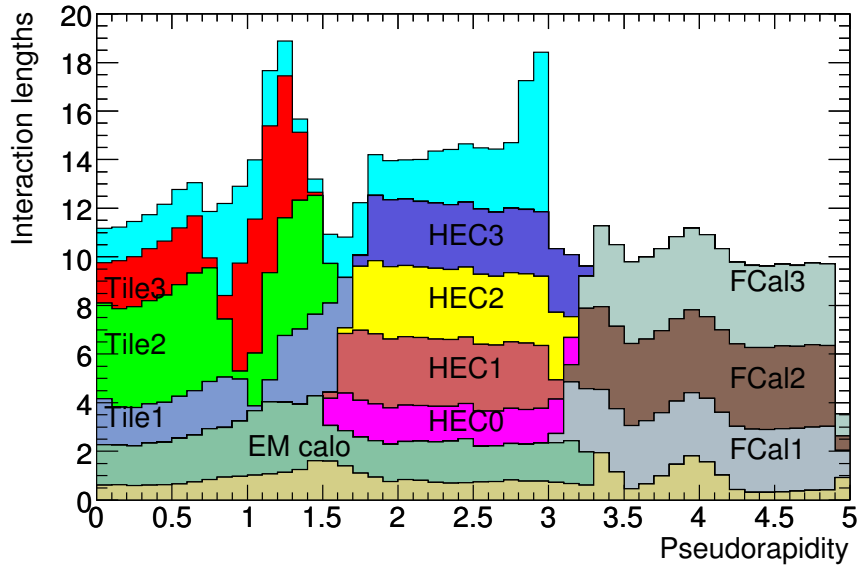


Figure 2.11: Total occupancy of the major components of the detector in units of interaction length, as a function of the pseudorapidity $|\eta|$. The graph shows the material in front of the ECAL, the different layers of ECAL and HCAL including the forward components, and also the total amount of material in front of the first active layer of the muon spectrometer up to $|\eta| < 3.0$.

Forward calorimeters

The calorimeter system is completed by two forward detectors (FCal) that provide electromagnetic and hadronic energy measurements in the pseudorapidity range $3.1 < |\eta| < 4.9$. The FCal uses LAr as active material and is divided in three layers of 45 cm each. The inner layer uses copper as absorber and is dedicated to electromagnetic showers, while

the remaining two are made of tungsten and are optimised to measure the hadronic ones. The measurements performed by the FCal are not as accurate as those from the other subdetectors, due to a coarser segmentation and to the large amount of background from underlying hadronic activity in the forward region. Nevertheless, they give an crucial contribution to the hermeticity of ATLAS, which is important for the measurement of the missing transverse momentum (E_T^{miss}).

2.3.5 Muon Spectrometer

The outermost component of ATLAS is the Muon Spectrometer (MS) [74] dedicated to the detection of muons, that travel through the inner layers of the detector as minimum ionising particles. The muon trajectory in the MS is curved in the R - z plane by the bending field of the toroid magnets, so the reconstruction of the tracks can be used for the measurement the momentum, similarly to what happens in the Inner Detector. The larger size of the MS allows to provide accurate measurements of muons up to the TeV scale, which is essential for the physics program of ATLAS.

The MS consists a central barrel with three cylindrical layers with a radius of 5, 7.5 and 10 m, and four end-cap wheels at a longitudinal distance of 7.4, 10.8, 14 and 21.5 m from the centre of the detector. This structure hosts four different subsystems shown in Figure 2.12, each contributing to specific needs of the detector. Monitored Drift Tube (MDT) chambers and Cathode Strip Chambers (CSC) are dedicated to high-resolution measurements of the tracks in the pseudorapidity range $|\eta| < 2.7$, while Resistive Plate Chambers (RPC) and Thin Gap Chambers (TGC) are designed to provide trigger information with faster speed of response. A brief description of the four components of the MS is given below.

Monitored Drift Tubes The MDTs are chambers composed of drift tubes with 30 mm of diameter, filled with a mixture of Argon and CO₂. They cover the pseudorapidity range $|\eta| < 2.7$, except in the innermost end-cap layer where they only reach $|\eta| < 2.0$, providing a spatial resolution of approximately 80 μm per tube and 35 μm per chamber. They are disposed orthogonally with respect to the beam axis,

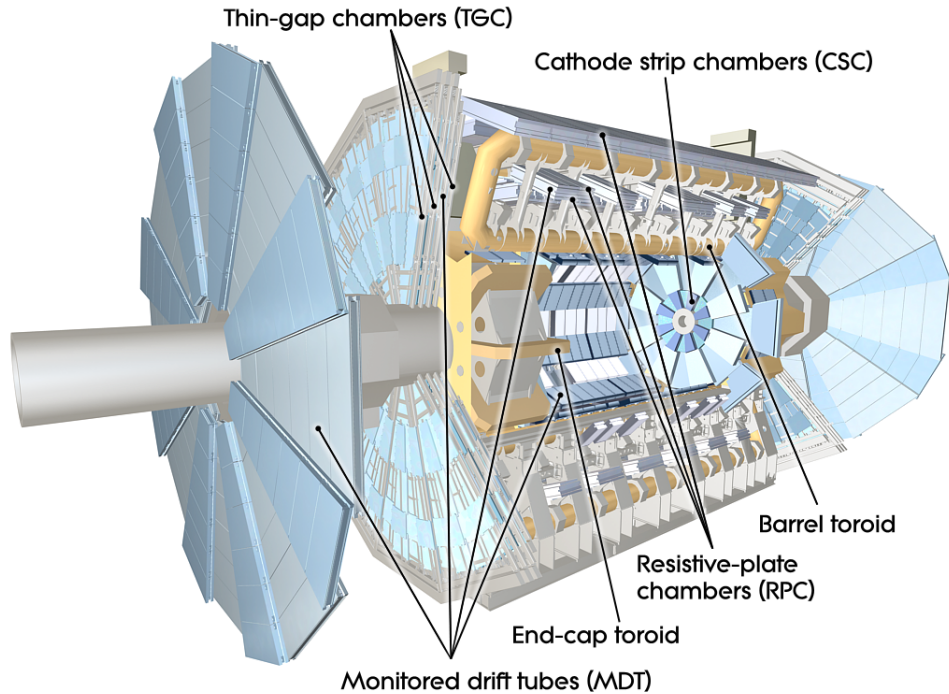


Figure 2.12: Scheme of the ATLAS outer layer showing the Muon Spectrometer.

so they only provide a measurement of the η coordinate of the hits. The major limitation of the MDTs is that their drift time can reach up to 700 ns, limiting the maximum rate of operation of the system.

Cathode Strip Chambers The CSCs are multi-wire proportional chambers with a finer spatial resolution with respect to the MDTs. They are used in the first layer of the end-caps corresponding to $2.0 < |\eta| < 2.7$, where a higher rate of signal is expected due to the abundance of particles in the forward region.

Resistive Plate Chambers The RPCs are gas chambers mounted in the barrel system of the MS, in the pseudorapidity range $|\eta| < 1.05$. They are formed by two parallel plates, a positively-charged anode and a negatively-charged cathode, both made of a plastic material with high resistivity (Bakelite). The signal from ionising particles is collected by external metallic strips with a time resolution of the order of 1 ns, significantly shorter than the separation between two bunch crossings at the LHC (25 ns). They are used as inputs for the muon triggers, thanks to the fast speed of

response, and they also measure the ϕ coordinate of the muon hits, which is not provided by the MDTs.

Thin Gap Chambers The TGCs are multi-wire proportional chambers optimised to achieve a fast signal collection. They are mounted in the end-cap muon spectrometers to improve the muon trigger capability in the $1.05 < |\eta| < 2.4$ region and to determine the ϕ coordinate in the forward direction up to $|\eta| = 2.7$.

2.3.6 Trigger and Data Acquisition

As discussed in Section 2.1, the LHC is able to deliver collisions between proton bunches at a rate of 40 MHz, significantly higher than the readout capabilities of ATLAS. The physics processes of interest, however, are produced in a minor fraction of these events, while most bunch crossings yield only soft hadronic collisions that are not interesting for physics analyses. The Trigger system of ATLAS [75] is designed to perform an online selection of events where interesting physics objects are produced, making a fast real-time decision based on the signal in the sub-detectors. The accepted events are recorded by a Data Acquisition system, that channels the data from the sub-detectors to the permanent storage.

A scheme of the Trigger and Data Acquisition system (TDAQ) is shown in Figure 2.13 where the interplay between the different sub-components is highlighted. A full trigger selection involves a chain of decisions taken first by a hardware-based Level-1 trigger (L1) and subsequently by a software-based High Level Trigger (HLT). If their output rate is too high, the trigger chains can be pre-scaled by a factor P , which means that only a fraction $1/P$ of the events that meet the selection criteria is accepted. Since this procedure causes a loss of interesting events, pre-scaled trigger chains are generally not used in physics analyses.

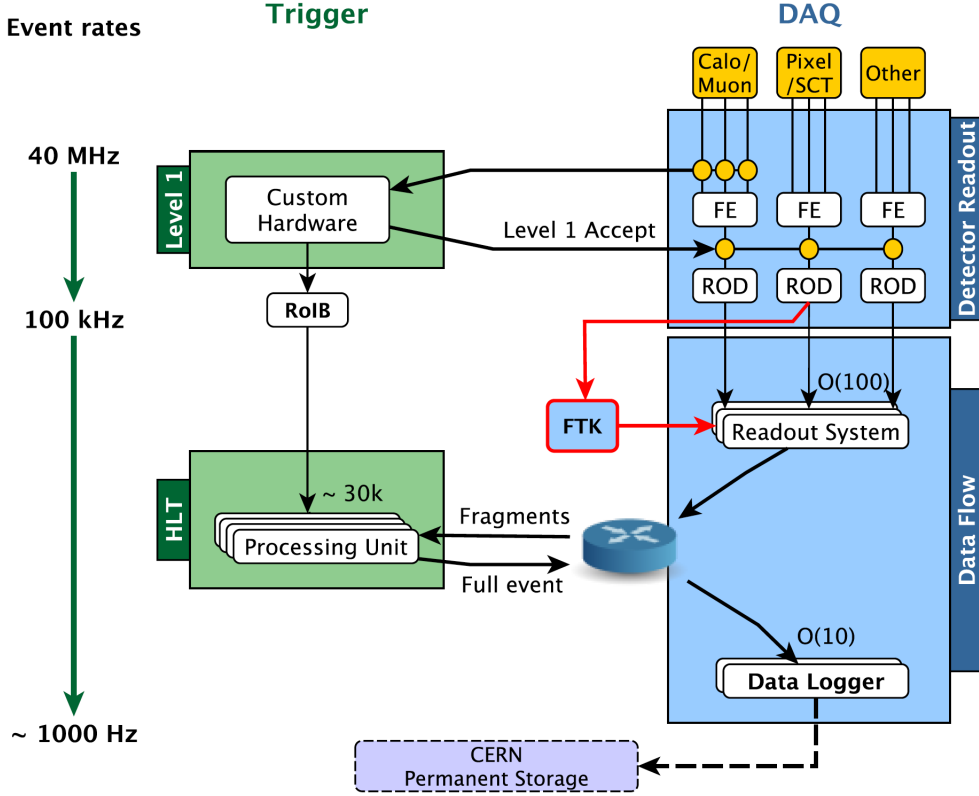


Figure 2.13: Scheme of the TDAQ system of the ATLAS detector [76].

Level-1 Trigger

The L1 trigger [77] performs a first selection of events that reduces the rate from the bunch crossing frequency (40 MHz) to a maximum output of 100 kHz, using low granularity information from the calorimeters (L1-Calorimeter) and the dedicated sub-systems in the Muon Spectrometer (L1-Muon). The selections on the signals from the sub-detectors are optimised to identify events where interesting physics objects are produced, such as electrons, muons, τ leptons, jets or missing transverse momentum (E_T^{miss}). During Run 2, the system has been upgraded by adding a topological trigger processor (L1-Topo) [78] that combines kinematic information from different calorimeter and muon trigger objects, allowing to define more complex selections based on the geometry of the event. The data from the above sub-systems is kept in memory buffers for a latency period of 2.5 μs , during which the Central Trigger Processor (CTP) decides whether the events meets

the selection criteria. If it is accepted, the corresponding data is sent to detector-specific Readout Drivers (RODs) and subsequently transferred to the Readout System (ROS). In addition, the Regions of Interest (RoIs) with the η and ϕ coordinates of the interesting objects in the event are determined by an ROI Builder (RoIB) and transferred to the HLT to act as seeds for further selections.

High Level Trigger

The HLT [79] performs additional selections that reduce the event rate from the output of L1 (100 kHz) to values of the order of 1 kHz. The system exploits software algorithms that use the full detector information, typically restricted to the RoIs defined by the L1 trigger in order to reduce the computational time. In Run 1 the HLT consisted of two separate levels of decisions, Level-2 (L2) and Event Filter (EF), running in separate server farms. Before the beginning of Run 2 the two levels were merged [80] into a single homogeneous farm, removing redundancies between them and simplifying the hardware and software structure. In addition, a new hardware-based Fast Tracker (FTK) [81] is being incorporated, in order to provide tracking information with full detector coverage to the HLT. The events selected by the HLT algorithms are sent to mass storage by Sub-Farm Output (SFO) nodes.

Data Quality

The data collected by the ATLAS detector must satisfy standard quality criteria in order to be used for offline analysis. To provide an effective monitoring of the performance of the detector during the runs, the ATLAS data are recorded in luminosity blocks, short periods of time (with typical length around one minute) during which the configuration of each sub-system is kept constant. A set of quality parameters can be monitored during the operation for each sub-detector, and a record of the performance is kept in order to compile a Good Run List (GRL) for each period of data taking. The GRL contains the list of luminosity blocks in each run where the detector has performed in line with the quality requirements.

Chapter 3

Event simulation and reconstruction

This chapter presents a comprehensive discussion of the experimental signature of the major physics processes in the ATLAS experiment. Section 3.1 is dedicated to a discussion of the event simulation techniques, from the proton-proton collisions to the interaction of the particles with the detector. The remaining part of the chapter (Section 3.2) describes the standard procedures for the reconstruction of different types of physics objects in ATLAS, based on the signal that they release in each detector sub-system.

3.1 Monte Carlo simulation of ATLAS events

A crucial tool for the analysis of the ATLAS data is the simulation of physics processes, heavily used to predict their kinematic properties and their experimental signature in the detector. The standard approach is to employ Monte Carlo (MC) generators, where the events are simulated stochastically following probability distributions determined by the theory. Once the basic physics events are generated, the following step is to simulate the response of the detector to the particles in the final state, in order to obtain samples that can be directly compared to the ATLAS data.

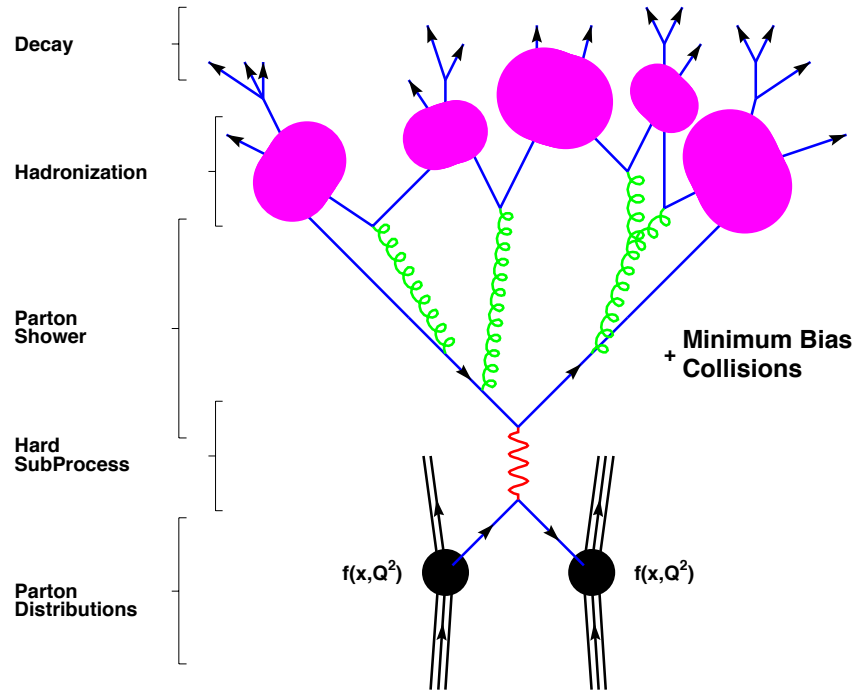


Figure 3.1: Scheme of a physics process at the LHC, showing the various stages from the two protons in the initial state to the decays of the produced particles [82].

3.1.1 Simulation of physics processes

The production of physics objects in proton-proton collisions can be viewed as a multi-stage process, as shown in Figure 3.1. The first step is the hard scattering of individual partons from the protons, already discussed in Section 2.1.2, where the Parton Distribution Functions (PDFs) play a key role. The hard scattering can be further split into a Matrix Element computation, which typically uses perturbative calculation truncated at a fixed order, and a Parton Showering stage which simulates the emission of extra soft objects in the event. Due to the confinement properties of QCD, any quarks or gluons produced by the hard scattering are eventually converted into hadrons through a hadronisation process (see Section 1.1.2). If the particles are unstable, their decay can be simulated in different stages of the chain. A description of the individual steps of the Monte Carlo simulation procedure is provided below:

Factorisation and PDFs As discussed in Section 2.1.2 the hard scattering in proton-

proton collisions involves two partons (quarks or gluons) that carry an unknown fraction x_1 and x_2 of the the momentum of the protons. The cross section σ of the full physics process is given by Equation 2.7, where the probability of finding a parton with momentum fraction x is factorised with respect to the partonic cross section $\hat{\sigma}$. To take into account the effects of higher order corrections, it is necessary to introduce a factorisation scale μ_F and a renormalisation scale μ_R (see Ref. [38] for a full discussion) and Equation 2.7 becomes:

$$\sigma_{ij} = \int dx_1 dx_2 f_i(x_1, \mu_F^2) f_j(x_2, \mu_F^2) [\hat{\sigma}_0 + \alpha_S(\mu_R^2) \hat{\sigma}_1 + \dots]_{ij \rightarrow X}, \quad (3.1)$$

where the perturbative corrections $\hat{\sigma}_n$ of order α_S^n are introduced. Formally the total cross section is independent of μ_F and μ_R , because the scale dependance at infinite order is exactly compensated by the coefficients $\hat{\sigma}_n$. At fixed order, however, the numerical results are affected by the choice of the two scales, which is a source of theoretical uncertainty. The Parton Distribution Functions (PDFs) are determined by experimental measurements at fixed energy scales, and their evolution to different scales is determined through the DGLAP equations [83–85]. For the analyses discussed in this thesis, PDFs derived by the CTEQ [86, 87], NNPDF [88, 89] and MSTW [90] groups were used.

Matrix element An essential step of the MC simulation is the computation of the partonic cross section $\hat{\sigma}_n$. The process of interest can be schematically represented as

$$ij \rightarrow X + \sum_i x_i$$

with an initial state ij and a final state that includes a main product X and a variable number of extra objects x_i . The associated scattering matrix, or S-matrix, can be computed at different orders in perturbation theory.

Figure 3.2 shows three Feynman diagrams for the case of top pair production initiated by two quarks: the first (Figure 3.2a) is a Leading Order (LO) diagram, while the others (Figures 3.2b and 3.2c) are Next to Leading Order (NLO) diagrams that include a gluon emission and a loop correction respectively. While the diagrams

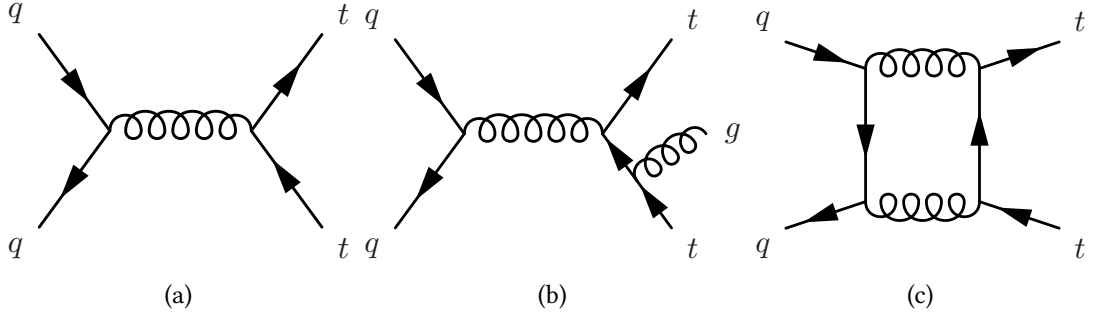


Figure 3.2: Feynman diagrams for top pair-production initiated by two quarks, where (a) is a LO diagram, (b) is a NLO diagram with a gluon emission and (c) is a NLO diagram with a loop correction [93].

in Figures 3.2b and 3.2c are both divergent, an important theorem by Kinoshita-Lee-Nauenberg [91, 92] states that at fixed orders in perturbation theory the infinities are exactly cancelled, yielding a finite result for the cross section. If a larger multiplicity of objects in the final state is included, however, the cancellations are spoiled and divergent contributions from soft collinear emissions can appear. The standard strategy to remove the divergencies is to introduce a cutoff in the computation of the matrix element, such that extra soft objects are excluded and a finite result can be obtained. These missing objects are subsequently added by dedicated Parton Shower (PS) generators.

Parton Shower Once the computation of the matrix element is completed, a PS generator is used to include the emission of extra soft objects. In QCD, the possible processes are the emission of a gluon by a quark ($q \rightarrow qg$) and the emission of a quark pair or a gluon pair by a gluon ($g \rightarrow qq$ and $g \rightarrow gg$). The MC generators make use of Sudakov form factors [94], that describe the probability for a gluon with a virtuality level Q_a^2 to evolve to a virtuality Q_b^2 without radiating. The PS objects can appear as parts of the Final State Radiation (FSR, as in Figure 3.2b) or the Initial State Radiation (ISR). The latter case is implemented in the MC using a backward evolution technique, where the matrix element is computed us-

ing partons with fixed momentum and the initial state is determined by evolving them in reversed time order.

ME-PS matching In order to combine the matrix element and PS generators, it is necessary to define a procedure that determines the respective domains. This is done by dedicated matching algorithms that identify two orthogonal regions of phase space, one containing the products of the hard scattering and one with the additional soft objects in the event. The goal of the matching is to remove any potential overlap between the physics objects generated by the matrix element and by the PS, without causing significant discontinuities in observable spectra. The most common implementations are the Catani-Krauss-Kuhn-Webber (CKKW) [95] and the Michelangelo L. Mangano (MLM) [96] schemes, both widely used by the ATLAS Collaboration.

Hadronisation Quarks or gluons in the final state evolve until they reach a Q^2 value of the order of $\Lambda_{\text{QCD}} \sim 200$ MeV, at which the confinement properties of QCD become relevant. As explained in Section 1.1.2, at this stage all the elementary hadrons in the event must recombine into colourless objects, mesons or baryons. The hadronisation process is regulated by non-perturbative QCD, so its simulation needs to rely on phenomenological models: the most common ones are the cluster model [97, 98] and the Lund string model [99, 100].

Underlying event and pileup While the hard scattering processes at the LHC involve only two quarks or gluons, the remaining partons from the initial state protons can yield an extra number of soft interactions at lower energy scale. As a result, the LHC processes can generally be regarded as Multiple Parton Interactions (MPIs) that produce a significant amount of underlying hadronic activity in the events (see Section 2.1.2). The underlying event is simulated using phenomenological models (tunes) extracted from experimental data [101, 102], which include a description of the colour flow.

Additional hadronic activity can originate from interactions between different pro-

ton pairs in the same bunch crossing (in-time pileup) or by remnants of collisions in different bunch crossings (out-of-time pileup). Both processes are simulated similarly to the underlying event, and are included in the MC samples used by the ATLAS Collaboration.

3.1.2 Monte Carlo generators

The scientific community has developed a variety of MC generators to implement the various steps of the simulation of physics processes at the LHC. A brief description of those that are used in this thesis is given below:

Pythia is a multi-purpose LO generator that can handle the full reaction chain for $2 \rightarrow n$ ($n \leq 3$) processes [103, 104], including hadronisation (with string model) and underlying event.

Herwig is a similar multi-purpose LO generator that simulates $2 \rightarrow 2$ processes [105] using the cluster model for hadronisation and underlying event.

MadGraph is a MC generator that handles the matrix element part of the simulation chain [106]. It can be used at LO or in its NLO version aMC@NLO, and it must be interfaced with another generator (typically Pythia or Herwig) for PS, hadronisation and underlying event.

Powheg is a NLO matrix element generator [107] that can be interfaced with Pythia or Herwig for PS, hadronisation and underlying event.

Sherpa is a multi-purpose generator that performs LO or NLO calculations for $2 \rightarrow n$ processes [108]. It includes matrix element, PS [109] and underlying event generator and it uses the CKKW method for the ME-PS matching.

EvtGen is a MC software that runs after Pythia or Herwig and provides an accurate description of the decay of b -hadrons in the final states of physics processes [110].

3.1.3 Detector simulation

The output of the Monte Carlo generators is a list of four-vectors of particles in the final state, which can be used to examine the kinematic features of the physics processes. In order to compare the MC samples with the ATLAS data, however, it is also necessary to simulate the interaction of the particles with the detector and the resulting signals from the sub-systems [111].

The detector simulation is implemented by the Geant 4 package [112], which is integrated in the ATLAS offline software. The full reconstruction chain includes a first stage dedicated to the interaction of the particles with the detector, and a second (digitisation) stage where the energy deposits are converted into voltages and currents in the sub-systems. The output of the simulation can be presented in a format identical to the output of the ATLAS TDAQ system, so the MC samples and the real ATLAS data can be processed by the same trigger and event reconstruction softwares.

Finally, it is important to mention that the ATLAS Collaboration makes wide use of faster simulations such as ATLFAST-II (or AF2) [113], where a parametrised description of the showers in the calorimeters is implemented in order to reduce the CPU processing time.

3.2 Object reconstruction

An essential step of the analysis of ATLAS data is the reconstruction of physics objects in the events, based on their experimental signature in the detector. As discussed in Section 2.3.6, a first selection of events is performed online by the TDAQ system, where the relevant features are identified by fast online algorithms. Once the events are recorded, the final objects to be used for the analyses are defined by more refined reconstruction algorithms, less affected by timing limitations.

The searches presented in this thesis employ different types of trigger selections, requiring the presence of missing transverse momentum (E_T^{miss}) or single electrons, photons or muons in the events. At offline level, the relevant objects to be reconstructed include tracks and primary vertices (Section 3.2.2), electrons and photons (Section 3.2.3), muons

(Section 3.2.4), jets originating from the hadronisation of light quarks (Section 3.2.5) and b -quarks (Section 3.2.6) and E_T^{miss} (Section 3.2.7).

3.2.1 Online trigger objects

The ATLAS TDAQ system performs the online selection of events based on the definition of trigger chains, sequences of algorithms optimised to identify a given type of physics object [75]. After the primary hardware-based selections applied at L1, the HLT chains are typically configured as a sequence of Feature Extraction (FEX) algorithms, where the relevant physical quantities are reconstructed based on the signals in the subdetectors, and Hypothesis algorithms, where the trigger selections are implemented. The following naming convention is used for the chains:

$$[\text{LEVEL}] [\text{TYPE}] [\text{THRESHOLD}] [\text{IDENTIFICATION}] [\text{ISOLATION}] \quad (3.2)$$

where the trigger level (L1 or HLT), type (electron, muon, E_T^{miss} or others), energy threshold, identification and isolation criteria (if present) are listed.

The collection of chains used during the online operation of the detector is known as the ATLAS trigger menu, optimised to fulfil the requirements of a broad range of physics analyses and operational purposes. The list below provides a brief description of the triggers that are relevant for the searches presented in this thesis, namely electron, photon, muon and E_T^{miss} chains:

Electrons and photons The online trigger chains targeting electron and photon candidates are seeded by L1 algorithms that identify RoIs with significant energy deposits in the calorimeters (L1Calo). As shown in Figure 3.3, trigger towers measuring 0.1×0.1 in η and ϕ are formed in both ECAL and HCAL, with a pseudorapidity range $|\eta| < 2.5$. A sliding window procedure is used to select blocks of 4×4 towers where the total energy in at least one of the central pairs (horizontal or vertical) exceeds a fixed threshold. Isolation selections are applied by using the energy deposits in the external ring of the 4×4 blocks, and a veto on significant energy deposits in the HCAL is added to suppress hadronic showers.

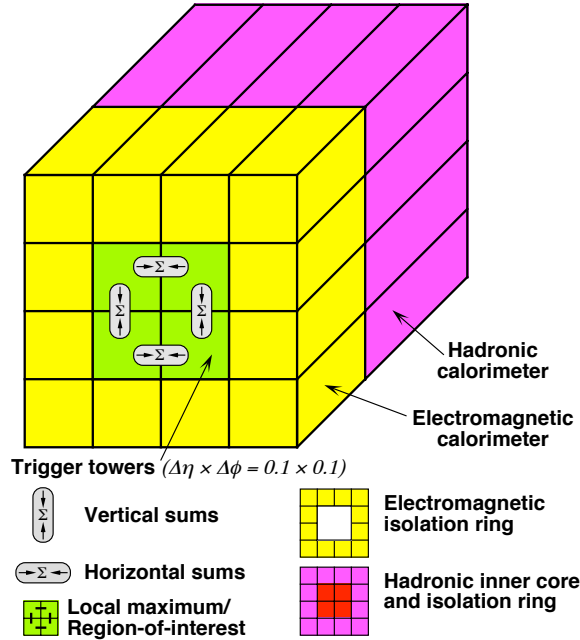


Figure 3.3: Scheme of a 4×4 block of trigger towers employed by the L1Calo trigger algorithms. [75].

The RoIs defined at L1 are passed to the HLT, that applies an additional sequence of selections using algorithms that closely resemble the offline ones (see Section 3.2.3). The requirement of a track matched to the calorimeter cluster is introduced for all electron chains, to distinguish them from photon candidates. The author has contributed to a variety of tasks related to the electron and photon triggers, including a study of the online rate of a single electron trigger chain as a function of the transverse energy threshold, which is discussed in Appendix A.

Muons The L1 trigger identifies muon candidates by requiring the coincidence of hits in the RPC or TGC chambers, and an estimate of the transverse momentum of the particle is obtained by measuring the deviation of the trajectory with respect to a straight line. The HLT receives the ROI information and uses the precision chambers, MDTs and CSCs, to apply further selections on the candidate, with a two-stage approach similar to the one of the electron and photon chains. The tracks from the Muon Spectrometer are matched and combined with those in the

Inner Detector, and additional isolation variables can be used to reduce the number of fake candidates.

Missing transverse momentum The computation of the E_T^{miss} performed by the L1 trigger employs the same energy deposits in 0.1×0.1 towers used for the electron and photon chains. To maximise the coverage, all layers of the ECAL and HCAL for $|\eta| < 4.9$ are employed. The HLT algorithms use as input only the signals provided by the calorimeters, with no RoI information due to the global nature of the E_T^{miss} variable. Different methods are employed for the reconstruction of the E_T^{miss} , based on cells, jets or energy clusters, with dedicated techniques to correct for pileup effects.

Trigger efficiency and scale factors

The most relevant parameter to describe the performance of the trigger chains is the selection efficiency ϵ , defined as the fraction of events where the presence of a real object¹ is successfully identified by the online algorithms.

The efficiency of the chains is typically studied as a function of the transverse momentum of the associated offline objects in the event, as shown in Figure 3.4 for the cases of electrons, muons and E_T^{miss} . The efficiency of E_T^{miss} chains is measured in events satisfying lepton trigger requirements, while for electrons and muons the tag-and-probe method in $Z \rightarrow ee$ and $Z \rightarrow \mu\mu$ events is used [75]. Since the selections are applied based on online energy measurements, it is natural to obtain turn-on curves with a step-like behaviour close to the online threshold of the chain, and a smoothed profile due to finite resolution effects. Both electron (Figure 3.4a) and E_T^{miss} (Figure 3.4b) triggers have high efficiencies above the turn-on, although especially in the case of E_T^{miss} triggers a tight offline selection is necessary. On the contrary, the L1 muon trigger efficiency is limited in both barrel (Figure 3.4c) and end-cap (Figure 3.4d) regions, mainly due to geometrical acceptance effects.

¹For the purpose of the definition of the trigger efficiency, the concept of physics object is extended to event-level quantities such as the E_T^{miss} .

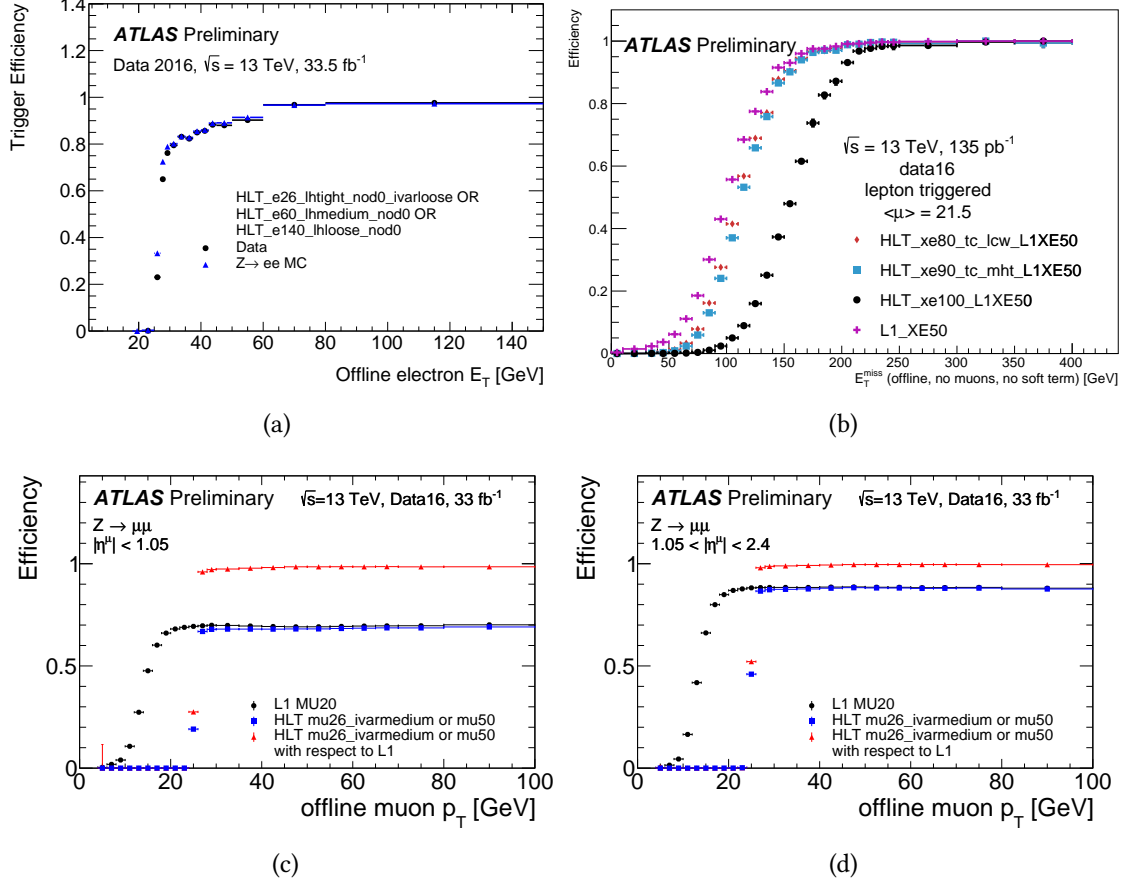


Figure 3.4: Trigger efficiency as a function of offline variables for electrons (a), E_T^{miss} (b), and muons in the barrel (c) and end-caps (d). Various types of online E_T^{miss} algorithms are compared in Figure (b), while for electrons and muons a logic OR of chains with different E_T thresholds and isolation requirements is used [114].

Finally, by comparing the trigger efficiency in data and simulation it is possible to obtain calibration scale factors for both electrons and muon chains, essential to improve the data-MC agreement in the analysis selections.

3.2.2 Tracks and primary vertices

Electrically charged particles release localised ionisation signals (hits) in the Inner Detector, which is able to measure the positions of the hits with variable precision depending

on the granularity of the corresponding layer (see Section 2.3.3). By combining the individual hits, it is hence possible to identify tracks that correspond to the trajectories of the particles. The baseline track reconstruction algorithms in ATLAS [115] follows an inside-out approach where the initial track candidates are formed by at least 3 hits in the silicon detectors, and are subsequently extrapolated to the outer silicon layers and the TRT. The track finding procedure is then completed by an outside-in algorithm, which uses TRT hits as seeds and extends them towards the inner layers.

Due to the magnetic field produced by the solenoid, the tracks follow a characteristic helicoidal trajectory whose curvature is inversely proportional to the momentum of the particle. A track is fully described by five perigee parameters measured at the point of closest approach to the z -axis:

$$(\theta, \phi, q/p, d_0, z_0)$$

where θ and ϕ are the longitudinal and azimuthal angles, and q/p is the ratio between the charge and the momentum of the particle. The quantities d_0 and z_0 are known as transverse and longitudinal impact parameters, and represent the transverse and z projections of the minimum distance between the track and the centre of the detector.

The tracks reconstructed by the above algorithms can be used to identify the presence of vertices formed by collisions or decays of particles in the event. The vertexing procedure [116] uses vertex finding algorithms, that associate the tracks to a set of vertex candidates, and fitting algorithms, that determine the position of the vertices and the associated uncertainties. The number of primary vertices in each event is correlated to the $\langle\mu\rangle$ parameter, which describes the average number of interactions per bunch crossing (see Section 2.1.2), and is used as a direct measurement of the pileup for a variety of calibration purposes. The vertex associated to the hard scattering interaction, or Primary Vertex (PV), is selected as the one for which the sum of the squared momenta of the associated tracks ($\sum p_T^2$) is the largest. After the PV is identified, it is useful to express the impact parameters d_0 and z_0 of the tracks with respect to its position.

3.2.3 Electrons and photons

The characteristic experimental signature of electrons and photons in ATLAS consists in an electromagnetic shower in the ECAL and, for electrons, an associated track in the Inner Detector. In both cases the selection procedure [117] begins with a sliding window algorithm that searches for clusters of energy deposits in the calorimeter, scanning it in blocks of 3×5 cells with individual transverse size of 0.025×0.025 in η and ϕ .

The discrimination between electrons and photons is implemented by matching the calorimeter clusters with the Inner Detector tracks. The simplest photon candidates are clusters with no associated tracks, but it is also possible to reconstruct converted photons that produce an electron-positron pair before reaching the ECAL. The latter case can be identified from the presence of two oppositely-charged tracks matched to the cluster or, if the opening angle of the electron-positron pair is large, a single track with no hits in the innermost silicon layers [118]. Electron candidates are instead reconstructed as clusters matched to a track with a sufficient numbers of silicon hits. After the matching, the calorimeter cluster is rebuilt using blocks of 3×7 cells in the barrel and 5×5 cells in the end-caps.

The computation of the total energy of the clusters includes corrections from the pre-shower sub-detector, to quantify the energy lost by the particles before the ECAL, and from the cells surrounding the bulk of the cluster, to estimate the lateral and longitudinal leakage of the shower. For electrons, the final energy is obtained by combining the cluster energy with the momentum of the track, while the η and ϕ coordinates are derived exclusively from the track². The energy calibration is performed using a mixture of Monte Carlo based algorithms and data driven corrections derived from $Z \rightarrow ee$ events [119, 120].

Once the electron and photon candidates are reconstructed, additional selections are applied in order to suppress the backgrounds from the misidentification of different types of objects (fakes). The identification (ID) algorithms exploit variables related to the shape of the electromagnetic showers, track quality and matching requirements

²If the track has no hits in the silicon detectors, the η coordinate is derived from the cluster.

and, for electrons, information about the transition radiation released in the TRT. The electron identification is based on a likelihood approach (LH) built from the probability distributions of discriminating variables in signal and background candidates. For both electrons and photons a set of ID working points (WPs) are defined, with different selection efficiency and purity³. Similarly, isolation variables and WPs are defined using information from both Inner Detector tracks and calorimeter clusters.

The offline selection efficiency of electrons and photons can be factorised as:

$$\epsilon_{\text{tot}} = \epsilon_{\text{reco}} \times \epsilon_{\text{ID}} \times \epsilon_{\text{iso}} \quad (3.3)$$

where each step of the selection procedure contributes separately. The reconstruction and identification efficiency in 2016 data is shown in Figure 3.5 for electrons and unconverted photons, highlighting a data-MC discrepancy in the electron ID performance caused by a mis-modelling of the TRT conditions. Calibration corrections are derived in the form of efficiency scale factors, that are applied to the Monte Carlo to match the observed performance in data.

3.2.4 Muons

Muons appear as charged particle tracks in the Inner Detector and Muon Spectrometer, with a finite curvature caused by the magnetic field of the solenoid and toroid systems. Their selection procedure [123] begins with two independent track fits in the ID and MS, that are then combined using different algorithms depending on the signature in each sub-system. The ATLAS detector is able to reconstruct the following types of muon candidates:

Combined When tracks are found in both ID and MS, a global refit is performed in order to obtain a combined muon track that describes the trajectory of the particle through the entire detector, taking into account the energy loss in the calorimeter. This signature provides a good momentum resolution in all p_T ranges, driven

³The purity is defined the fraction of real electrons (photons) among the selected objects.

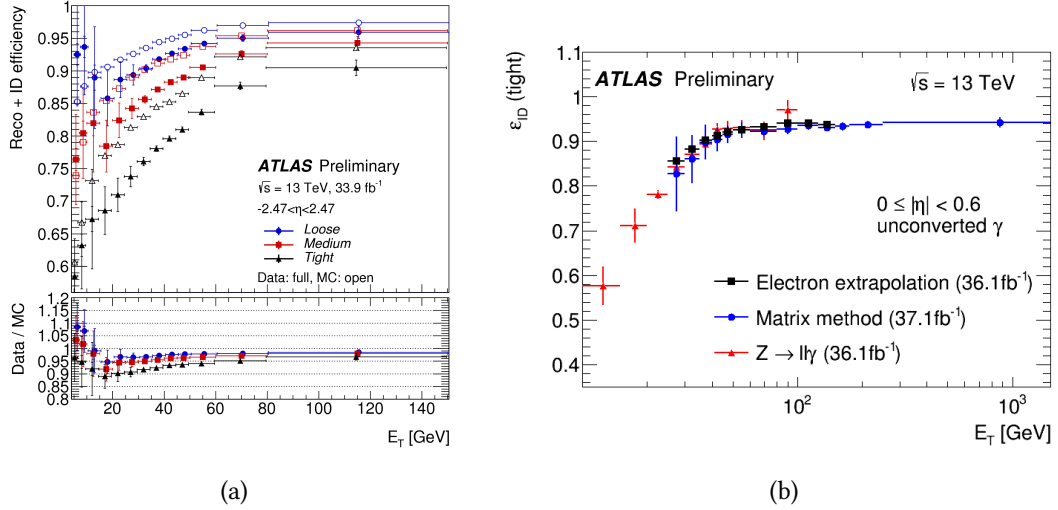


Figure 3.5: Reconstruction and identification efficiencies for electrons (a) and for unconverted photons (b) [121]. The electron efficiency measured in $Z \rightarrow ee$ events in both data and Monte Carlo, while the photon efficiency is measured through different data-driven techniques [122] in the central pseudorapidity region ($|\eta| < 0.6$).

by the ID at low p_T and by the MS at high p_T . The longitudinal acceptance of combined muons is limited by the ID ($|\eta| < 2.5$).

Extrapolated Muons in the forward region ($2.5 < |\eta| < 2.7$) yield a track in the MS but lie outside the acceptance of the ID. Their trajectory is reconstructed from the MS track, with a loose requirement on its compatibility with the interaction point in the centre of the detector.

Segment tagged Tracks in the ID are classified as muons if a corresponding hit in the inner layer of the MS is found. In general, this type of signature occurs only for muons with low p_T or as a result of acceptance cracks in the MS.

Calorimeter tagged Similarly, tracks in the ID are classified as muons if they can be matched with an energy deposit in the calorimeter compatible with the signature of a Minimum Ionising Particle (MIP), with no associated MS track. This happens primarily in the central pseudorapidity region ($|\eta| < 0.1$) due to the presence of a crack in the barrel of the MS.

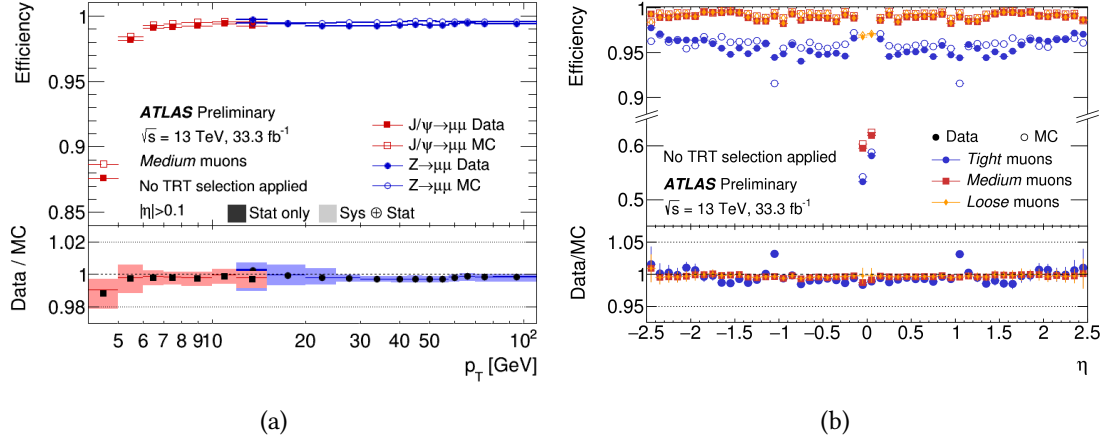


Figure 3.6: Muon reconstruction and identification efficiency as a function of p_T (a) and η (b) in the ATLAS detector [124].

Additional identification selections are applied in order to separate prompt muons from various background sources, mostly pion and kaon decays. The selections employ track quality variables in both ID and MS, including the normalised χ^2 of the combined track fit, and other requirements on the compatibility between the charge and momentum measurements in the two sub-systems. In addition, track-based and calorimeter-based isolation variables are used to further select prompt muons, produced at significant angular distance from other objects in the event.

Similarly to the case of electrons and photons, a set of identification and isolation WPs are defined to meet the requirements of different ATLAS analyses. The performance is calibrated using the tag-and-probe method in $Z \rightarrow \mu\mu$ or $J/\psi \rightarrow \mu\mu$ events, and scale factors are obtained for each step of the selection process. The reconstruction and identification efficiencies as a function of p_T and η are shown in Figure 3.6.

3.2.5 Jets

As a result of the confinement properties of QCD, elementary quarks and gluons from proton collisions generate collimated sprays of particles (jets) [125] in the events, which appear as showers in the calorimeter system associated to tracks in the Inner Detector.

The analyses presented in this thesis employ Calorimeter (Calo) jets, that reconstruct the four-vector of the original partons by measuring the energy of the showers in the ECAL and HCAL.

Jet reconstruction

The energy of the showers is measured by forming topological clusters [126, 127] in the calorimeters, similarly to what is done for the triggers described in Section 3.2.1 but with a three-dimensional structure. The clusters are built through an iterative algorithm that begins with the identification of seed cells with energy deposits above a high threshold t_{seed} and continues by adding neighbouring cells with a lower threshold t_{cell} . Once the bulk of the cluster is formed, an external layer of cells is also added in order to include potential leaks of the shower.

The collection of topological clusters in each event is used as input for jet-finding algorithms, which treat them as massless objects with four-vectors of energy $E = \sum_i E_{\text{cell}}^i$ and angular coordinates determined by their position in the detector. The standard choice of the ATLAS Collaboration is the anti- k_T algorithm [128], where a collection of jets is formed through an iterative recombination of the input clusters. The characteristic shape of the output jets is a circular cone with angular width driven by a free parameter R , which is set to 0.4 in all the analyses discussed in this thesis. As discussed in Ref. [125], the anti- k_T algorithm is infrared and collinear safe, meaning that the output jet collection remains unchanged if the event is modified by adding a collinear splitting of a parton or an extra soft emission in the final state.

Jet calibration

Jets obtained from topological clusters are reconstructed at the characteristic energy scale of electromagnetic objects (EM scale), which underestimates the hadronic energy deposits due to the non-compensation of the calorimeter and to other detector-related effects. The jet calibration procedure used for the analysis of 2015 and 2016 data follows the Electromagnetic + Jet Energy Scale (EM+JES) scheme [129], where a set of corrections

parametrised by the p_{T} and η of the jets are applied to match the energy of the initial partons. The Jet Energy Scale is defined by the following sequence of corrections:

Vertex correction The four-vectors of the jets reconstructed by the anti- k_{T} algorithm, which are initially pointing to the geometrical centre of the detector, are adjusted to point to the primary vertex in the event.

Pileup correction The effect of pileup on the energy of the jets is mitigated using an area-based subtraction procedure [130], based on the average energy deposits in the calorimeters produced by the underlying event.

Jet energy and η correction Jets are further calibrated by applying energy and pseudorapidity corrections derived from Monte Carlo simulation, where the reconstructed kinematical properties are compared to the true values in bins of reconstructed p_{T} and η .

Global sequential correction Additional corrections, known as Global Sequential Corrections (GSC) [131], are applied based on individual jet properties, such as the fraction of energy deposited in different calorimeter layers or the number and type of associated tracks.

In-situ calibration A final set of in-situ corrections accounts for discrepancies between data and simulation in the measurement of the p_{T} of the jets [132]. The corrections are obtained from multijet and $\gamma/Z + \text{jet}$ events, where the momentum of a probe jet is balanced against a well-measured reference object. The jet response function, defined as $p_{\mathrm{T}}^{\text{probe}}/p_{\mathrm{T}}^{\text{ref}}$, is shown in Figure 3.7 as a function of p_{T} and η .

Jet cleaning selections and Jet Vertex Tagger

Dedicated selections are applied to reduce the background of fake jets, that may arise from a variety of sources ranging from hardware effects, LHC beam-gas interactions or

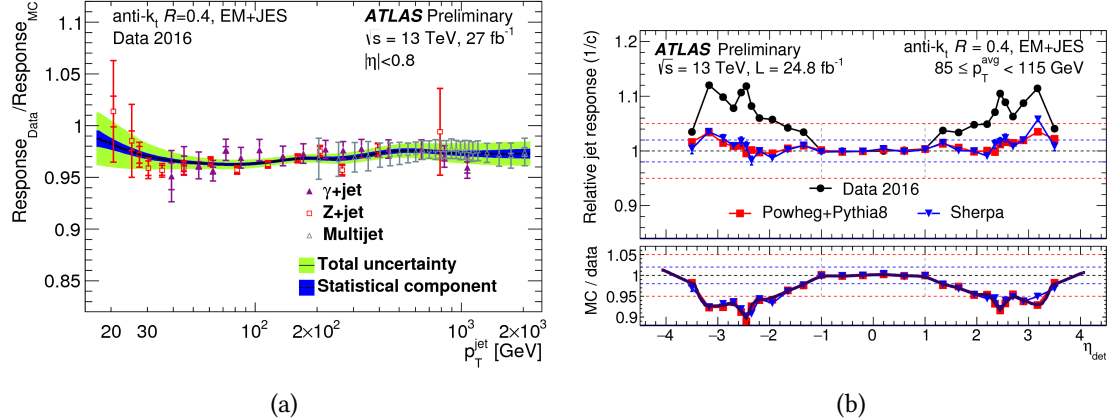


Figure 3.7: Momentum (a) and pseudorapidity (b) dependence of the jet response in the ATLAS detector [133]. The left plot shows the ratio of the jet response in data and MC obtained from the combination of three in situ calibration techniques, while in the right plot the relative jet response is shown as a function of η in di-jet events for data and two different Monte Carlo samples.

cosmic ray showers. Quality requirements are introduced for a variety of parameters, including the fraction of energy deposited in the different layers of the calorimeter system and the fraction of jet p_T measured by the tracks in the Inner Detector. The above requirements define a “bad jet” condition, which is used in the analyses to suppress the fake contamination.

In addition, a Jet Vertex Tagger (JVT) [134] variable is developed in order to remove jets produced by pileup effects in the kinematic range $20 < p_T < 60$ GeV and for $|\eta| < 2.5$. JVT is a multivariate discriminant built from variables related to the fraction of charged tracks in the jets that point to the primary vertex, indicating the compatibility of the jet with originating from the hard scattering interaction. Particular efforts have been dedicated to ensure that JVT is stable as a function of the number of primary vertices in the event, to avoid the introduction of pileup-dependent biases. The performance of the JVT selections is calibrated using $Z \rightarrow \mu\mu + \text{jets}$ events, and efficiency scale factors are derived in bins of jet p_T for a set of WPs.

3.2.6 *b*-tagging

The ability to identify the products of bottom quark hadronisation (*b*-hadrons) is crucial for the analyses presented in this thesis and for several more areas of research within the ATLAS Collaboration. Bottom quarks generate hadronic jets (*b*-jets) with the same mechanism of the other coloured particles, so they are reconstructed through the standard procedure described in Section 3.2.5. Once the jets are formed, dedicated *b*-tagging algorithms [135] are employed to assess the presence of a *b*-hadron within their cone.

b-tagging algorithms

The characteristic properties of *b*-jets in ATLAS are shown in Figure 3.8, where a comparison with a standard light jet is presented. Due to their lifetime of the order of 10^{-12} s, *b*-hadrons can travel a measurable distance in the detector before decaying, yielding a secondary vertex within the jet cone. In addition, the impact parameter of the tracks from the *b*-hadron decay is expected to differ from zero, providing a useful tool for jet flavour discrimination. A similar experimental signature is obtained for jets from charm quark hadronisation (*c*-jets), with lower average displacement of the secondary vertex due to the shorter lifetime of *c*-hadrons. This implies that dedicated algorithms can be developed also to identify *c*-jets [136], but at the same time it introduces a significant source of background for *b*-tagging.

The ATLAS Collaboration has developed three types of *b*-tagging algorithms that identify *b*-jets following alternative approaches. The outputs of these algorithms are then combined into a single multivariate tagger, MV2, that provides the best discriminating power between the various jet flavour hypotheses. A brief overview of the major characteristics of each algorithm is given below:

IP2D and IP3D The first approach involves the use of the impact parameters of the tracks as main discriminating variables, since they are expected to be larger for tracks that originate from the decay of *b*-hadrons. The significance of the transverse impact parameter of the tracks, d_0/σ_{d_0} , is employed by both IP2D and IP3D

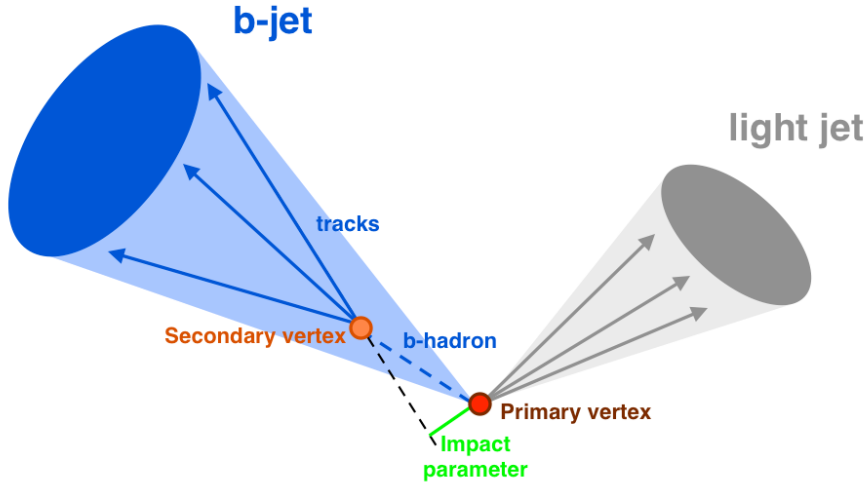


Figure 3.8: Comparison between the characteristic properties of light jets and b -jets in the ATLAS events. The trajectory of the b -hadron, the secondary vertex and the impact parameter of a track from its decay are highlighted.

taggers, and the latter uses also the longitudinal impact parameter significance, $z_0 \sin \theta / \sigma_{z_0 \sin \theta}$. The probability distributions of these quantities are employed to define ratios of b -jet and light-jet hypotheses, which are then combined into a single discriminant.

Secondary Vertex Finding Algorithm (SV) A second possibility is to perform an explicit reconstruction of secondary vertices within the cone of the jets. The SV algorithm uses as input all pairs of tracks associated to the jet, forming two-track vertices that are then discarded based on their compatibility with background sources such as hadronic interactions with the detector, photon conversions or decays of long-lived particle (kaons or Λ baryons). Additional quality requirements on the tracks are introduced to suppress the background from pileup vertices, and to reduce the probability of reconstructing fake vertices in dense track environments.

Decay Chain Multi-Vertex Algorithm (JetFitter) A third type of algorithm, JetFitter [137], performs a reconstruction of the full decay chain of b -hadrons inside the jets based on their expected topological structure. The trajectory of the b -hadron and

of its decay products is extracted using a Kalman filter [138].

Mutivariate Algorithm (MV2) A Boosted Decisions Tree (BDT) algorithm [139], MV2, is implemented with the ROOT TMVA package [140] to combine the output of the three taggers described above. The algorithm is available in three different versions, MV2c00, MV2c10 and MV2c20, where the numbers indicate the fraction of c -jets (in %) that are present in the background training sample in addition to a majority of light flavour jets. The MV2c10 tagger, trained on a sample with 10% c -jets and 90% light jets, is the baseline choice for the analysis of 2015 and 2016 data.

The performance of different configurations of the MV2 algorithm in $t\bar{t}$ events is shown in Figure 3.9, where the efficiency of correctly identifying b -jets is compared with the rejection probability of c -jets and light jets, defined as the inverse of the corresponding mis-tag rates. As expected, the versions of the algorithm with more c -jets in the background training sample yield a better c -jet rejection and a worse light jet rejection, while the opposite happens if no c -jets are included in the training. Benchmark cuts on the output of the MV2c10 algorithm are used to define a set of b -tagging WPs, optimised to provide specific efficiency values (60%, 70%, 77% and 85%) on a reference $t\bar{t}$ sample. In addition, to correct for a degradation of the b -tagging performance at high values of the jet p_T , a more sophisticated set of WPs is defined by modifying the cut threshold of MV2c10 as a function of the p_T , yielding a constant tagging efficiency in all kinematic regimes. More detail on the performance of b -tagging algorithms is provided in Chapter 4.

***b*-tagging calibration**

In order to apply b -tagging requirements in physics analyses, the performance of the algorithms must be accurately measured in data and Monte Carlo simulation. The first parameter to be measured is the b -jet efficiency, but it is also important to determine the probability of mis-tagging c -jets (referred to as c -tagging efficiency) and light jets

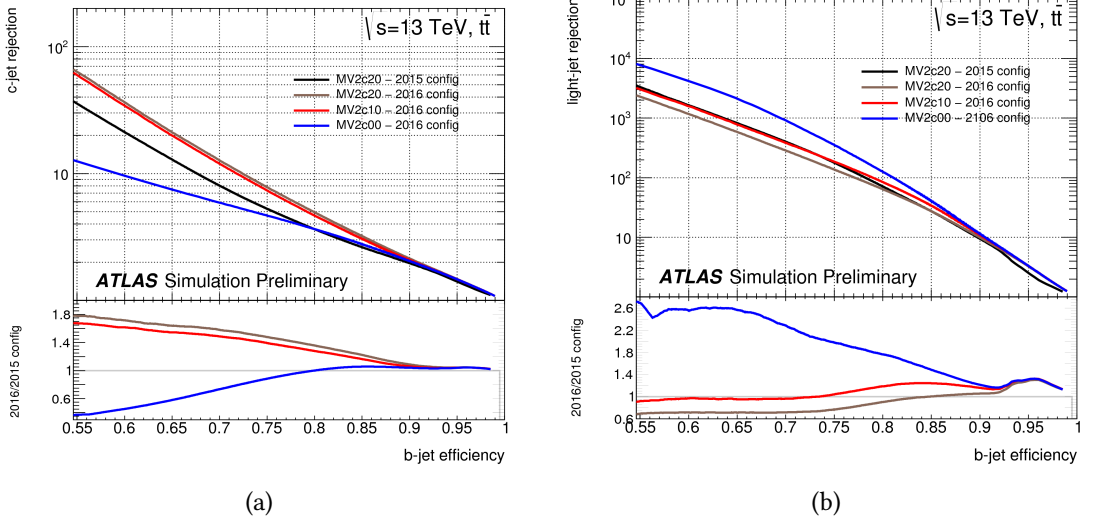


Figure 3.9: Performance of the MV2 b -tagging algorithm in $t\bar{t}$ events for different fractions of c -jets in the background training sample [141]. The b -tagging efficiency is shown versus the c -jet (a) and light jet (b) rejection factors.

(mis-tag rate).

A variety of techniques have been developed to measure the above parameters in data, allowing to derive calibration corrections in terms of efficiency scale factors for real b , c and light jets separately. The baseline b -jet calibration, performed by selecting $t\bar{t}$ events in di-leptonic final states [142], is able to achieve a precision of the order of a few % in the jet p_T range between 20 and 300 GeV. The reach can be extended to approximately 500 GeV by performing a similar analysis in semi-leptonic events, which benefits from more available statistics. The c -tagging efficiency is measured by selecting events with c -jets produced in association with a W boson decaying into a lepton and a neutrino [143]. The presence of a c -jet is determined by reconstructing a soft muon from the semi-leptonic decay of the c -hadron, and the purity of the sample is improved by correlating the charge of the two leptons in the event. Finally, a negative-tag method [144] is employed to measure the mis-tag rate that originates mainly from tracking resolution effects. Several more calibration strategies have been studied within the ATLAS Collaboration, and a comprehensive overview of the most relevant ones is provided in Ref. [135].

3.2.7 Missing transverse momentum

Thanks to the hermetic coverage of the ATLAS detector, the presence of invisible particles in the events can be assessed by reconstructing a significant momentum imbalance in the transverse plane. Indeed, while the longitudinal boost of the hard scattering products varies on an event-by event basis, the net transverse momentum of the reconstructed objects in the final state is expected to be balanced within finite resolution effects, unless at least one particle has escaped the detection.

The momentum imbalance in the transverse plane is measured by the two-dimensional missing transverse momentum vector, $\mathbf{p}_{\text{miss}}^T$ [145], defined as the negative vectorial sum of the x - y components of the four-momenta of the visible objects in the event:

$$\mathbf{p}_{\text{miss}}^T = - \sum_{\text{all}} \mathbf{p}_{\text{obj}}^T. \quad (3.4)$$

The magnitude of $\mathbf{p}_{\text{miss}}^T$ is known as missing transverse momentum or missing transverse energy (E_T^{miss}), and the azimuthal coordinate of the vector is simply given by:

$$\phi_{E_T^{\text{miss}}} = \arctan(p_{\text{miss}}^y / p_{\text{miss}}^x) \quad (3.5)$$

where the x and y projections of $\mathbf{p}_{\text{miss}}^T$ are used.

The sum in Equation 3.4 can be split in a hard term that includes all the relevant physics objects reconstructed by the detector (electrons, muons, τ leptons, photons, jets) calibrated at their appropriate energy scale, and a soft term that contains the remaining detector signal objects in the event. The individual contributions to the hard term are added in sequence following a fixed order: electrons, photons, hadronically decaying τ leptons, jets and muons. During the reconstruction process, the algorithm solves the overlaps between different types of objects by keeping those that appear earlier in the chain. For the analyses presented in this thesis the hadronic τ term is not included in the computation, because explicit τ reconstruction is not employed, so any hadronic τ in the events is reconstructed as a jet and contributes to the jet term of the E_T^{miss} . The soft term can be reconstructed using ID tracks (track-based soft term) or calorimeter signals (calorimeter-based soft term): for the analysis of 2015 and 2016 data, the track soft term

is used as a baseline choice due to its lower sensitivity to pileup effects.

The performance of the E_T^{miss} is studied in events where invisible particles are present, such as leptonically decaying W or $t\bar{t}$ samples, in order to validate the reconstruction algorithms and remove potential biases in the absolute scale. In parallel, a measurement of the resolution is obtained from the width of the E_T^{miss} distribution in $Z \rightarrow \ell\ell$ events where no real sources of momentum imbalance are expected.

Chapter 4

***b*-tagging performance studies with Monte Carlo simulations**

This chapter presents a study of the performance of the baseline *b*-tagging algorithm in ATLAS, MV2c10, with focus on the boosted kinematic regime of the *b*-jets. Since the data-based calibration analyses have a limited reach at high p_T due to the small size of the available *b*-jet sample [135], the study is entirely performed using MC simulations, where *b*-jets with p_T up to a few TeV can be obtained. The workflow of the analysis is outlined in Section 4.1 together with a description of the technical aspects, while Section 4.2 is dedicated to a full discussion of the results.

4.1 Analysis strategy

As described in Section 3.2.6, the MV2c10 algorithm computes a multivariate *b*-tagging weight for each input jet, based on a set of variables related to the jet and to the associated tracks. Since these quantities are reconstructed by the detector with finite accuracy, their measured values carry an experimental uncertainty that affects the resulting MV2c10 weight, causing a systematic variation of the performance of the tagger. The purpose of the study presented in this chapter is to evaluate the impact of various sources of systematic uncertainty on the performance of MV2c10, quantifying the resulting uncertainty

on the tagging efficiency as a function of the p_T of the jets. The study is particularly relevant for jets with p_T higher than a few hundred GeV, for which the data-based calibration analyses are unable to provide a direct measurement of the b -tagging performance¹.

4.1.1 Workflow and object definitions

The analysis is performed with a software that runs the b -tagging algorithm on a set of benchmark MC samples, computing the value of the output MV2c10 discriminant for all input jets in each event. The output discriminant is built both for an input dataset with nominal track and jet collections, and for one where the input collections are modified according to the expected experimental uncertainties on tracks and jets (see Section 4.1.3).

The performance of the MV2c10 tagger is studied separately for real b , c and light jets (see Section 3.2.6) with flavour determined at truth level by performing an angular (ΔR) matching between jets and b or c -hadrons in the events. The b -tagging decision is taken by applying a cut on the MV2c10 outputs of each jet, and efficiency distributions as a function of the jet p_T are derived for each different source of systematic uncertainty. By comparing the efficiency values in each bin of p_T , it is hence possible to assess the impact of each variation on the performance of the MV2c10 tagger.

The studies are entirely based on Calo jets reconstructed through an anti- k_T algorithm with radius $R = 0.4$, as introduced in Section 3.2.5. Tracks are required to satisfy the “Loose” quality criteria [146], which corresponds to the following selections:

- $p_T > 400$ MeV and $|\eta| < 2.5$.
- At least 7 hits in Pixel and SCT layers.
- A maximum of 1 shared module (Pixel hit shared by two or more tracks, or double hit in a single SCT layer).

¹For reference, the baseline b -tagging efficiency calibration [135] has a b -jet p_T reach of 300 GeV.

- A maximum of 2 silicon holes (Pixel or SCT layers with no hit in correspondence with the track trajectory) and 1 pixel hole.

4.1.2 Monte Carlo samples

The analysis of the performance of the MV2c10 algorithm requires large samples of b -jets covering a wide range of kinematic regimes, with p_T distributed from a minimum of 20 GeV up to a few TeV. In order to obtain them, the following MC samples are used:

Inclusive $t\bar{t}$: The pair production of Standard Model top quarks yields two bottom quarks in each event, originating from the $t \rightarrow Wb$ decay. The majority of the b -jets have p_T values below the top mass scale, but occasionally also b -jets with higher boosts are produced. The nominal $t\bar{t}$ sample in ATLAS is simulated using Powheg [107] as event generator and Pythia 6 for the parton showering [103, 104], with the EvtGen [110] software regulating the decays of the b -hadrons. Two alternative sample that uses Pythia 8 or Herwig [105] instead of Pythia 6 are also available for comparison.

$Z' \rightarrow bb$: The decay of a Z' resonance into a pair of bottom quarks provides a sample of b -jets with average p_T approximately given by $m_{Z'}/2$. The the studies presented in this chapter employ a $Z' \rightarrow bb$ sample with $m_{Z'} = 5$ TeV, where a large amount of b -jets with high p_T is obtained. The sample is simulated with Pythia 8 interfaced with EvtGen.

$W' \rightarrow tb$: A third sample of b -jets is obtained by simulating the decay of a W' resonance into a top-bottom pair, with the top decaying into a W boson and a bottom quark. The peculiarity of this sample is that 50% of the b -jets originate from the prompt decay of the W' , while the remaining 50% is produced through the decay of the top quark. W' samples are generated with MadGraph [106] interfaced with Pythia 8 and EvtGen.

4.1.3 Systematic uncertainties

The performance of b -tagging algorithms is affected by a variety of systematic effects related to the input tracks [147] or to global jet properties. This paragraph presents the sources of systematic uncertainty that are considered for the present study, providing a description of their origin and their expected impact.

Impact Parameter Resolution

The transverse and longitudinal impact parameters of the tracks (d_0 and z_0) are essential for the computation of the multivariate MV2c10 weight, because the tracks from the decay of b -hadrons are distanced from the primary vertex.

The intrinsic resolutions of d_0 and z_0 are measured in multi-jet and $Z \rightarrow \mu\mu$ events [148], and are found to be larger in data compared to MC simulations. A dedicated analysis is performed to extract d_0 and z_0 smearing corrections, to be applied to each track in order to reproduce the resolution observed in data. Alternatively, since the resolution in MC is influenced by the modelling of the inactive modules of the Pixel detector, a correction can also be derived by re-evaluating the track parameters after randomly disabling a 5% fraction of them. In both cases, an impact on the performance of the MV2c10 algorithm is expected.

Fake Tracks

Uncorrelated hits in the Inner Detector can cause the reconstruction of fake tracks as a result of combinatorial effects, particularly relevant in high pileup conditions. Under the assumption that the number of real (i.e. non-fake) tracks is proportional to the pileup parameter μ , the number of fakes can be estimated by measuring the total number of tracks as a function of μ , attributing any deviation from a linear behaviour to the fake component [147]. The difference between the number of fake tracks in data and MC is found to be around 30% independently of p_T and η , so a systematic variation is implemented by randomly removing 30% of them from the nominal input collection in the MC samples.

Track Reconstruction Efficiency

Another relevant parameter for the performance of *b*-tagging is the reconstruction efficiency of real tracks, which is affected by the knowledge of the amount of material in the Inner Detector [149]. The associated uncertainty is evaluated as a function of the track p_T and η by measuring the difference in tracking efficiency between the nominal sample and one where additional material is added. Four independent variations are implemented:

- Passive material in the Inner Detector scaled by 5%.
- Passive material in the IBL layer scaled by 40%.
- Passive material in the Patch Panel 0 (PP0) region of the ID scaled by 50%.
- Change in the Geant 4 physics model used for the event reconstruction.

Tracking in dense environments

Specific measurements of the track reconstruction efficiency are performed in the core of hadronic jets [150], where a deterioration of the tracking performance is expected due to the high density of the experimental environment. The fraction of lost tracks is measured in bins of jet p_T in data and MC, and the observed difference is applied as a systematic uncertainty by dropping 0.4% of the tracks within $\Delta R(\text{track}, \text{jet}) < 0.1$.

Weak modes in the Inner Detector alignment

The alignment of the Inner Detector is performed with a track fit procedure [151] based on the minimisation of a χ^2 function, which depends on a set of alignment parameters. The deformations of the detector material that have little or no impact on the value of the χ^2 are known as weak modes, and represent a source of ambiguity in the alignment procedure. As a result, the following potential biases on the performance of the tracking algorithms [152] may occur:

- Charge-antisymmetric bias on the reconstructed q/p ratio of the tracks.

- Bias on the transverse and longitudinal impact parameters (d_0 and z_0).

The impact of the weak mode biases on the performance of MV2c10 is studied by shifting the tracking parameters within the expected systematic uncertainties, evaluating the corresponding efficiency variations.

Jet Energy Scale and Resolution

The calibration of the jets to the appropriate energy scale [153], described in Section 3.2.5, carries an uncertainty that influences their measured momentum, potentially causing a bias in the p_T -binned b -tagging efficiency. The JES uncertainty is implemented based on the results of the calibration studies, in the form of 3 variations that parametrise the effect of a larger number of corrections. Similarly, the resolution of the measured jet energy also carries an experimental uncertainty [154], and the associated effect on the performance of the MV2c10 algorithm is studied.

Jet Angular Resolution

A final uncertainty is associated with the direction of the jet axis, which can be reconstructed either from the energy deposits in the calorimeter or from the tracks in the Inner Detector. The two measurements may differ due to experimental resolution effects, and a smearing factor can be applied to the MC simulation to match the resolution in data, similarly to what is done for the impact parameters of the tracks. The associated systematic uncertainty on the b -tagging is estimated by smearing the ϕ and η values of the jets by gaussian factors of 0.004 and 0.008 respectively.

4.2 Results on b -tagging performance

This section is dedicated to a full discussion of the performance of the MV2c10 b -tagging algorithm, including the analysis of the systematic effects described in the previous paragraphs. As anticipated in Section 3.2.6, the algorithm can be employed with two types of WPs, implemented by defining benchmark selections on the value of the MV2c10

discriminant of the jets. In the fixed cut WPs the selection on the MV2c10 output is a constant value independent of the jet p_T , so the resulting performance may vary in different kinematic regimes. Alternatively, fixed efficiency WPs are defined by scaling the value of the MV2c10 cut as a function of the jet p_T , to ensure that the b -tagging efficiency remains constant over a wide range of momenta. The performance results in this section are presented for a fixed cut WP that yields a b -tagging efficiency of 77%, used for all the analyses described in the next chapters. The case of the fixed efficiency WP, for which similar conclusions can be drawn, is presented in Appendix B.

4.2.1 Nominal performance

Before studying the impact of systematic effects, it is useful to examine the nominal performance of the MV2c10 tagger for different physics processes and for different kinematic regimes of the jets.

The b -tagging efficiency as a function of the jet p_T is shown in Figures 4.1a and 4.1b for the 77% fixed cut and fixed efficiency WPs, comparing the performance in $t\bar{t}$ and $Z' \rightarrow bb$ samples. The general trend of the curves is similar for the two physics processes: the efficiency is relatively low for soft b -jets, it reaches a peak in the p_T range between 50 and 200 GeV and it decreases again for higher boosts of the jets. The performance in $t\bar{t}$ and Z' is comparable up to about 200 GeV, but a major deviation is observed in the high p_T region, where the Z' efficiency is significantly lower. In particular, the fixed efficiency WP is able to yield a constant efficiency only when applied to the $t\bar{t}$ sample (which is used to optimise its p_T -dependent selections), while the Z' curve still shows a significant decrease at high p_T .

Similarly, Figures 4.1c and 4.1d show the nominal c -tagging and mis-tag efficiencies for the 77% fixed cut and fixed efficiency WPs, obtained using a $t\bar{t}$ sample. As expected, the comparison between the two plots indicates that the fixed efficiency WP yields a larger mis-identification efficiency at high p_T for both c -jets and light jets.

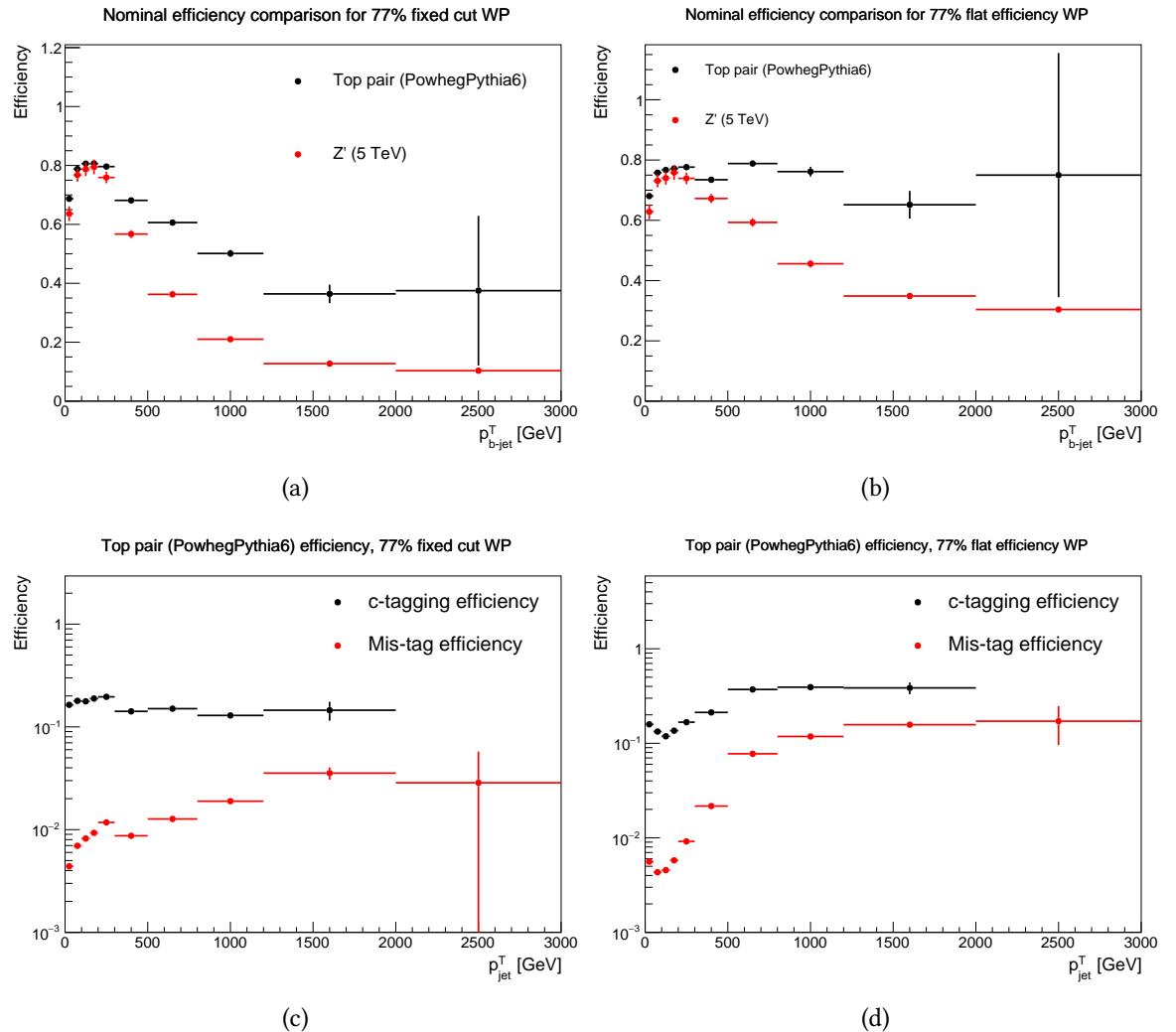


Figure 4.1: Nominal tagging efficiency for different jet types, physics processes and WPs. Figures (a) and (b) show the b -tagging efficiency as a function of the b -jet p_T in $t\bar{t}$ and Z' samples for the 77% fixed cut and fixed efficiency WPs, while the c -tagging and mis-tag efficiencies are compared in Figures (c) and (d) in a $t\bar{t}$ sample for same two WPs.

4.2.2 Relation between b -hadron and b -jet momentum

The discrepancy between the b -tagging performance in $t\bar{t}$ and Z' can be understood by analysing the different substructure of the b -jets in the two physics processes, focusing on the kinematical properties of the b -hadrons, that can be studied using the truth infor-

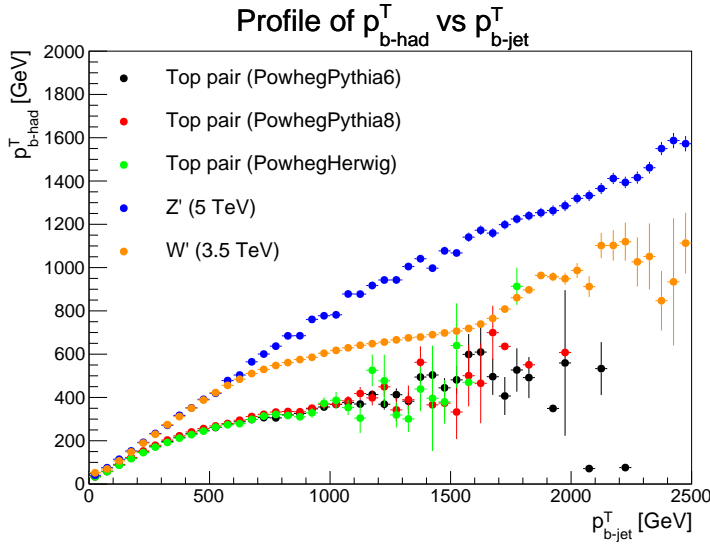


Figure 4.2: Average p_T of the b -hadrons as a function of the p_T of the associated b -jets in $t\bar{t}$ (with Pythia 6, Pythia 8 and Herwig as PS generators), Z' and W' samples. Both quantities in the plot are extracted from the truth information of the MC simulations.

mation in the MC samples.

The average p_T of the b -hadrons as a function of the p_T of the associated b -jets is shown in Figure 4.2 for $t\bar{t}$ (with Pythia 6, Pythia 8 and Herwig as PS generators), Z' and W' samples. The relation is approximately linear for Z' , while for $t\bar{t}$ the slope of the curve is lower and tends to decrease at high p_T . Lastly, the W' sample exhibits an intermediate behaviour between the two. It is important to emphasise that the $t\bar{t}$ distributions are independent of the chosen PS generator, proving that the observed discrepancies are not related to different types of hadronisation or fragmentation models in the nominal $t\bar{t}$ and Z' samples, but rather to the intrinsic features of the physics processes.

Further details are provided in Figure 4.3, where the distribution of the ratio between b -hadron and b -jet p_T is shown separately in individual bins of b -jet p_T for the same four MC samples. When the 50-100 GeV bin is considered (Figure 4.3a) the distributions appear similar, while for higher p_T ranges the discrepancies between the different physics processes become progressively more relevant. In the 1000-1100 GeV bin (Figure 4.3d) the $t\bar{t}$ and Z' histograms have different peaks, while interestingly the W' histogram

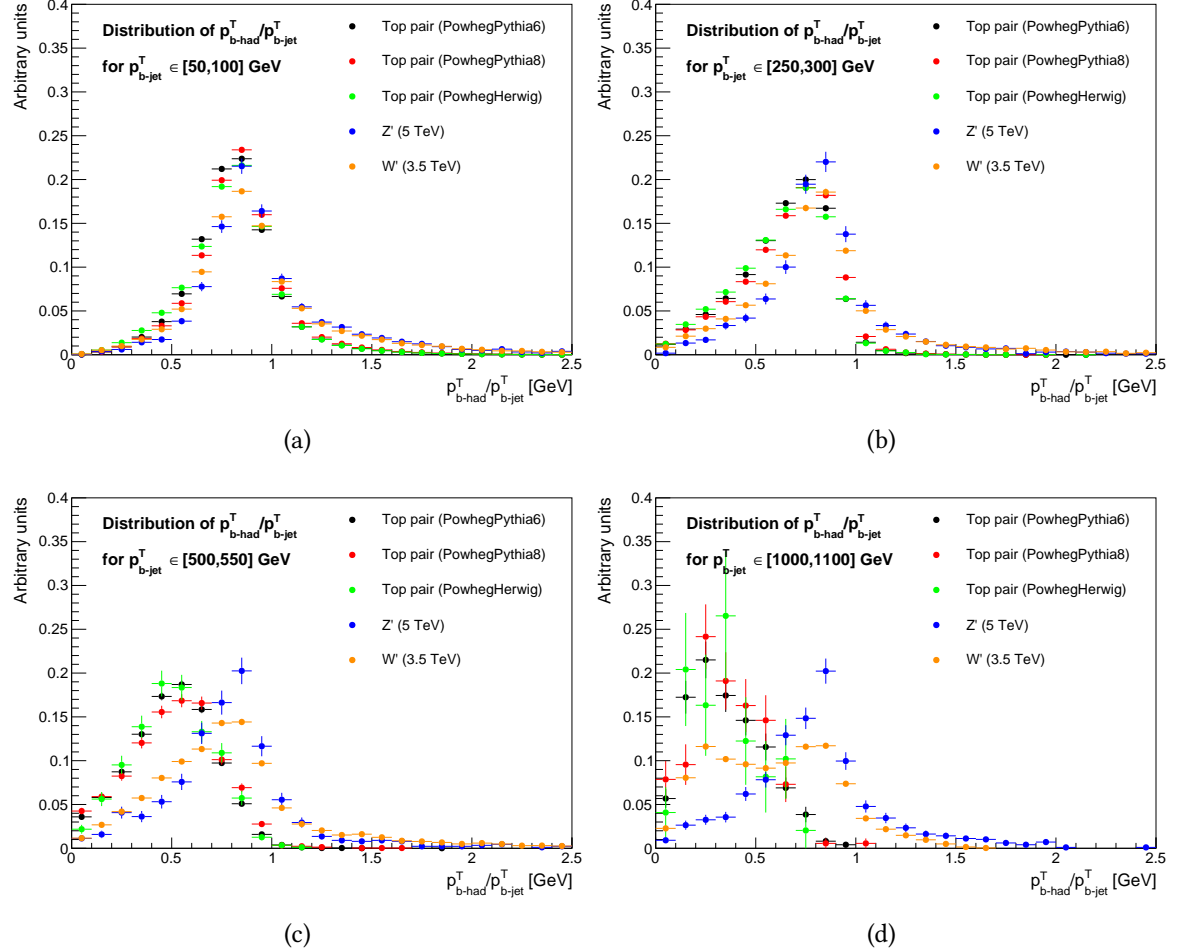


Figure 4.3: Distribution of the ratio of b -hadron and b -jet p_T in $t\bar{t}$ (with Pythia 6, Pythia 8 and Herwig as PS generators), Z' and W' samples in the b -jet p_T ranges 50-100 GeV (a), 250-300 GeV (b), 500-550 GeV (c) and 1000-1100 GeV (d). The histograms are obtained using the MC truth information and are normalised to unit area.

shows a hybrid structure, with one peak similar to the $t\bar{t}$ one and a second peak that follows the shape of the Z' distribution.

The observed features can be interpreted by analysing the different production mechanisms of b -hadrons in the physics processes under exam. In $t\bar{t}$ events b -hadrons originate from top quark decays, so the p_T of the associated b -jets is generally limited by the top mass. This is the case for the majority of the b -jets, which populate the first bins in Fig-

ure 4.2 and yield the largest b -tagging efficiency in Figure 4.1. The b -jets with higher p_T must necessarily originate from top quarks with significant boost, where the decay products are collimated and can potentially overlap within the cone of the jets [155]. Indeed, Figures 4.2 and 4.3 show that the fraction of jet p_T carried by the b -hadrons tends to decrease in high p_T bins, implying that the reconstructed jets contain more objects from different sources. The situation is different in Z' events, where the b -hadrons originate directly from the two-body decay of the resonance, so the corresponding b -jets are well isolated and the relation between b -hadron and b -jet p_T is nearly independent of the p_T regime. Finally, in W' events a first b -hadron is produced directly in the decay of the resonance, while a second one originates from the decay of the top quark. As a result, 50% of the jets show the same features of those from the Z' sample, while the others behave similarly to the $t\bar{t}$ ones, yielding the hybrid behaviour observed in the plots.

The larger b -tagging efficiency at high p_T in $t\bar{t}$ events compared to Z' can be explained by the fact that a given bin of b -jet p_T corresponds to different average boosts of the b -hadrons. The performance of the b -tagging algorithms is driven by the p_T of the b -hadron, which influences the average displacement of the secondary vertex (see Figure 3.8) and the associated quantities, such as the impact parameters d_0 and z_0 . The MV2c10 algorithm is optimised for the bulk of $t\bar{t}$ events, where it achieves the highest efficiency, while the performance deteriorates when the kinematical properties of the b -hadrons are significantly altered.

4.2.3 Systematic uncertainties on b -tagging efficiency

After the discussion of the nominal performance of the MV2c10 tagger, it is now possible to analyse the impact of the uncertainties presented in Section 4.1.3. Since the number of systematic variations is large, it is convenient to consider separately the track-related and jet-related ones, so that the individual contributions can be highlighted. In addition, due to the observed discrepancy in the nominal efficiency, it is useful to evaluate the size of the systematic variations separately for $t\bar{t}$ and Z' samples.

Figure 4.4 shows the uncertainty on the b -tagging efficiency as a function of the b -jet p_T

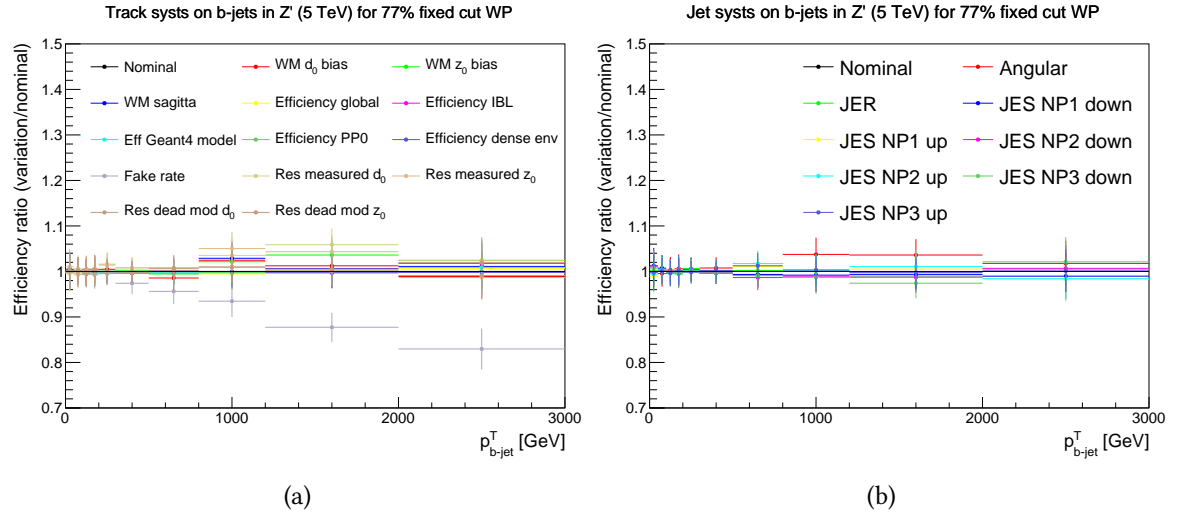


Figure 4.4: Ratio of modified and nominal b -tagging efficiencies as a function of b -jet p_T in a 5 TeV Z' sample for the 77% fixed cut WP, showing the impact of the individual track (a) and jet (b) systematics.

caused by track and jet systematics in a 5 TeV Z' sample, for the 77% fixed cut WP. A remarkable feature of the Z' sample is the large amount of statistics in the boosted p_T regime of the b -jets, which allows to measure the uncertainty with high accuracy up to a 2-3 TeV p_T bin, while c -tagging efficiency and mistag rate cannot be studied due to the lack of c -jets and light jets in the final state. The size of the variations is generally low, with the largest contribution given by the track fake rate, which reduces the tagging efficiency in the highest p_T bins.

Analogous efficiency plots are shown in Figure 4.5 for $t\bar{t}$, where c -tagging efficiency and mis-tag rate can also be shown thanks to the sufficient amount of c -jets and light jets in the sample. Due to the lower available statistics at high p_T , the uncertainties are evaluated only up to a maximum p_T of 2 TeV. The observed uncertainties on the b -tagging efficiency (Figures 4.5a-4.5b) are generally compatible with the results obtained with the Z' sample: the dominant variations originate from track-related effects, while the jet systematics have a negligible impact. The total uncertainties do not exceed $\sim 10\%$ even for the highest p_T bin, and the size of the track fake rate uncertainty is slightly smaller

than the same variation in the Z' sample.

The impact of the uncertainties on c -tagging efficiency and mistag rate from light jets in $t\bar{t}$ events is presented in Figures 4.5c and 4.5f. While the jet uncertainties are again causing minor effects, the track-related systematics produce significant variations of the efficiency in a broad range of jet p_T . In particular, the smearing of the resolution of both impact parameters (d_0 and z_0) causes a relevant increase of the mistag efficiency for both c -jets and light jets. This result is not surprising, since the misidentification of jets is mainly due to mis-measurements of tracking parameters [144].

The total impact of track-related systematic uncertainties on the efficiencies is shown in Figure 4.6 for b , c and light jets in the $t\bar{t}$ sample and for b -jets in the Z' sample. For simplicity, the histograms are obtained by summing in quadrature the contributions from the individual sources of uncertainty. This strategy neglects potential correlations between different systematics and may produce a double counting of similar effects, but it provides a good estimate of the overall size of the tracking uncertainties on the efficiency of the MV2c10 algorithm. The relative uncertainty on the b -tagging efficiency is below 10% for all b -jets up to 1.2 TeV, and remains below 20% even when b -jets with p_T higher than 2 TeV are considered. The size of the variations at high p_T is slightly more significant in Z' compared to $t\bar{t}$, due to the larger impact of the track fake rate uncertainty. The uncertainty on the c -tagging efficiency is around 10% up to jet p_T values of 800 GeV, while the mis-tag uncertainty is stable around 30% and reaches 50% only in the highest- p_T bin. The corresponding plots for jet-related systematics are included in Appendix B.

4.2.4 Final remarks

The performance studies presented in this chapter are used to define a systematic uncertainty on the efficiency scale factors of the MV2c10 algorithm, based on the total tracking uncertainties shown in Figure 4.6. The uncertainty is particularly relevant in boosted regime of the jets, where the data-driven calibration techniques cannot be employed.

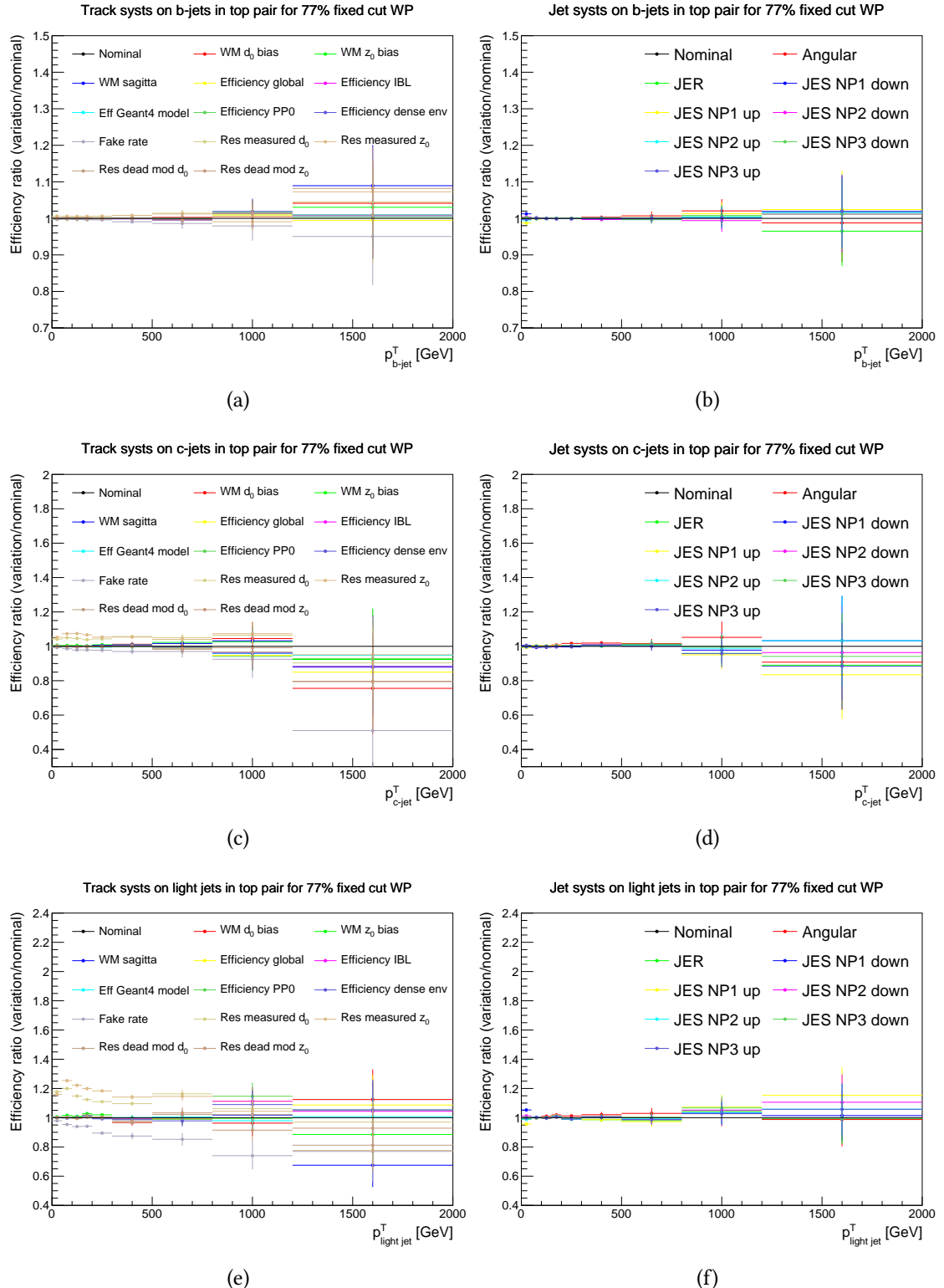


Figure 4.5: Ratio of modified and nominal b -tagging efficiencies as a function of jet p_T in a $t\bar{t}$ sample for the 77% fixed cut WP, showing the impact of the individual track (left) and jet (right) systematics on b (top), c (middle) and light (bottom) jets.

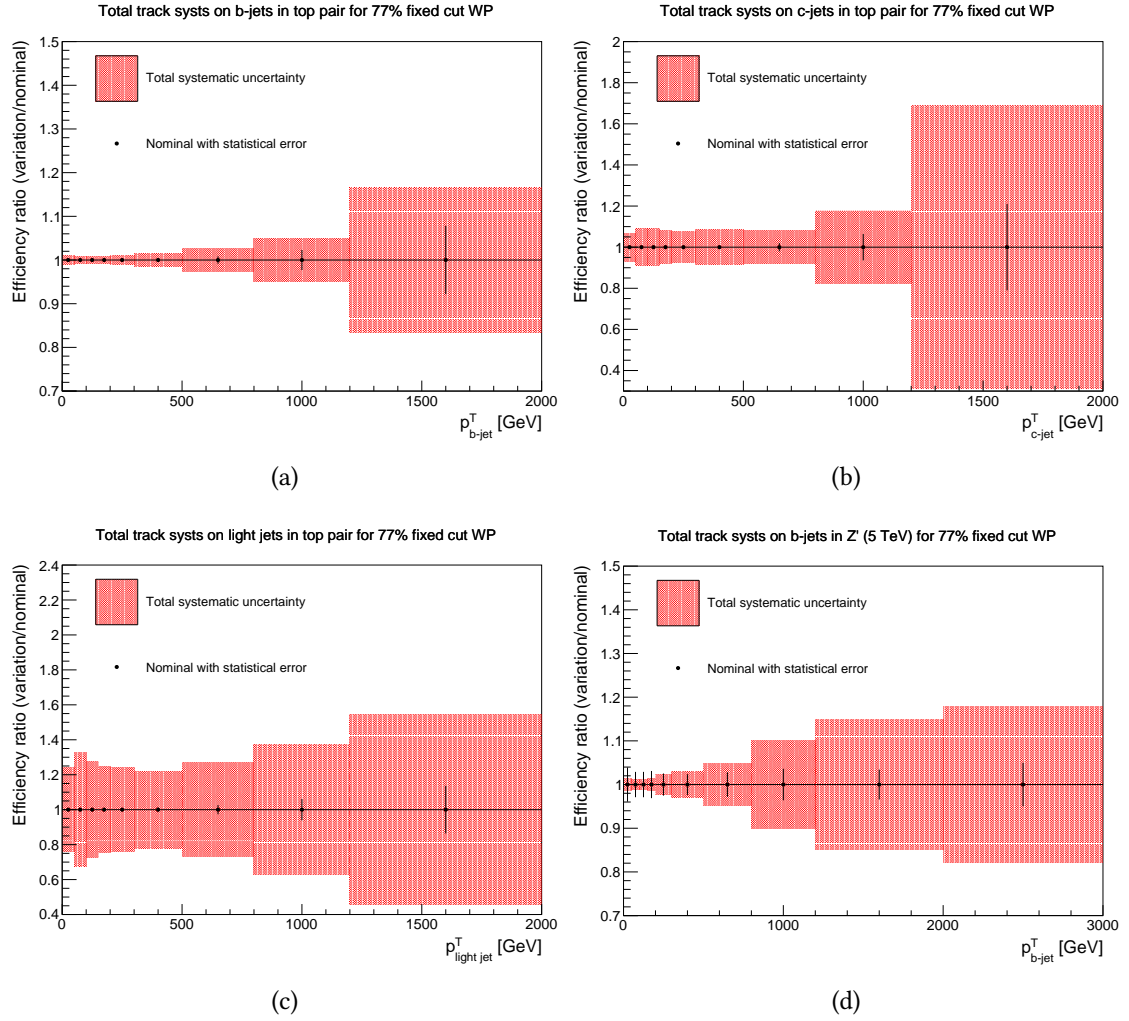


Figure 4.6: Relative uncertainty caused by tracking systematics on the tagging efficiency as a function of jet p_T for b (a), c (b) and light jets (c) in a $t\bar{t}$ sample, and for b -jets in a Z' sample (d), for the 77% fixed cut WP.

In addition, the comparison between the performance in $t\bar{t}$, Z' and W' samples is also showing a significant discrepancy between the b -tagging efficiencies in different physics processes, caused by the different sub-structure of the b -jets. This effect is not related to the modelling of hadronisation and fragmentation in the Monte Carlo samples, and it must be taken into account when applying b -tagging selections on jets with p_T greater than a few hundred GeV.

Finally, the studies in this chapter are based on the 77% fixed cut WP, which is used for all analyses presented in this thesis, but similar results with the fixed efficiency WP are included in Appendix B. The analysis was also repeated for the 60%, 70% and 85% WPs, commonly used within the ATLAS Collaboration, reaching similar conclusions about both nominal performance and systematic uncertainties.

Chapter 5

Third generation SUSY searches in ATLAS

The core topic of this thesis is the search for third generation squarks in the framework of natural pMSSM models (introduced in Section 1.3.3) and models with spontaneous R -parity breaking (Section 1.3.4). While the two types of signals are targeted by independent analyses, the general approach presents several common aspects that are introduced in the present chapter before discussing the individual cases.

Section 5.1 describes the characteristic experimental signature of SUSY particles at the LHC, with emphasis on the case of third generation squarks. The dominant background processes are then introduced in Section 5.2 together with a description of the Monte Carlo samples that are employed for the searches in Chapters 6 and 7. Section 5.3 presents the general workflow of the two analyses, which is common to several more SUSY searches in ATLAS, including a description of the 2015 and 2016 data samples, the online and offline event selection, the definition of signal-enriched regions and the baseline background estimation strategy. Finally, Section 5.4 is dedicated to the statistical tools that are employed for the evaluation and the interpretation of the results of the searches.

5.1 SUSY searches

The superpartners of Standard Model particles are expected to appear in the proton-proton collisions produced by the LHC, yielding characteristic experimental signatures in the ATLAS detector. Since the production mechanisms are regulated by R -parity conserving couplings (with model-dependent exceptions far beyond the scope of this thesis) the analyses are done under the assumption that SUSY particles are pair-produced. This section presents an overview of the typical approach to SUSY searches in ATLAS, highlighting the challenges that they pose and the strategies used to overcome them. The phenomenology of third generation squarks is discussed in detail, in order to provide the context of the analyses in Chapters 6 and 7.

5.1.1 Experimental challenges

The main difficulties faced by SUSY searches in ATLAS are related to the presence of an overwhelming amount of background from Standard Model processes. The production cross section of the most relevant SUSY particles at the LHC [156] is shown in Figure 5.1, to be compared with the background cross sections in Figure 5.2, that are larger by several orders of magnitude. The signal cross sections are obtained by treating squarks and gluinos as decoupled particles, which means that squarks do not contribute to gluino production diagrams and vice versa. Under this assumption, the cross section of squark pair-production is found to be the same for all families, with a twofold degeneracy for each flavour due to the presence of left and right handed components. Gluinos have a relatively large cross-section, while neutralinos and charginos are disfavoured because their production is mediated by electroweak interaction.

The low cross section of SUSY particles implies that dedicated selections must be implemented to remove the majority of the events collected by the detector, identifying those with signal-like properties. A description of the baseline analysis strategy is presented in Section 5.3.

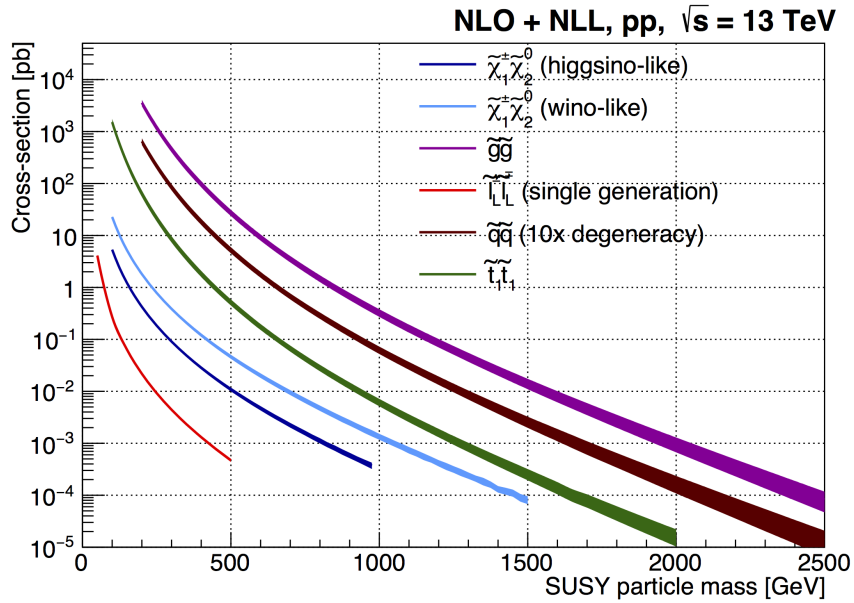


Figure 5.1: Cross sections for pair production of SUSY particles as a function of their mass in proton-proton collisions at $\sqrt{s} = 13$ TeV. The cross sections are computed under the assumption that the different SUSY particles are decoupled.

5.1.2 Benchmark models

The parametrisation of SUSY models can be challenging from a practical point of view, due to the large number of particles and degrees of freedom in the MSSM. A common strategy [157] is to concentrate on specific signal processes extracted from the full models, ignoring any particle that does not contribute to them. For example, an analysis can be designed to target pair-produced squarks decaying into a Standard Model quark and a neutralino, neglecting completely the rest of the SUSY mass spectrum. The signature-based benchmarks, referred to as simplified models, allow to minimise the number of free parameters that define the phenomenological properties of the signal: in the above example, the masses of squarks and neutralinos are sufficient.

Due to their convenience, simplified models have become a standard tool for SUSY searches in ATLAS. Their simplicity is also a benefit for the reinterpretation of the results of the analyses under different theoretical assumptions, which is a powerful way

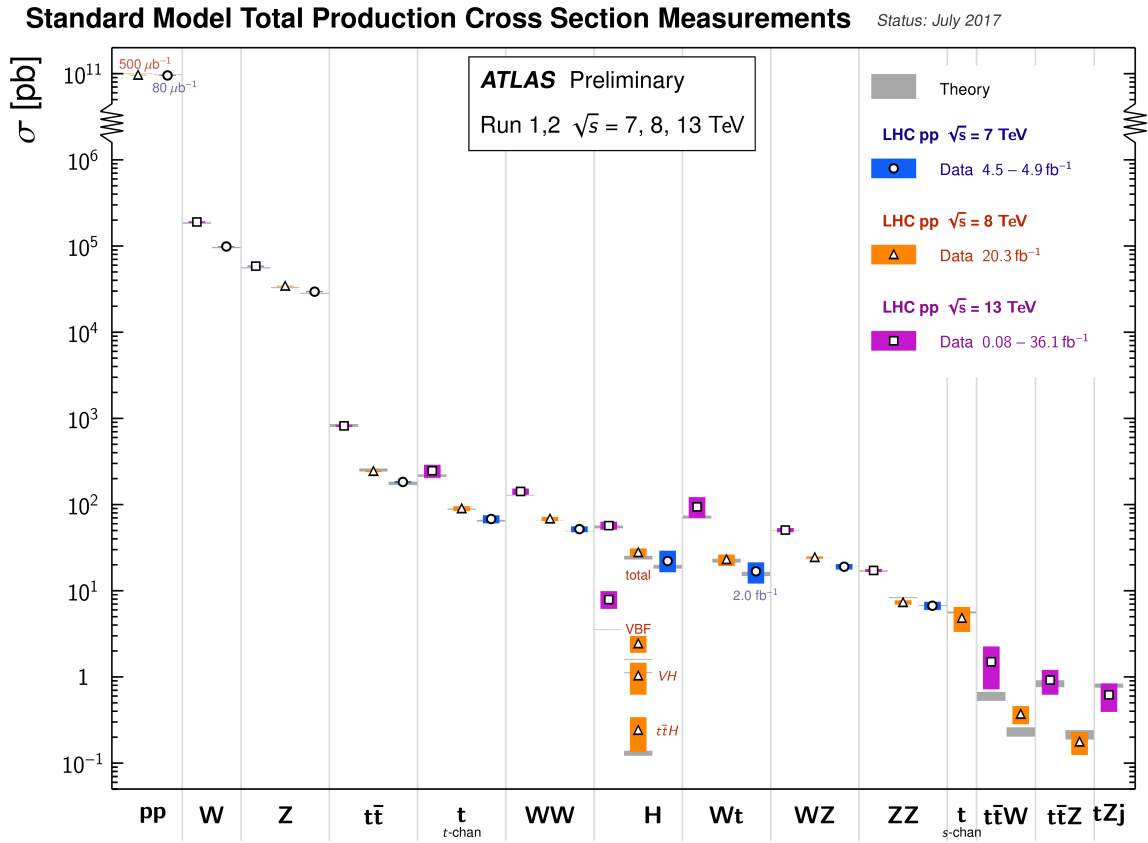


Figure 5.2: Summary of the cross sections of the most relevant Standard Model processes measured by the ATLAS experiment at $\sqrt{s} = 7, 8$ and 13 TeV.

to constrain new models. When following this approach it is important to keep track of the theoretical assumptions behind the specific features of the models, to be able to interpret the results of the searches in broader contexts. The analyses presented in this thesis are entirely based on simplified models of third generation squarks, motivated by the theoretical arguments discussed in Chapter 1.

5.1.3 Phenomenology of third generation squarks

While the cross section of stop and sbottom pair-production with decoupled gluinos depends only on the mass of the sparticles, the experimental signature of the models varies significantly if different decays are considered. Lighter signals are generally easier to target thanks to the larger production rate, but in some situations the kinematic properties

of the final states resemble those of the Standard Model backgrounds, compromising the possibility to obtain an effective separation. For each SUSY model, it is hence important to optimise dedicated selections for different hypotheses on masses and decay modes. In the case of third generation squarks, the experimental signatures are generally similar for stop and sbottom production, so the analyses can often be interpreted in both scenarios. The next pages provide an overview of the phenomenology studied within the ATLAS Collaboration, highlighting the differences between the two cases.

R-parity conserving decays

The ATLAS searches for stop or sbottom pair-production with RPC decays are usually done under the assumption of a neutralino ($\tilde{\chi}_1^0$) LSP [158]. This choice satisfies the requirements of the natural pMSSM spectrum shown in Figure 1.7 and provides a good candidate for dark matter. In the simplest case the squarks decay directly into the LSP plus some extra Standard Model particles, so the signal properties are basically defined by fixing the values of the masses of the two superpartners. More degrees of freedom appear if additional SUSY particles are included in the decay chain, such as heavier neutralinos or charginos.

The signal benchmark samples are typically generated as a grid of simplified models parametrised by the mass of the third generation squark and of one of the SUSY particles from the decay chain. If more than two SUSY particles are involved, dedicated assumptions are made on the masses of the extra ones in order to keep a total of two free parameters. For example, when working in the framework of the natural pMSSM spectrum it is necessary to include an extra light chargino ($\tilde{\chi}_1^+$) and a next-to-lightest neutralino ($\tilde{\chi}_2^0$) in addition to the \tilde{t} (or \tilde{b}) and the $\tilde{\chi}_1^0$. A two-dimensional signal grid can be obtained by making an assumption on the mass splitting between the heavier Higgsinos and the LSP, leaving the values of $m_{\tilde{t}}$ and $m_{\tilde{\chi}_1^0}$ as the only free parameters.

The most relevant decay modes of the \tilde{t} that terminate with the production of a $\tilde{\chi}_1^0$ are shown in Figure 5.3 in the $m_{\tilde{t}}\text{-}m_{\tilde{\chi}_1^0}$ plane. The dominant final states are different depending on which region of the parameter space is considered, yielding a rich and complex

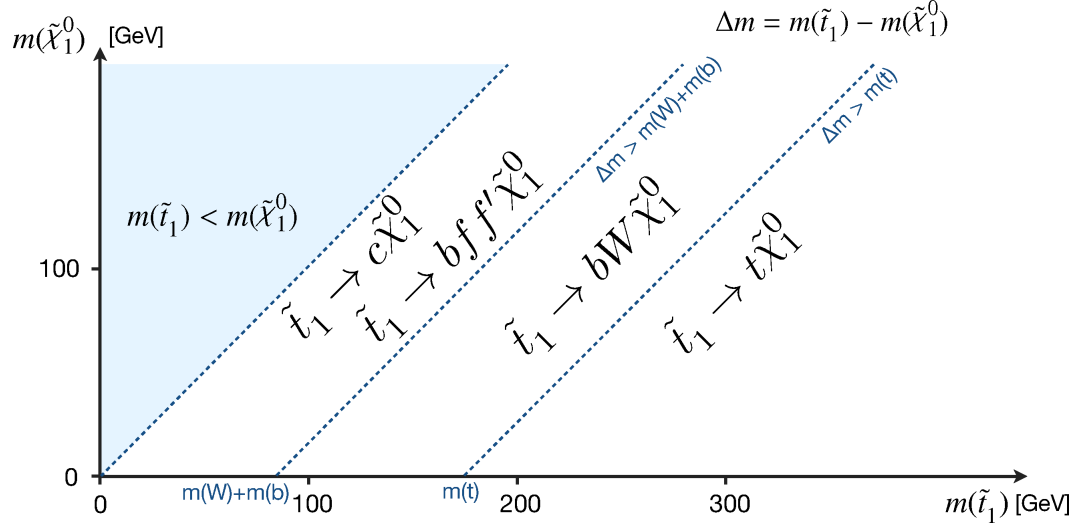


Figure 5.3: Stop decay modes in the $m_{\tilde{t}}-m_{\tilde{\chi}_1^0}$ plane [158].

phenomenology.

A favoured two-body decay of the \tilde{t} , shown Figure 5.4a, is the following:

$$\tilde{t}_1 \rightarrow t\tilde{\chi}_1^0 \quad (5.1)$$

that requires $m_{\tilde{t}_1} > m_t + m_{\tilde{\chi}_1^0}$. In principle an analogous decay into heavier neutralinos can occur, yielding more objects in the final state, but this possibility is neglected in the present discussion. When a two-body decay takes place, the boost of the quarks and LSPs in the final state depends on the mass splitting $\Delta m(\tilde{t}_1, \tilde{\chi}_1^0)$. If the splitting is large the objects are produced with high momentum, while compressed mass spectra yield softer decay products, that often require dedicated analysis techniques. An alternative two-body decay, illustrated in Figure 5.4b, is:

$$\tilde{t}_1 \rightarrow b\tilde{\chi}_1^+ \quad (5.2)$$

where the kinematic constraint is $m_{\tilde{t}_1} > m_b + m_{\tilde{\chi}_1^+}$ and the mass of the $\tilde{\chi}_1^+$ appears as a new free parameter. It should be noted that the decays in Figures 5.4a and 5.4b assume that the \tilde{t} decays exclusively in the channel of interest, $t\tilde{\chi}_1^0$ and $b\tilde{\chi}_1^+$ with 100% respectively. If both decays occur with comparable branching ratios (BRs) it is possible to obtain asymmetric final states as the one shown in Figure 5.4c, interesting to examine

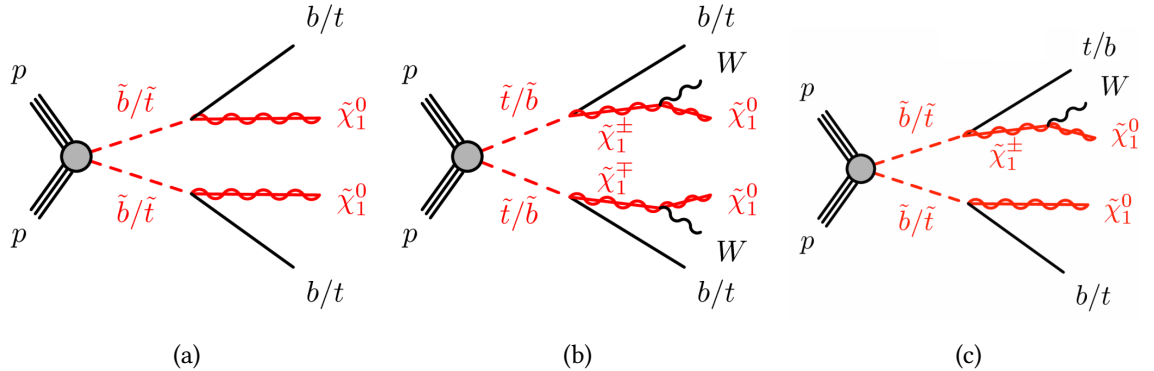


Figure 5.4: Stop quarks decaying directly into a $\tilde{\chi}_1^0$ (a), via a $b\tilde{\chi}_1^+$ (b) or into a mixture of the two final states (c). The figures show how the diagrams changes if \tilde{t} or \tilde{b} pair production is considered.

in addition to the symmetric ones.

Another possible two-body final state [159] can be obtained through the following decay:

$$\tilde{t}_1 \rightarrow c\tilde{\chi}_1^0 \quad (5.3)$$

where no third generation quarks are produced. Since this process implies flavour violation, it is commonly expected to be relevant only when the competitive channels are forbidden by kinematic constraints, as in the compressed region in Figure 5.3.

It should be emphasised that, as Figure 5.4 shows, the Feynman diagrams associated with the above processes can be used to describe both \tilde{t} or \tilde{b} pair-production by inverting the positions of top and bottom quarks in the final states. The replacement has a significant impact on the phenomenological properties of the signals, because top quarks have a more complex experimental signature, so the analyses need to be adapted to the chosen case. A comprehensive search where \tilde{b} pair-production is assumed is presented in Chapter 6.

When two-body decays are kinematically forbidden, the off-shell decays of the \tilde{t} via virtual W bosons or top quarks become relevant, yielding three-body or four-body final

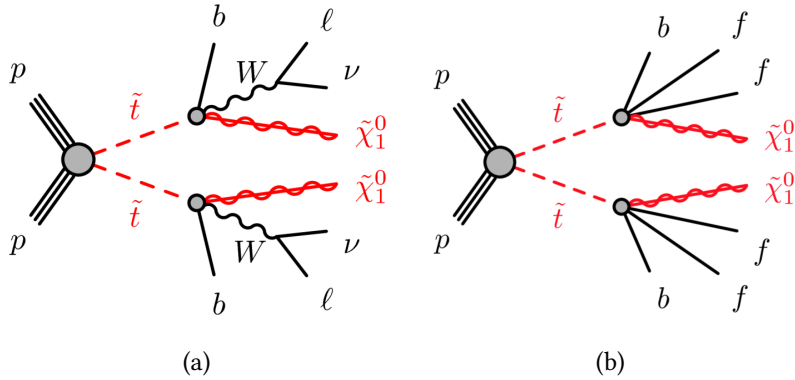


Figure 5.5: Three-body (a) and four-body (b) decays of the stop. For the three-body case, the leptonic decay of W bosons is shown.

states. The decay via a virtual top quark (Figure 5.5a) is:

$$\tilde{t}_1 \rightarrow b W \tilde{\chi}_1^0 \quad (5.4)$$

while the four-body decay where also the W is virtual gives:

$$\tilde{t}_1 \rightarrow b f f' \tilde{\chi}_1^0 \quad (5.5)$$

As discussed in detail in Ref. [159], the four-body decay and the two-body decay into charm quarks (Equation 5.3) are predicted to be relevant in the same region of the $m_{\tilde{t}} - m_{\tilde{\chi}_1^0}$ plane, with a relative branching ratio that depends on the values of the MSSM parameters.

R-parity violating decays

When the \tilde{t} decays via R -parity violating couplings the assumption of a $\tilde{\chi}_1^0$ LSP can be dropped, and direct decays into Standard Model particles become possible. As discussed in Section 1.3.4, models with spontaneously broken $U(1)_{B-L}$ symmetry predict the two-body decay of the \tilde{t} into a bottom quark and a lepton (see Equation 1.35) where the preferred lepton flavour is related to the neutrino mass hierarchy. This signal, shown in Figure 5.6a, yields two b - ℓ pairs with invariant mass peaking at $m_{\tilde{t}_1}$ and is targeted by

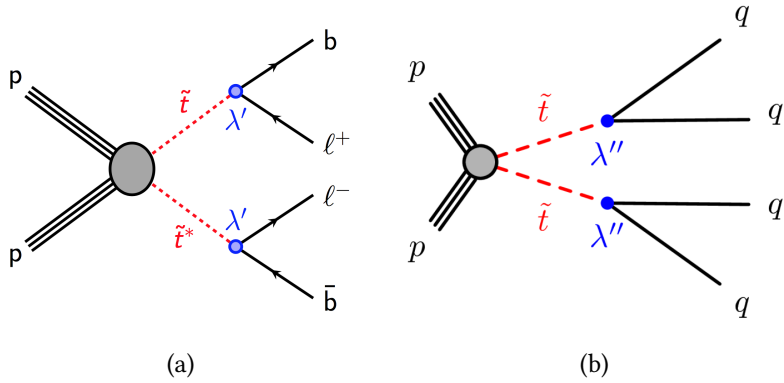


Figure 5.6: RPV decays of the stop into a $b\text{-}\ell$ pair (a) and two quarks (b).

the analysis presented in Chapter 7.

Finally, an alternative RPV coupling predicts the prompt decay of the \tilde{t} into a pair of quarks:

$$\tilde{t}_1 \rightarrow qq' \quad (5.6)$$

The corresponding Feynman diagram is shown in Figure 5.6b, and the analysis is particularly challenging due to the overwhelming multijet background at the LHC.

5.2 Backgrounds and Monte Carlo simulations

As discussed in Section 5.1, the experimental signature of third generation squarks is similar to a variety of Standard Model processes with significantly larger cross sections. The accurate modelling of these backgrounds is hence essential to implement robust physics analyses that are able to target the desired signals. In particular, the definition of Signal Regions (see Section 5.3.5) requires an accurate knowledge of the kinematical properties of both signals and backgrounds, and the final sensitivity of the searches depends on the ability to estimate the leftover backgrounds with high accuracy. This section is dedicated to a discussion of the properties of the most relevant Standard Model backgrounds in ATLAS, together with a description of the Monte Carlo Samples that are used to model them in the analyses.

5.2.1 Background processes

The main sources of Standard Model background, whose relative importance depends on the specific selections of each analysis, are described in detail the list below, which includes information about their properties obtained from the Particle Data Group [160]:

Z + jets The associated production of Z bosons and jets is a relevant source of background in 0-lepton plus E_T^{miss} or 2-lepton final states, due to the $Z \rightarrow \nu\nu$ decay (with BR $\sim 20\%$) and the $Z \rightarrow \ell\ell$ decay ($\ell = e, \mu, \tau$, with total BR $\sim 10\%$). The $Z \rightarrow qq$ decay, which occurs with the largest BR ($\sim 70\%$), generates a pair of quarks with relatively low boost, yielding a fully hadronic final state which is covered by the dominant multi-jet background and hence is not relevant for third generation SUSY searches. A Feynman diagram corresponding to the production of a Z boson and a bottom quark pair is shown in Figure 5.7a.

W + jets Similarly, the production of W bosons plus jets yields a relevant background in many ATLAS analyses, especially when final states with 1 lepton are considered, due to the $W \rightarrow \ell\nu$ decay ($\ell = e, \mu, \tau$) which happens with a total BR of $\sim 32\%$. The dominant $W \rightarrow qq'$ decay yields a multi-jet final state which is again irrelevant for the analyses in this thesis. Figure 5.7b shows a Feynman diagram corresponding to the associated production of a W boson and a bottom quark pair, closely resembling the Z boson one.

Top pairs A major background process at the LHC is the pair production of top quarks, already introduced for the b -tagging performance studies in Section 4.1.2. The dominant $t \rightarrow Wb$ decay, with $\sim 99.8\%$ BR, yields two b -jets and two oppositely charged W bosons that further decay as described above, yielding 0-lepton, 1-lepton and 2-lepton final states with 45.7%, 43.8% and 10.5% BRs respectively. The Feynman diagram corresponding to the semi-leptonic decay scenario is shown in Figure 5.7c.

Single top While top quarks are mainly produced in pairs, the single production is also

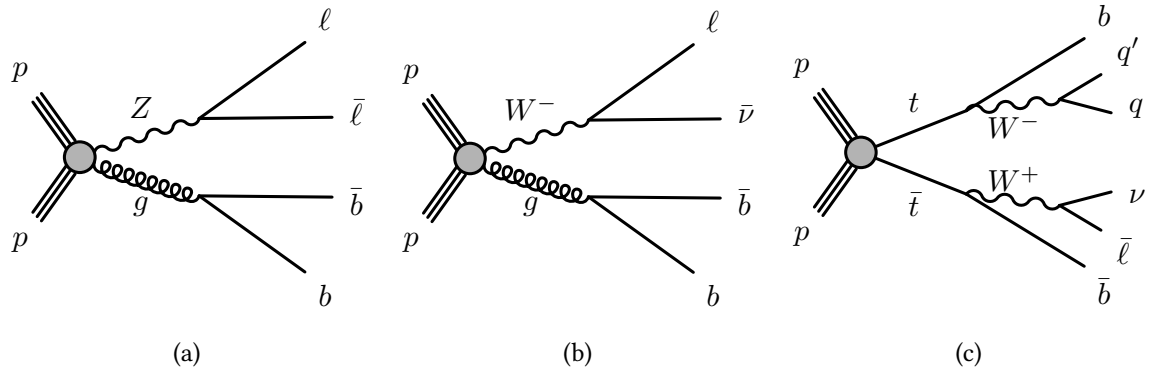


Figure 5.7: Feynman diagrams for the associated production of a pair of bottom quarks and a Z (a) or W (b) boson, and for the pair production of top quarks (c) at the LHC.

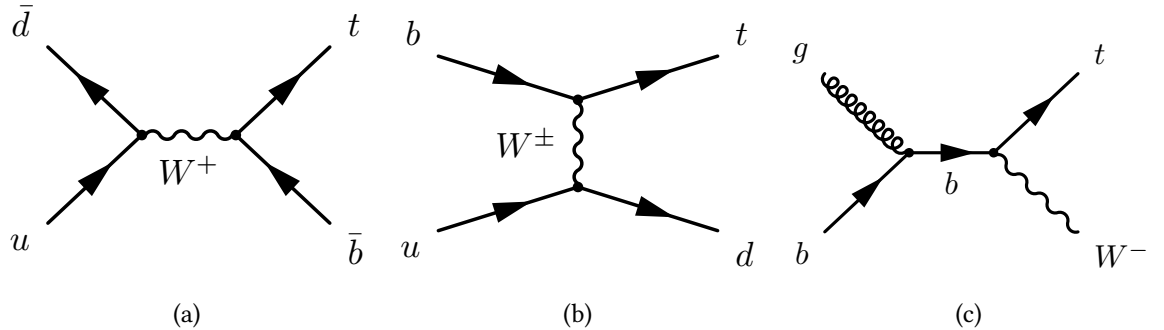


Figure 5.8: Feynman diagrams for the production of a single top quark at the LHC, in the s -channel (a), t -channel (b) and Wt channel (c).

possible at the LHC via one of the three diagrams shown in figure 5.8, referred to as s -channel, t -channel and Wt channel. The latter case is generally the most relevant for third generation SUSY analyses, because it yields a lepton, two b -jets¹ and a significant amount of E_T^{miss} .

Top pair plus X The pair production of top quarks can also happen in association with an extra boson in the final state, that can be a vector boson (γ , W or Z) or a Higgs

¹The first b -jet originates from the decay of the top quark, while the second appears as a result of the extraction of a $b\bar{b}$ pair from the sea.

boson. Despite the lower cross section with respect to the processes considered so far, $t\bar{t}+X$ production can be a relevant background for third generation SUSY models, especially in the case of W and Z bosons for which the cross section is relatively larger.

Di-bosons Another set of processes with low cross section but signal-like properties is the di-boson production, where pairs of vector bosons can appear in different combinations and the most relevant cases are WW , WZ or ZZ . Final states with variable lepton and jet multiplicities are obtained when different decays of the bosons are considered.

Multi-jet The majority of proton collisions at the LHC yield fully hadronic final states, which result in multi-jet events with no prompt leptons or invisible objects. These events may assume signal-like properties as a result of the mis-reconstruction of isolated leptons, or due to large measured values of the E_T^{miss} from detector resolution effects. While both contingencies are unlikely, their probability is enhanced by the large total cross section of the process, so it is important to estimate the impact of this background in the relevant analysis channels.

5.2.2 Monte Carlo samples

Signal and background processes are simulated through the procedure described in Section 3.1, and Monte Carlo samples are obtained for all of them with the exception of multi-jet production, which is estimated in the analyses using dedicated data-driven techniques.

SUSY signal samples are generated using MadGraph [106] v2.2.3 at leading order (LO) and interfaced to Pythia v8.186 [104] for the modelling of the parton showering (PS), hadronisation and underlying event, using the A14 tune [102]. The matrix element (ME) is computed at tree level including the emission of up to two additional partons. The ME-PS matching is done following the CKKW-L prescription [161], with matching scale set to a quarter of the squark mass, and the NNPDF23LO [89] PDF set is used.

The associated production of W or Z bosons and jets is simulated with the Sherpa v2.2.1 generator [108], including jets from the hadronisation of b and c quarks. The matrix elements are calculated for up to two additional partons at NLO and four partons at LO using Comix [162] and OpenLoops [163], and the matching is performed using the Sherpa PS generator [109] with the ME+PS@NLO prescription [164]. The simulations use the NNPDF30NNLO PDF set [89] and a dedicated PS tune developed by the Sherpa authors. In order to increase the available statistics in the most relevant regions of phase space, the simulations are split in sub-samples where specific flavours of the jets (b , c and light) are selected. A further slicing is performed using as filtering variable the maximum between H_T ² and the p_T of the boson, so that the production of boosted particles is simulated with higher precision. The W/Z plus jets events are normalised to their NNLO cross sections [165].

Single top and $t\bar{t}$ are simulated at next-to-leading order (NLO) with the Powheg event generator [107], using v1 for the t -channel single top process and v2 for $t\bar{t}$ and the remaining single top channels. In all these samples the mass of the top quark is set to 172.5 GeV, and the matrix element computation employs the CT10 PDF set [86]. The parton shower (PS), fragmentation, and underlying event simulation are performed with Pythia v6.428 [103], using the CTEQ6L1 PDF set [87] and the P2012 (Perugia) tune [101]. Both $t\bar{t}$ and single top events are required to contain at least one leptonically decaying W boson, while fully hadronic events are removed from the samples because they do not represent a relevant source of background for the analyses. In addition, a dedicated slicing is implemented using E_T^{miss} and H_T as filtering variables, in order to populate the tails of the associated distributions with sufficient MC statistics. The $t\bar{t}$ samples are normalised to their next-to-NLO (NNLO) cross section [166], while the NNLO cross-sections reported in Refs. [167–169] are used for the s , t and Wt channels of single top.

The production of top quark pairs plus electroweak vector bosons (W, Z) or Higgs bosons is simulated at NLO using MG5_aMC@NLO v2.2.3 and Pythia v8.212. Diboson processes are simulated using the Sherpa, similarly to the case of the W/Z plus jets sam-

²The H_T variable is defined as the scalar sum of the p_T of all jets in the event.

Process	ME	PS	UE tune	PDF	Cross section
Signal	MadGraph 2.2.3	Pythia v8.186	A14	NNPDF2.3	NLO+NLL
$t\bar{t}$	Powheg v2	Pythia v6.428	P2012	CT10	NNLO+NNLL
Single top (s, Wt)	Powheg v2	Pythia v6.428	P2012	CT10	NNLO+NNLL
Single top (t)	Powheg v1	Pythia v6.428	P2012	CT10	NNLO+NNLL
$W/Z+\text{jets}$	Sherpa 2.2.1	Sherpa 2.2.1	Default	NNPDF3.0	NNLO
Diboson	Sherpa 2.2.1	Sherpa 2.2.1	Default	NNPDF3.0	NLO
$t\bar{t} + W/Z$	MG5_aMC@NLO 2.2.3	Pythia v8.212	A14	NNPDF2.3	NLO

Table 5.1: Details of the MC simulations used for each physics process.

ples, and the matrix element is computed up to one (ZZ) or zero (WW, WZ) additional partons at NLO and up to three additional partons at LO.

For all samples described above, with the exception of those generated with Sherpa, the EvtGen v1.2.0 program [110] is employed to simulate the decays of b and c hadrons. Pileup is simulated by overlaying additional pp collisions to the hard scattering events, using Pythia v8.186 as generator with the MSTW2008LO [90] PDF set. The interaction of the particles in the final state with the detector is simulated with Geant4 as described in Section 3.1.3, using a full simulation for the background processes and an AF2 simulation for the signal samples. A summary of the details of the MC simulations is provided in Table 5.1.

Additional samples are generated to estimate the theoretical uncertainties associated with the configuration of the MC simulations. These include variations of the renormalisation, factorisation or CKKW matching scales, different PDF sets or hadronisation models, as described in more detail in Section 5.3.4.

5.3 Analysis strategy

The analyses in this thesis are based on a cut and count strategy, where events are selected according to the experimental signature of the targeted signals and a dedicated set of discriminating variables is employed to define signal-enriched regions with reduced

levels of Standard Model background. The relevant observables of the analyses are the number of events passing each selection, and their values are predicted for both signal and background processes using MC samples, data-driven techniques or combinations of the two.

This section introduces the general strategy of the analyses in Chapters 6 and 7, together with a description of the common technical aspects. These include the data sample, the trigger and event cleaning selections, the definition of physics objects and experimental quantities in the events with the related performance corrections in MC, and the dominant sources of systematic uncertainties. In addition, the standard strategies for the definition of SRs and the estimation of the leftover backgrounds is outlined.

5.3.1 Data sample and event selection

The analyses presented in this thesis are based on proton-proton collision data at $\sqrt{s} = 13$ TeV collected by the ATLAS detector during 2015 and 2016. The dataset corresponds to an integrated luminosity of 36.1 fb^{-1} , computed after requiring the full operation of all detector sub-systems during the data taking periods. The measured value of the integrated luminosity carries an uncertainty of 3.2%, derived through a procedure similar to the one described in Ref. [170] using x - y beam separation scans performed in August 2015 and May 2016. The average pileup parameter μ is 13.7 in 2015 and 24.9 in 2016, where a higher instantaneous luminosity was reached (see Section 2.1.4).

Due to the different operating conditions of the experiment in 2015 and 2016, a variety of selections are applied differently in the various periods of the data taking, including trigger requirements and calibration parameters. Since the same Monte Carlo samples are used for all periods, the simulated events are assigned a random number that identifies a given ATLAS run, allowing to associate them with specific periods of operation so that their parameters can be modified consistently with what is done in data.

Online triggers

As discussed in Sections 2.3.6 and 3.2.1, events are recorded by the ATLAS detector if they satisfy the requirements of pre-defined trigger chains based on the presence of specific objects or features in the events. The analyses in Chapters 6 and 7 employ E_T^{miss} triggers in 0-lepton events, single electron or muon triggers in channels with one or more leptons, and single photon triggers when the presence of a photon is required. The detail of the trigger chains that are used is given below:

E_T^{miss} triggers The online requirement on the E_T^{miss} is applied using different energy thresholds depending on the period of data taking. In 2015 data, events are selected by reconstructing the E_T^{miss} from an input jet collection and requiring that its measured value exceeds 70 GeV. During the 2016 operation, a similar algorithm is employed but the energy threshold is progressively increased to 90, 100 and 110 GeV due to the higher instantaneous luminosity, that has a direct impact on the trigger rate. As already seen in Figure 3.4b, these triggers reach their efficiency plateau above offline E_T^{miss} values of approximately 200 GeV.

Single electron triggers In both 2015 and 2016 data a logic OR of three different chains is used to select electron events at trigger level. The first chain includes an isolation requirement, which allows to keep a low energy threshold of 24 GeV in 2015 and 26 GeV in 2016, where tighter identification and isolation selections are also applied. In the second chain the isolation requirement is dropped to reduce efficiency losses at high E_T , and the energy threshold is raised to 60 GeV (constant for the full dataset). Finally, the third chain has looser identification requirements and a higher energy threshold of 120 GeV in 2015 and 140 GeV in 2016. The efficiency plateau is reached by selecting offline electrons with $p_T > 27$ GeV.

Single muon triggers Similarly, events with muons are selected with an OR of two chains, where the first has a lower energy threshold and an isolation requirement. The first chain has an energy threshold of 20 GeV in 2015 and 26 GeV in 2016, where a tighter isolation selection is also included, while the second chain has a

threshold of 50 GeV in the whole dataset. The trigger is fully efficient for offline muon selections with $p_T > 27$ GeV.

Single photon triggers Events with photons are selected using a dedicated chain with energy threshold of 120 GeV in 2015 and 140 GeV 2016. An offline selection of photons with $p_T > 145$ GeV is applied to ensure that the trigger is fully efficient.

Event cleaning

A set of event-level cleaning selections are applied in both data and Monte Carlo samples to remove events where pathological behaviour is observed. A first essential requirement is the presence of at least one primary vertex in the events, with a minimum of two associated tracks with $p_T > 400$ MeV. In addition, data events in which the electromagnetic or hadronic calorimeters are flagged to be in error state are removed from the analysis, and a similar veto is applied in case of single event upsets in the SCT.

Further cleaning selections are applied if poorly reconstructed jets or muons are identified through standard ATLAS criteria. Events with bad jets (as defined in Section 3.2.5) passing the overlap removal (OR) selections (see Section 5.3.2) are removed from the analysis. In addition, a similar veto is applied if baseline muon candidates with relative uncertainty on q/p larger than 20% are found before the OR, or if a muon with cosmic-like properties survives the OR.

5.3.2 Object definition

The definition of physics objects for offline analysis is based on the reconstruction algorithms described in Section 3.2, that are standard tools within the ATLAS Collaboration. While minor differences are present between different searches, including those in Chapters 6 and 7, it is convenient to present the object definition in the present paragraph, highlighting the specificities of each analysis when necessary.

A common approach followed by many SUSY searches is to define two categories of reconstructed objects in the events, referred to as baseline and signal objects. The former

type is identified by a minimal set of conditions applied to the outputs of the reconstruction algorithms, to obtain a large sample of candidates for each physics object, while the latter is selected by applying tighter requirements on the baseline object collections in order to reduce the background contamination.

The baseline collections are used as inputs of an overlap removal (OR) procedure, which is introduced to solve potential ambiguities caused by the presence of close-by objects in the detector, or single objects reconstructed in different ways. This may occur, for example, if a lepton is produced within the cone of a b -jet, or if an isolated electron is identified also by the jet reconstruction algorithm. The OR proceeds through the following sequence:

- The overlap between electrons and jets within $\Delta R < 0.2$ is solved by removing the jets, unless they are b -tagged, in which case the electrons are removed because they are likely to originate from a b -hadron decay.
- Leptons within $\Delta R < 0.4$ from a jet are removed, except if the jets have less than 3 tracks and are overlapping with muons, in which case they are removed instead.
- If photons are included in the OR procedure, they are removed when they are within $\Delta R < 0.4$ from electrons or muons, while jets within $\Delta R < 0.4$ from a photon are removed.

In the analyses in Chapters 6 and 7 the OR is performed in the simple version with no photons, with the exception of the data driven estimate of Z plus jets events discussed in Section 6.0.3, where photon events are used and the OR is modified accordingly.

The detailed definition of baseline and signal objects used for the two analyses is provided below:

Electrons The baseline electron collection is defined by requiring $p_T > 10$ GeV, $|\eta| < 2.47$ and loose identification [117, 119, 120]. Signal electrons are further required to pass the OR and satisfy additional impact parameter (IP) cuts ($d_0/\sigma_{d_0} < 5$, $z_0 \sin \theta < 0.5$), tight identification and loose isolation. The p_T threshold for signal

electrons depends on the analysis: it is 20 GeV³ for the search in Chapter 6 and 40 GeV for the one in chapter 7.

Muons Baseline muons are reconstructed using the combined reconstruction chain (see Section 3.2.4), and are required to pass a medium track quality requirements [123] and to satisfy $p_T > 10$ GeV $|\eta| < 2.5$. Signal muons are then selected after the OR with $p_T > 20$ GeV⁴, after applying IP cuts ($d_0/\sigma_{d_0} < 3$, $z_0 \sin \theta < 0.5$) and loose isolation selections. Finally, cosmic muons are defined through impact parameter selections ($|z_0| > 1$ mm or $|d_0| > 0.2$ mm) and are used for event cleaning purposes.

Photons Reconstructed photons are not used in the main event selections of the two analyses in this thesis, but they are employed for an alternative estimate of the $Z \rightarrow \nu\nu$ background in the \tilde{b} analysis (Chapter 6). Baseline photons are selected with $p_T > 10$ GeV and $|\eta| < 2.37$ (whilst being outside the $1.37 < |\eta| < 1.52$ range), and must satisfy the tight photon shower shape and electron rejection requirements [122]. Signal photons are further required to have $p_T > 145$ GeV and to be isolated.

Jets Hadronic jets are reconstructed using the anti- k_T algorithm seeded by topological clusters, with cone size parameter $R = 0.4$. Baseline jets are selected with $p_T > 20$ GeV and $|\eta| < 4.8$, while signal jets are required to pass the OR, have $|\eta| < 2.8$ and satisfy JVT requirements to suppress pileup (see Section 3.2.5). The signal jet p_T threshold is 20 or 35 GeV in the analysis in Chapter 6 (depending on the channel) and 60 GeV in the analysis in Chapter 7.

b -jets The identification of b -jets is based on the MV2c10 algorithm and uses the 77% fixed cut WP as described in Chapter 4. The same p_T thresholds of standard jets

³In events selected with a single electron trigger, the offline electron with highest p_T is required to have $p_T > 27$ GeV to reach the efficiency plateau.

⁴Similarly to electrons, also signal muons are required to satisfy $p_T > 27$ GeV in events triggered by single muon chains.

are used, while the pseudorapidity range is reduced to $|\eta| < 2.5$.

Missing transverse momentum The E_T^{miss} is reconstructed through the procedure described in Section 3.2.7, using as inputs the baseline objects described above, including the photon term. Hadronically decaying τ leptons are not explicitly reconstructed, so they enter the computation with the standard jet calibration.

5.3.3 Monte Carlo corrections

A dedicated set of Monte Carlo weights are applied to the simulations in order to match the measured values of specific performance parameters in data. These include online and offline scale factors (SFs), already introduced in Chapter 3, and ad-hoc reweighting procedures used to ensure that given quantities (such as the pileup parameter μ) are equally distributed in data and MC samples. The following list describes the MC weights used for the analyses in this thesis:

***b*-tagging SFs** In order to calibrate the performance of the MV2c10 algorithm, as discussed in Chapter 4, efficiency scale factors are defined separately for real b , c and light jets:

$$\text{SF}_i = \frac{\epsilon_i^{\text{data}}}{\epsilon_i^{\text{MC}}}, \quad i = b, c, l \quad (5.7)$$

and the corresponding inefficiency scale factors for non b -tagged jets are also defined:

$$\text{SF}_i = \frac{1 - \epsilon_i^{\text{data}}}{1 - \epsilon_i^{\text{MC}}}, \quad i = b, c, l. \quad (5.8)$$

The total event-level weights are obtained as the product of the above SFs for all jets to which the b -tagging decision is applied.

JVT SFs Additional SFs are used to calibrate the performance of JVT in signal jets, based on the same definition of the b -tagging SFs described above.

Lepton offline SFs Efficiency SFs are also obtained for offline electrons and muons in the events, as anticipated in Sections 3.2.3 and 3.2.4. Electron SFs are com-

puted separately for the reconstruction, identification and isolation steps, while for muons the reconstruction and isolation SFs are employed.

Lepton trigger SFs The performance of the lepton triggers is calibrated using dedicated SFs, that are obtained for both single electron and single muon chains. In events where at least one signal lepton is present, the total trigger efficiency is computed as the probability that at least one of them has fired the corresponding trigger:

$$\epsilon_{\text{trig}} = 1 - \prod_i (1 - \epsilon_i) \quad (5.9)$$

where ϵ_i is the trigger efficiency corresponding to the lepton i . The trigger efficiency SF for each event is hence obtained as:

$$\text{SF}_{\text{trig}} = \frac{\epsilon_{\text{trig}}^{\text{data}}}{\epsilon_{\text{trig}}^{\text{MC}}} = \frac{1 - \prod_i (1 - \epsilon_i^{\text{data}})}{1 - \prod_i (1 - \epsilon_i^{\text{MC}})} \quad (5.10)$$

where only trigger-matched leptons are considered.

Pileup weight Finally, an event-level weight is applied to the MC samples to correct the distribution of the pileup parameter μ and match it to the one observed in the 2015+2016 dataset. The impact of the reweighting procedure is expected to be negligible if the selections of the analysis are not sensitive to pileup.

5.3.4 Systematic uncertainties

In addition to the object definition described in the previous paragraph, it is useful to present an overview of the sources of systematic uncertainty that are relevant for both analyses in this thesis, as well as for several other searches in ATLAS. The list of experimental uncertainties is only partially overlapping with the one presented in Section 4.1.3 for the b-tagging performance studies, where tracking and jet related effects are included. In particular, the impact of tracking uncertainties is not evaluated explicitly in the physics analyses, while a variety of higher-level systematics associated with reconstructed objects or quantities in the events are instead considered. In addition to the experimental effects, the modelling of signal and background processes introduces more

sources of systematics, referred to as theory uncertainties, that are particularly relevant for the majority of SUSY searches.

Similarly to what done in Chapter 4, the systematic uncertainties are implemented by modifying the MC samples according to the expected variations of the relevant quantities. The full list of systematics is presented in the next paragraph, describing separately the experimental and theoretical contributions.

Experimental systematics

The following experimental uncertainties are considered for the analyses in Chapters 6 and 7:

JES and JER The uncertainties on the Jet Energy Scale (JES) and Resolution (JER), already introduced in Section 4.1.3, are implemented with the same procedure in the physics analyses. The uncertainty on the JES is evaluated using a reduced number of variations with respect to the full set, as detailed in Ref. [153], while for the JER the variation of a single parameter is sufficient [154].

JVT The p_T -dependent Jet Vertex Tagger (JVT) scale factors are modified within the uncertainties, obtained from dedicated measurements in $Z \rightarrow \mu\mu$ events [134].

***b*-tagging** The uncertainties on the performance of the MV2c10 algorithm are implemented by modifying the nominal values of the efficiency SFs, based on the result of data-driven calibration measurements and on the MC studies described in Chapter 4. The variations are applied separately to b -jets, c -jets and light jets, with flavour determined from the truth information in the MC samples. The following four independent contributions are evaluated:

- b -tagging efficiency uncertainty measured in $t\bar{t}$ events [142].
- c -tagging efficiency uncertainty from leptonic W events [143].
- Mis-tag rate uncertainty from a negative-tag method [144].

- Uncertainty on the tagging efficiency of high- p_T jets based on the studies in Chapter 4, referred to as extrapolation uncertainty.

Lepton and photon reconstruction The uncertainties on the calibration of the energy or momentum of leptons (electrons and muons) and photons, as well as on their energy or momentum resolutions, are implemented by varying the four-vectors within the measured variations [123, 171].

Lepton and photon efficiency The efficiency scale factors (SFs) associated with the reconstruction and calibration of leptons and photons are also modified within their expected uncertainties, based on the results of the corresponding performance studies [118, 123, 171].

Trigger efficiency Similarly, the trigger efficiency SFs are also carrying experimental uncertainties, that are implemented using the results of the dedicated measurements [75].

Missing transverse momentum The above systematic uncertainties on the physics objects are propagated to the E_T^{miss} , which is rebuilt using the modified input four-vectors. In addition, further variations are introduced to take into account the uncertainty on the track-based soft term described in Section 3.2.7.

Pileup The uncertainty on the pileup weights is implemented by applying their modified values to the MC samples, and evaluating the impact on the predicted rates.

Luminosity The luminosity of the 2015+2016 dataset carries a 3.2% uncertainty, which is also taken into account in the analyses.

Theory systematics

The uncertainties on the modelling of signal and backgrounds are taken into account by adopting dedicated strategies for each process:

W/Z plus jets The uncertainties on W and Z plus jets are estimated by varying the Sherpa parameters related to the factorisation, renormalisation, resummation and CKKW matching scales, combining the individual variations into a total theoretical uncertainty either by summing them in quadrature (as in Chapter 6) or by taking their envelope (as in Chapter 7). In addition, an extra 40% uncertainty is assigned to the heavy flavour jet content in the W plus jets background by varying independently the normalisation of event samples with c -jets or b -jets, based on the results in Ref. [172].

Top production The theory systematics on the $t\bar{t}$ and single top (Wt) backgrounds are evaluated as the difference between the predictions of the nominal MC samples described in Section 5.2.2 and those of alternative samples with different generators or parameter settings. The uncertainties on the amount of extra radiation emitted by the initial and final state of the scattering process, on the PS tune and (for $t\bar{t}$ only) on the choice of the h_{damp} parameter in Powheg are estimated by varying the settings of the nominal Powheg+Pythia generator. In parallel, the hadronisation and PS uncertainties are obtained from samples generated using PowhegBox v2 and showered by Herwig v2.7.1 [173] with the UEEE5 underlying event tune [174], while the uncertainty on the event generator is estimated by comparing the above Powheg+Herwig sample with an alternative one that uses MadGraph interfaced with Herwig. Finally, an extra source of uncertainty comes from the combined modelling of the $t\bar{t}$ and Wt processes, that are sharing the same final states and are hence subject to quantum mechanical interference effects. This is estimated using dedicated LO samples of $t\bar{t}$, Wt and inclusive $WWbb$ production generated with MadGraph, by comparing the sum of $t\bar{t}$ and Wt with the $WWbb$ predictions.

Dibosons and top pair plus W/Z The uncertainties on diboson and $t\bar{t} + W/Z$ backgrounds are estimated by modifying event generator parameters related to the factorization, renormalization, resummation, and CKKW matching scales, similarly to what done for the W/Z samples. Additional uncertainties on the cross

sections are also considered, measuring around 6% for dibosons [175] and 13% for $t\bar{t} + W/Z$ [106].

Signals The theory systematics on the signal samples are calculated for each SUSY model. The resulting variations are dominated by the uncertainties on the choice of the PDF set and on the renormalisation and factorisation scales [156].

Monte Carlo statistics Due to the finite size of the Monte Carlo samples, the rates of the physics processes are predicted with finite accuracy. The impact of the uncertainty on MC statistics is particularly important when extreme regions of phase space are selected, as it often happens in SUSY analyses, and is relevant both for the nominal samples and for the samples that are used to estimate the theory systematics.

5.3.5 Signal Regions

A crucial step of the cut and count analyses is the optimisation of Signal Regions (SRs) which aim at enhancing the signal yield with respect to the dominant background sources. As a preliminary step, a basic selection of candidate events is performed by applying trigger and event cleaning cuts as described in Section 5.3.1, and by requiring the presence of a relevant set of physics objects based on the experimental signature of the targeted SUSY model. For example, in order to isolate the signal in Figure 5.6a (which is the target of the analysis in Chapter 7) it is reasonable to select events that pass a lepton trigger requirement and have a minimum of two jets and two isolated leptons.

Once the events with signal-like shape are identified, additional selections are applied to suppress the leftover background whilst retaining the largest possible fraction of signal. This is done using dedicated sets of discriminating variables with different distributions in signal and background, that are strongly analysis-dependent and are hence not discussed in the present chapter. In general, the optimisation of SR selections is done by

maximising a given figure of merit, such as the significance S :

$$S = \frac{N_{\text{sig}}}{\sqrt{N_{\text{bkg}} + (\sigma_{\text{bkg}} N_{\text{bkg}} + 1)^2}} \quad (5.11)$$

where N_{sig} and N_{bkg} are the signal and background yields, σ_{bkg} is an assumption on the relative systematic uncertainty on the background, and the expression in brackets is incremented by 1 to prevent S from diverging in the limit of low background. The purpose of the above formula is to maximise the ratio between the signal yield and the total uncertainty on the background, defined as the sum in quadrature of the Poisson error $\sqrt{N_{\text{bkg}}}$ and the systematic uncertainty σ_{bkg} . Equation 5.11 is an approximate expression of a discovery significance computed from a test statistic function, as further explained in Section 5.4. The RooStats package [176] of ROOT [177] provides various possible implementations of the significance, which can be used as a figure of merit to optimise the SR selections.

5.3.6 Background estimation

In order to determine the background yields in the SRs without relying exclusively on MC simulations, a semi data-driven method based on the definition of Control Regions (CRs) is implemented in several SUSY analyses, including those presented in this thesis. The CRs are defined as orthogonal selections to the SRs, such that their event yield is dominated by a specific background process and the signal is instead strongly suppressed. A normalisation scale factor for each relevant background is derived by rescaling the expected MC yield to the observed number of data events in the corresponding CR, and the rate prediction in the SR is rescaled accordingly. In a simplified case with one SR and one CR with 100% background purity, the expected background yield in the SR is given by:

$$N_{\text{SR}}^{\text{exp}} = \mu_{\text{MC}} \cdot N_{\text{SR}}^{\text{MC}}, \quad \mu \equiv \frac{N_{\text{CR}}^{\text{data}}}{N_{\text{CR}}^{\text{MC}}} \quad (5.12)$$

where the parameter μ is the normalisation scale factor described above. Alternatively, the SR yield can be expressed as a function of the number of observed data events in the

CR and the MC Transfer Factor (TF):

$$N_{\text{SR}}^{\text{exp}} = TF \cdot N_{\text{CR}}^{\text{data}}, \quad TF \equiv \frac{N_{\text{SR}}^{\text{MC}}}{N_{\text{CR}}^{\text{MC}}} \quad (5.13)$$

where it is shown explicitly that the result relies on the MC simulation only for the computation of the ratio between the SR and CR predictions. As a direct consequence, the total uncertainty on $N_{\text{SR}}^{\text{exp}}$ is determined exclusively by the Poisson error on $N_{\text{CR}}^{\text{data}}$ and by the uncertainty on the MC extrapolation from the CR to the SR, while any variation in the absolute normalisation of the MC sample (which may be due, for example, to the uncertainty on the cross section of the physics process) has no impact on the final background estimate.

In realistic physics analyses, multiple background processes are normalised in an independent set of CRs with non-negligible cross-contamination. The values of the normalisation factors can be obtained by solving a system of equations with n free parameters and constraints:

$$\left\{ \begin{array}{l} N_{\text{CR},1}^{\text{data}} = \mu_1 N_{\text{CR},1}^{\text{MC},1} + \mu_2 N_{\text{CR},1}^{\text{MC},2} + \dots + \mu_n N_{\text{CR},1}^{\text{MC},n} \\ N_{\text{CR},2}^{\text{data}} = \mu_1 N_{\text{CR},2}^{\text{MC},1} + \mu_2 N_{\text{CR},2}^{\text{MC},2} + \dots + \mu_n N_{\text{CR},2}^{\text{MC},n} \\ \dots \\ N_{\text{CR},n}^{\text{data}} = \mu_1 N_{\text{CR},n}^{\text{MC},1} + \mu_2 N_{\text{CR},n}^{\text{MC},2} + \dots + \mu_n N_{\text{CR},n}^{\text{MC},n} \end{array} \right. \quad (5.14)$$

where μ_i is the normalisation factors of the process i , $N_{\text{CR},j}^{\text{MC},i}$ is the MC yield of the process i in the CR j and $N_{\text{CR},k}^{\text{data}}$ is the number of data events in the CR k .

It is important to mention that, in order to prevent the analysers from being biased during the definition of the search strategy, the SUSY analyses in ATLAS follow a blinding procedure, which consists in hiding the number of observed events in the SRs until the selections are properly optimised and a robust background estimation strategy is in place. Before comparing the background yield with the data in the SRs, the data-MC agreement is hence verified in a set Validation Regions (VRs), where the signal contamination is required to be low and the data are expected to match the Standard Model predictions within uncertainties. As illustrated in Figure 5.9, the VRs are designed to lie within the CR-SR extrapolation region, in order to assess the size of any potential bias in

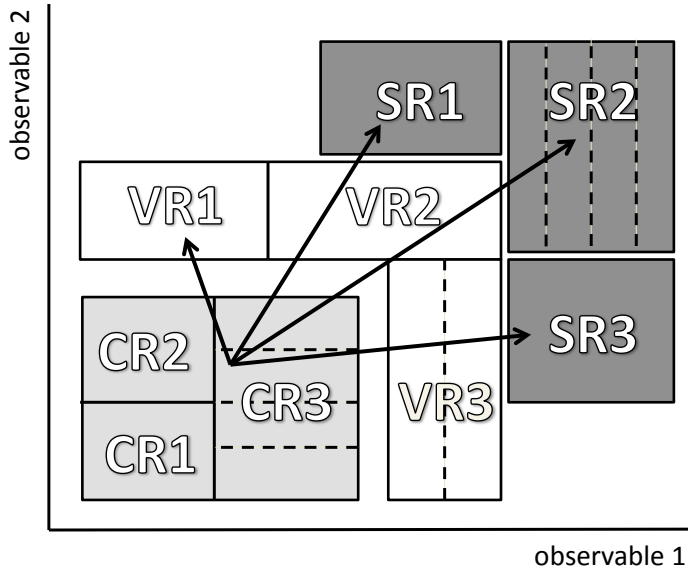


Figure 5.9: Scheme of the general structure of a cut and count analysis, where a set of CRs, VRs and SRs are defined using two observables [178]. The individual regions are required to be mutually orthogonal, and the VRs are located in an intermediate position to verify the quality of the CR-SR extrapolation.

the background estimation procedure. When the analysis is unblinded, the signal should appear as an excess of events in the SRs with respect to the background only hypothesis, with no corresponding effect in the VRs.

5.4 Statistical analysis

The last two sections have presented the general structure of the cut and count analyses in Chapters 6 and 7, that are based on the definition of different types of regions where the relevant signal and background parameters are measured. While a basic assessment of the value of the parameters can be obtained by solving systems as the one in Equation 5.14, the extraction of quantitative results requires appropriate statistical tools

that take into account the stochastic nature of high energy physics phenomena. The analyses in this thesis employ two types of statistical procedures, known as parameter estimation and hypothesis testing: the former allows to measure of a set of parameters from the input dataset, while the latter is used to verify the compatibility of specific models (hypotheses) with the observed data. Both procedures are implemented through the HistFitter framework [178] and are described in detail in the next paragraphs.

5.4.1 Parameter estimation

The primary goal of the physics analyses is the measurement of the parameters through which the data in the Control, Validation and Signal Regions are interpreted. These include the normalisation factors μ_b of the Standard Model backgrounds (see Equation 5.12) and an analogous quantity μ_s for the benchmark signal sample, commonly referred to as signal strength. The rate in any region X of the analysis can be expressed as:

$$N_X = \mu_s N_s + \sum_i \mu_b^i N_b^i \quad (5.15)$$

where N_b^i and N_s are the expected yields of the various processes from the MC simulations. In addition, a set of extra nuisance parameters θ are introduced to describe the impact of the systematic uncertainties on both signal and background, and Equation 5.15 is modified as:

$$N_X = \mu_s N_s (1 + \sum_j \theta_s^j \sigma_s^j) + \sum_i \mu_b^i N_b^i (1 + \sum_j \theta_b^{ij} \sigma_b^{ij}) \quad (5.16)$$

where σ_b^{ij} and σ_s^j are the relative variations of signal and background yields produced by the individual uncertainties. The above expression is configured such that the nominal yields are obtained for $\theta = 0$, while $\theta = \pm 1$ corresponds to the $\pm 1\sigma$ variations. The parameters θ can be common to many physics processes, for example when representing an experimental uncertainty that applies simultaneously to all of them, but they can also be related to single processes if they describe specific uncertainties such as the theory systematics.

The values of the parameters are extracted from the data by constructing a likelihood

function L , which condenses the relevant information of the analysis into a unique expression. The likelihood is a function of the set of free parameters to be measured, and is constrained by the observed number of events in the various regions of the analysis. As discussed in Ref. [178], its general expression is the product of Poisson distributions of event counts in the relevant regions (typically CRs and/or SRs) and of additional distributions that implement the impact of the systematic uncertainties:

$$\begin{aligned} L(\mathbf{N}^{\text{obs}}, \boldsymbol{\theta}^0 | \mu_s, \boldsymbol{\mu}_b, \boldsymbol{\theta}) &= P_{\text{SR}} \times P_{\text{CR}} \times C_{\text{syst}} = \\ &= \prod_{i \in \text{SR,CR}} P(N_i^{\text{obs}} | N_i(\mu_s, \boldsymbol{\mu}_b, \boldsymbol{\theta})) \times C_{\text{syst}}(\boldsymbol{\theta}^0, \boldsymbol{\theta}). \end{aligned} \quad (5.17)$$

The Poisson factors in Equation 5.17 reflect the stochastic nature of the event counts in the SRs and CRs, that are expressed as a function of the signal and background normalisations μ_s and $\boldsymbol{\mu}_b$ and the nuisance parameters $\boldsymbol{\theta}$, as described by Equation 5.16. The additional C_{syst} term is introduced to include the systematic uncertainty in the fit, and has the form of a product of gaussian functions with unit area (one for each independent systematic) that depend on auxiliary measurements $\boldsymbol{\theta}_0$ and nuisance parameters $\boldsymbol{\theta}$. The individual measurements $\boldsymbol{\theta}_0^i$ are generally set to 0, such that the values of the corresponding $\boldsymbol{\theta}^i$ are expected to be approximately 0 ± 1 , reproducing the expected size of the systematic uncertainties through Equation 5.16. Any significant deviation from the expected post-fit value of the $\boldsymbol{\theta}^i$ parameters is referred to as profiling, and indicates that the combination of nominal yield predictions and expected systematic uncertainties is not able to describe accurately the observed data.

Once the likelihood function in Equation 5.17 is built, the values of the parameters are obtained by maximising it following the Maximum Likelihood Estimation (MLE) procedure, illustrated in detail in Ref. [179].

5.4.2 Hypothesis testing

The ultimate purpose of the physics analyses is to determine whether the data indicate or exclude the presence of a signal beyond the Standard Model. This is achieved through a statistical procedure known as hypothesis testing [180], which involves the definition

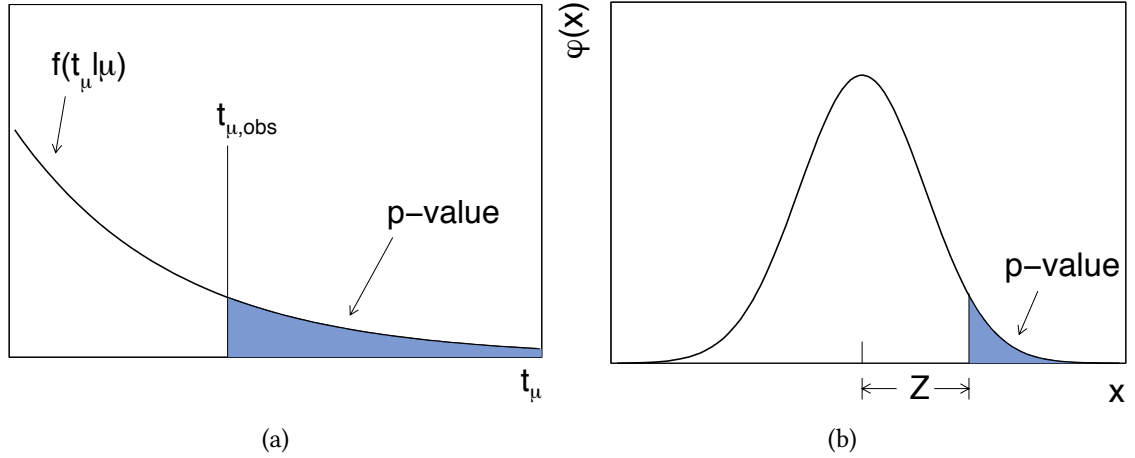


Figure 5.10: Graphical representation of a p -value (a) obtained from a test statistic f for a given signal strength μ (see Equation 5.20) and of the corresponding significance Z (b) [181].

of a null hypothesis H_0 to be tested against an alternative H_1 . In particle physics experiments H_0 and H_1 are chosen as the background only and the signal plus background hypotheses: when targeting a discovery the background only hypothesis is used as H_0 , while the roles are inverted when setting exclusion limits.

The hypothesis H_0 is tested through the computation of a p -value, which represents the probability of observing a larger incompatibility of the data with the predictions under the assumption that H_0 is valid. The p -value is obtained from a function of the data known as test statistic, configured such that it assumes large values when the data are incompatible with H_0 . It is computed as:

$$p = \int_{t_{\text{obs}}}^{\infty} f(t) dt \quad (5.18)$$

where the integral is taken from the observed value of the test statistic to infinity, as shown in Figure 5.10a. For practical purposes, it is convenient to convert the p -value into an equivalent significance Z , defined as the number of standard deviations σ from the mean of a gaussian distribution for which the integral of the tail of the curve is equal to p :

$$Z = \Phi^{-1}(1 - p), \quad (5.19)$$

where Φ^{-1} is the inverse of the cumulative distribution of the gaussian (see Figure 5.10b). The threshold chosen by the particle physics community to declare a discovery is a background rejection of $Z = 5$, which corresponds to $p = 2.87 \times 10^{-7}$, while $Z = 3$ ($p = 0.0013$) is regarded as evidence. Signal models are instead excluded using $p = 0.05$ ($Z = 1.64$).

The Profile Likelihood Ratio

From the above discussion it is clear that the choice of the appropriate test statistic plays a crucial role in the hypothesis testing procedure. The functions used by the LHC experiments are based on a Profile Likelihood Ratio (PLR) [180] obtained from the likelihood in Equation 5.17:

$$\lambda(\mu_s) = \frac{L(\mu_s, \hat{\theta})}{L(\hat{\mu}_s, \hat{\theta})} \quad (5.20)$$

where the vector θ includes the background normalisation factors and the nuisance parameters related to the systematic uncertainties. The denominator $L(\hat{\mu}_s, \hat{\theta})$ corresponds to the absolute maximum of the likelihood function, while the numerator $L(\mu_s, \hat{\theta})$ is the maximum for a given value of μ_s .

Equation 5.20 implies that the range of λ extends from 0 to 1, with larger values corresponding to a better agreement of the data with the μ_s hypothesis under test. A test statistic with the range required by the definition of the p -value (Equation 5.18) can be defined as:

$$t_\mu = -2 \ln \lambda(\mu) \quad (5.21)$$

where larger values of t correspond to a lower compatibility between the data and the hypothesis.

Finally, two versions of the test statistic are defined to perform different types of test:

Test statistic for discovery The discovery of a new signal is targeted by testing the background only hypothesis. This is done by using a PLR function with $\mu_s = 0$,

with the following definition:

$$q_0 = \begin{cases} -2 \ln \lambda(0) & \hat{\mu}_s \geq 0 , \\ 0 & \hat{\mu}_s < 0 , \end{cases} \quad (5.22)$$

where q_0 is set to 0 for negative $\hat{\mu}_s$ to avoid the exclusion of the background hypothesis if a deficit of events is observed in the SRs. As discussed in Ref. [182], an approximate expression of the above test statistic is given by the significance in Equation 5.11.

Test statistic for exclusion When targeting the exclusion of a signal model, the test statistic is instead computed as follows:

$$q_\mu = \begin{cases} -2 \ln \lambda(\mu_s) & \hat{\mu}_s \leq \mu_s , \\ 0 & \hat{\mu}_s > \mu_s . \end{cases} \quad (5.23)$$

where a non-zero signal strength μ_s is assumed.

Distribution of test statistics and CL_s method

In order to compute the p -value it is necessary to determine the distribution of the test statistic $f(t)$ under the assumption that H_0 is true. This can be done by generating pseudo-experiments (toys) in which the values of the observable quantities are generated randomly according to their expected distributions, and the resulting distribution of t is obtained. Alternatively, an asymptotic approximation [181] can be used provided that the size of the event samples in each channel of the analysis is sufficiently large.

A problematic feature of the exclusion test statistic in Equation 5.23 is that it yields a non-negligible probability of excluding signal models to which the analysis is poorly sensitive. While qualitative arguments suggest that these models should not be constrained, low p -values for the signal plus background hypothesis may indeed be obtained in case of significant down-fluctuations of the observed events in the SRs. This pathological behaviour can be avoided by exploiting the fact that such signals yield similar distributions

of discovery and exclusion test statistics, defining an alternative figure of merit for the exclusion [183] as:

$$\text{CL}_s = \frac{p_{\mu_s}}{1 - p_b} \quad (5.24)$$

where p_b and p_{μ_s} are the p -values of the background only and signal plus background hypotheses, and the threshold for a $Z = 2$ (or 95% Confidence Level) exclusion is $\text{CL}_s < 0.05$. In situations where the exclusion and discovery test statistics have similar distributions, the numerator and denominator of Equation 5.24 are of the same order, so the signals are not excluded as expected intuitively. Thanks to this feature, the CL_s is adopted by the ATLAS Collaboration as the standard tool to set exclusion limits on signal models.

5.4.3 Standard fits in SUSY analyses

In summary, the following statistical tools are relevant for the SUSY searches:

Background only fit A first type of fit is performed to estimate the value of the parameters that describe the background processes and the systematic uncertainties. The parameters are fitted only in the CRs, and the signal strength μ_s is neglected. The result of the fit allows to determine the background predictions and the impact of the systematics in the VRs and SRs.

Exclusion fit If no excess is observed in the SRs, the benchmark signal models are tested following the procedure described in the last paragraph, and exclusion limits are set with the CL_s technique.

Discovery fit In case of a significant excess in the SRs, a discovery fit is performed to quantify the significance of the result. This is done by testing the background only hypothesis and computing the associated p -value.

Chapter 6

Search for bottom squarks with two-body RPC decays

6.0.1 Signal models

The analyses in this thesis are targeting the case of a pair-produced \tilde{b} in an R -parity conserving (RPC) scenario with $\tilde{\chi}_1^0$ LSP (Chapter 6), and a pair-produced \tilde{t} which decays through an R -parity violating (RPV) coupling in a bottom quark and a lepton (Chapter 7). A description of the signal models is provided below:

RPC \tilde{b} signal The analysis discussed in Chapter 6 is a comprehensive search for \tilde{b} pair-production with RPC two-body decays, where the $\tilde{\chi}_1^0$ and the $\tilde{\chi}_1^+$ are assumed to be the LSP and the NLSP respectively. The decays of the \tilde{b} into $b\tilde{\chi}_1^0$ or $t\tilde{\chi}_1^+$ are studied under the assumption of small mass splitting between $\tilde{\chi}_1^+$ and $\tilde{\chi}_1^0$, such that the subsequent $\tilde{\chi}_1^+ \rightarrow W^*\tilde{\chi}_1^0$ decay yields no visible objects in the detector¹. The first signal model targeted by the analysis is shown in Figure 6.1a, where the \tilde{b} is assumed to decay into $b\tilde{\chi}_1^0$ with 100% BR, yielding a final state with two bottom

¹For $\Delta M(\tilde{\chi}_1^+, \tilde{\chi}_1^0)$ of the order of the GeV, the decay of the $\tilde{\chi}_1^+$ yields only soft objects in addition to the $\tilde{\chi}_1^0$. Since these objects are below the minimum threshold required to be reconstructed by the detector, the experimental signatures of $\tilde{\chi}_1^+$ and $\tilde{\chi}_1^0$ are effectively equivalent. In practice, the models studied in this thesis assume $\Delta M(\tilde{\chi}_1^+, \tilde{\chi}_1^0) = 1$ GeV, for which the above condition is satisfied.

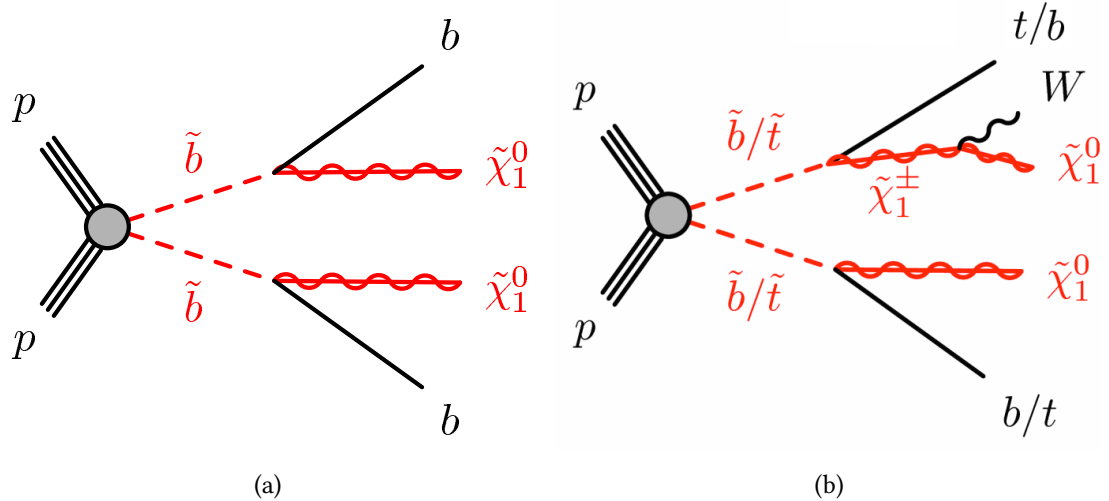


Figure 6.1: Benchmark signal models targeted by the analysis in Chapter 6. Diagram (a) shows a pair-produced \tilde{b} decaying into a $b\tilde{\chi}_1^0$ pair, yielding an experimental signature with two b -jets and E_T^{miss} . Diagram (b) shows a mixed decay of the \tilde{b} (or \tilde{t}) into $b\tilde{\chi}_1^0$ and $t\tilde{\chi}_1^+$ (or $t\tilde{\chi}_1^0$ and $b\tilde{\chi}_1^+$), which results in a $tb + E_T^{\text{miss}}$ final state under the assumption of small $\Delta M(\tilde{\chi}_1^+, \tilde{\chi}_1^0)$.

quarks and invisible particles. In addition, a mixed decay scenario of the \tilde{b} into $b\tilde{\chi}_1^0$ and $t\tilde{\chi}_1^+$ with 50% BR is considered, yielding a more complex model where 25% of the events are as in Figure 6.1a, 50% of them yield the asymmetric $tb + E_T^{\text{miss}}$ final state in Figure 6.1b and the remaining 25% yields a pure $tt + E_T^{\text{miss}}$ final state. It should be noted that, under the assumption of small $\Delta M(\tilde{\chi}_1^+, \tilde{\chi}_1^0)$, the $tb + E_T^{\text{miss}}$ diagram can be interpreted equivalently in terms of \tilde{b} or \tilde{t} pair-production. The case of a pure $\tilde{b} \rightarrow t\tilde{\chi}_1^+$ decay with 100% BR is not treated in this thesis because it yields a pure $tt + E_T^{\text{miss}}$ final state, which is already targeted by a dedicated analysis [].

RPV \tilde{t} signal The signal targeted by the analysis in Chapter 7 is a pair-produced \tilde{t} decaying into a b -quark and a charged lepton ($\tilde{t} \rightarrow b\ell$), shown in the diagram in Figure 6.2 (and previously in Figure 5.6a). Contrarily to the \tilde{b} signals described

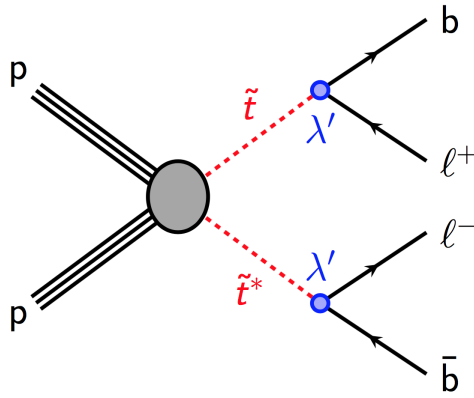


Figure 6.2: Benchmark signal model targeted by the analysis in Chapter 7, with a pair-produced stop decaying into $b\ell$ pairs through an RPV coupling.

above, this model yields no E_T^{miss} in the final state, because no invisible particles are produced. The BRs of the \tilde{t} decay are related to the neutrino mass hierarchy as described in Section 1.3.4, and a significant phase space can be explored with the Run 2 data of the LHC. The signal model yields events with two oppositely charged leptons and two b -jets, where the $b\ell$ pairs from the same \tilde{t} decay are produced with invariant mass corresponding to the mass of the \tilde{t} .

6.0.2 Discriminating variables

The following variables, calculated in each given event, have been proven to be useful in rejecting the Standard Model background effectively and for defining background control regions (CRs). The definitions assume a preliminary selection of events with one lepton, missing transverse energy and two b -tagged jets, as discussed in detail in section ???. When only one b -jet is present, at least one additional light flavour jet is required and the light jet with leading P_T takes the role of the second b -jet in each variable definition.

- E_{miss}^T

The first relevant variable is the missing transverse energy, whose reconstruction and definition are discussed in the previous chapter and in section 5.3.2.

- $\delta\phi_{min}(b, E_{miss}^T)$

This is defined as the minimum azimuthal distance between any b-tagged jet and the missing transverse energy E_{miss}^T :

$$\delta\phi_{min}(b, E_{miss}^T) = \min(|\phi_{1^{st} \text{ b-jet}} - \phi_{E_{miss}^T}|, \dots, |\phi_{n^{th} \text{ b-jet}} - \phi_{E_{miss}^T}|) \quad (6.1)$$

This variable is used to remove multijet backgrounds with a cut of $\delta\phi_{min} > 0.4$.

- H_T

This is the scalar sum of the transverse momentum of the two b-jets and the first light jet, if present:

$$H_T = P_{b_1}^T + P_{b_2}^T \quad (+P_{l_{j_1}}^T) \quad (6.2)$$

For events with only one b-jet, the transverse momenta of the b-jet and the leading light jet are always summed, as previously discussed. In addition, if more light jets are present, the transverse momentum of the sub-leading light jet is included too.

- M_{eff}

The so called effective mass is defined as the scalar sum of E_{miss}^T and the previously defined H_T :

$$M_{eff} = H_T + E_{miss}^T \quad (6.3)$$

- $E_{MissSignif}^T$

The significance of E_{miss}^T , expressed in $\text{GeV}^{1/2}$, is obtained as:

$$E_{MissSignif}^T = \frac{E_{miss}^T}{\sqrt{H_T}} \quad (6.4)$$

- $M_T(\ell, E_{miss}^T)$

This variable is the transverse mass of the system composed by the lepton and E_{miss}^T :

$$M_T = \sqrt{2p_\ell^T E_{miss}^T - 2\mathbf{p}_{ell}^T \cdot \mathbf{p}_{miss}^T} = \sqrt{2p_\ell^T p_{miss}^T [1 - \cos(\phi_\ell - \phi_{miss})]} \quad (6.5)$$

If the missing transverse energy and the lepton come from the same W boson decay, the M_T variable has an upper bound given by the W mass. This circumstance

occurs for most of the relevant backgrounds listed in section 5.2.1, such as the $t\bar{t}$ or the $W + \text{jets}$, while in the characteristic decay chains of the signals the E_{miss}^T comes also from the neutralinos (see figure ??), therefore the same upper bound is not present. As a result, this variable is extremely useful for the discrimination between signal and background.

- $aM_{T2}(b_1, b_2, \ell, E_{miss}^T)$

This variable is closely related to the so called *transverse mass* M_{T2} [184] [185], specifically designed for pair produced particles that decay in both visible and invisible products, yielding a characteristic final state illustrated by figure 6.3. The idea is to decompose the missing energy into two transverse vectors, which are interpreted as the transverse momenta of the invisible particles in the two legs of the event. For each of these decompositions, two transverse masses are built by combining the invisible and visible transverse momenta of the two legs, then the maximum of the two values is taken. By repeating this operation using all the possible decompositions of E_{miss}^T , and by taking the minimum between all the calculated maxima, the resulting value will be lower than the endpoint for the decay on a single leg. For example, for WW production this quantity has an upper bound given by the W mass. Assuming a null mass for the invisible particles, the definition for M_{T2} is thus

$$M_{T2}^2 \left(\vec{p}_T^\alpha, \vec{p}_T^\beta, \vec{p}_T^m \right) = \min_{\vec{q}_T^1 + \vec{q}_T^2 = \vec{p}_T^m} \left\{ \max \left[M_T^2 \left(\vec{p}_T^\alpha, \vec{q}_T^1 \right), M_T^2 \left(\vec{p}_T^\beta, \vec{q}_T^2 \right) \right] \right\} \quad (6.6)$$

where M_T indicates the usual transverse mass, \vec{p}_T^α and \vec{p}_T^β are the momenta of the visible decay products, and \vec{q}_T^1 and \vec{q}_T^2 are the vectors that decompose the missing transverse momentum by satisfying $\vec{q}_T^1 + \vec{q}_T^2 = \vec{p}_T^m$. The minimum is taken over the set of choices of \vec{q}_T^1 and \vec{q}_T^2 .

The aM_{T2} variable used in our analysis is a variation of M_{T2} specifically designed for the targeted signal decay chain and for the $t\bar{t}$ background reduction in the one lepton channel, driven by the necessity to associate the lepton with the correct

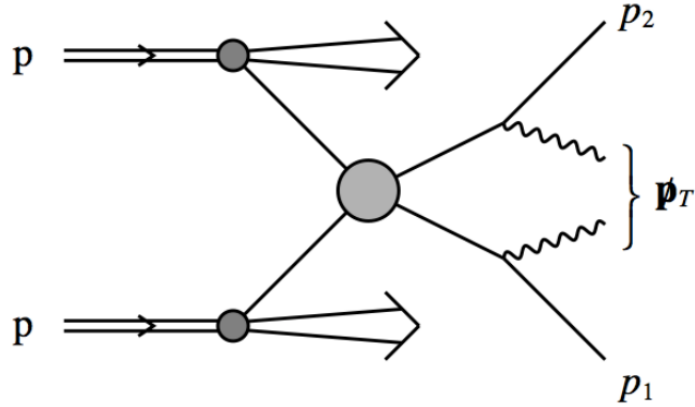


Figure 6.3: Diagram of a generic process suitable for the calculation of the M_{T2} variable. After the pair production of a particle, the two decay legs yield both visible and invisible products.

decay leg. The a in the front stands for *asymmetric* transverse mass. To obtain its value it is first necessary to compute the invariant masses

$$M_{b\ell}^1 = M(b_1 + \ell, b_2) \quad \text{and} \quad M_{b\ell}^2 = M(b_1, b_2 + \ell) \quad (6.7)$$

where $M()$ indicates the invariant mass calculation and b_1, b_2 and ℓ are the Lorentz four-vectors of the two b-jets² and the lepton respectively. At this point, aM_{T2} is obtained using the following procedure:

- If the condition $\min \{M_{b\ell}^1, M_{b\ell}^2\} > 170$ GeV is satisfied, where 170 GeV is approximately the top quark mass, the event is discarded. This is done because $M_{b\ell}^{min} > 170$ GeV indicates that the lepton is not compatible with a top decay, therefore the event is different from the signal hypothesis sketched in figure ???. The validity of this cut has been tested and the relative plots are shown in section ??.
- If $M_{b\ell}^1 < 170$ GeV and $M_{b\ell}^2 > 170$ GeV, the value of aM_{T2} is computed as

$$aM_{T2} = M_{T2}(b_1 + \ell, b_2)$$

²As usual, if only one b-jet is present the role of the second b-jet is taken by the light jet with leading transverse momentum.

because the invariant mass values indicate that the lepton is coming from the same leg of the first b-jet.

- Similarly, if $M_{b\ell}^2 < 170$ GeV and $M_{b\ell}^1 > 170$ GeV, the aM_{T2} value is given by

$$aM_{T2} = M_{T2}(b_1, b_2 + \ell)$$

- Finally, if both invariant masses are below 170 GeV, the minimum between the two possible combinations is taken:

$$aM_{T2} = \min [M_{T2}(b_1 + \ell, b_2), M_{T2}(b_1, b_2 + \ell)]$$

- M_{CT}

The so called cotransverse mass was tested as a possible alternative to aM_{T2} (see the N-1 plots paragraph in section ??). Similarly to aM_{T2} , it is designed to measure the masses of pair-produced semi-invisibly decaying heavy particles:

$$M_{CT}^2(v_1, v_2) = [E_T(v_1) + E_T(v_2)]^2 - [\mathbf{p}_T(v_1) + \mathbf{p}_T(v_2)]^2 \quad (6.8)$$

where $E_T = \sqrt{p_T + m^2}$ and v_1 and v_2 are two identical visible particles or particle aggregates that, in this analysis, are taken to be the two b-jets. The cotransverse mass is invariant under equal and opposite boosts of the parent particles in the transverse plane, and for parent particles produced with small transverse boosts it has an upper bound given by an analytical combination of the particle masses. For $t\bar{t}$ events the upper bound is at 135 GeV, while for the stop (or, equivalently, for the sbottom) it is given by

$$M_{CT}^{max} = \frac{m^2(\tilde{t}) - m^2(\tilde{\chi}_1^0)}{m(\tilde{t})}$$

- M_{bb}

An additional variable that was tested is the invariant mass M_{bb} of the two b-jets.

- $N_{ExtraJets}$

This variable was used for the definition of exclusive signal regions on the number of jets, that are not discussed in this thesis. It is defined as the number of the non b-tagged jets with $p_T > 50$ GeV.

6.0.3 Data driven estimates of the Z background

Chapter 7

Search for top squarks with RPV decays in b - ℓ pairs

Chapter 8

Conclusions

Appendix A

Single electron trigger rate

Appendix B

Additional b -tagging efficiency plots

This appendix includes a set of plots that complete the b -tagging performance studies presented in Chapter 4. Figures B.1-B.2 show the uncertainty on b , c and light jets efficiency as a function of jet p_T in Z' and $t\bar{t}$ samples for the 77% fixed efficiency WP, to be compared with Figures 4.4-4.5 where the fixed cut WP is used. Figure B.3 is instead showing the total impact of jet uncertainties on the tagging efficiency of b , c and light jet efficiency in $t\bar{t}$, and of b -jets in Z' , for the 77% fixed cut WP.

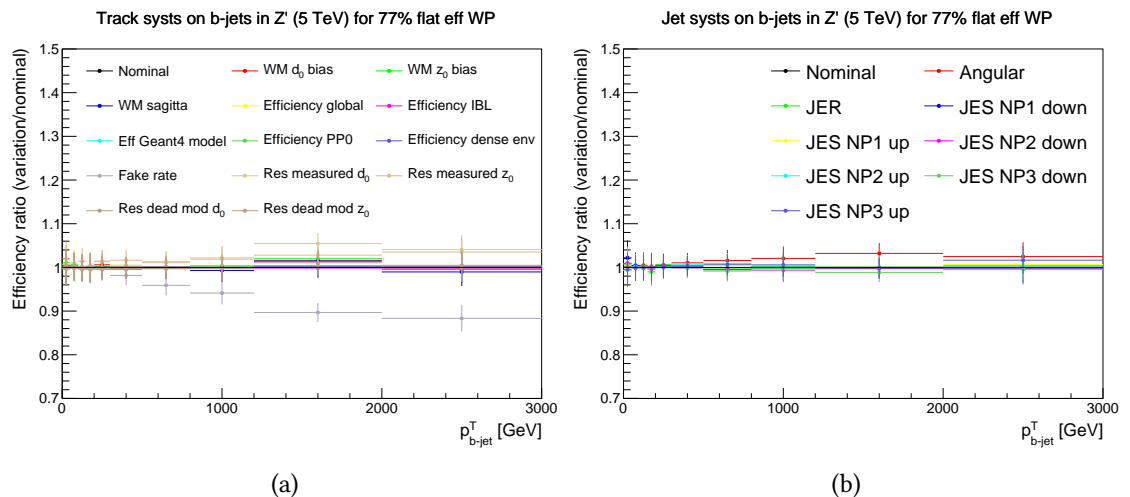


Figure B.1: Ratio of modified and nominal b -tagging efficiencies vs b -jet p_T in a 5 TeV Z' sample for the 77% fixed efficiency WP, showing track (a) and jet (b) systematics.

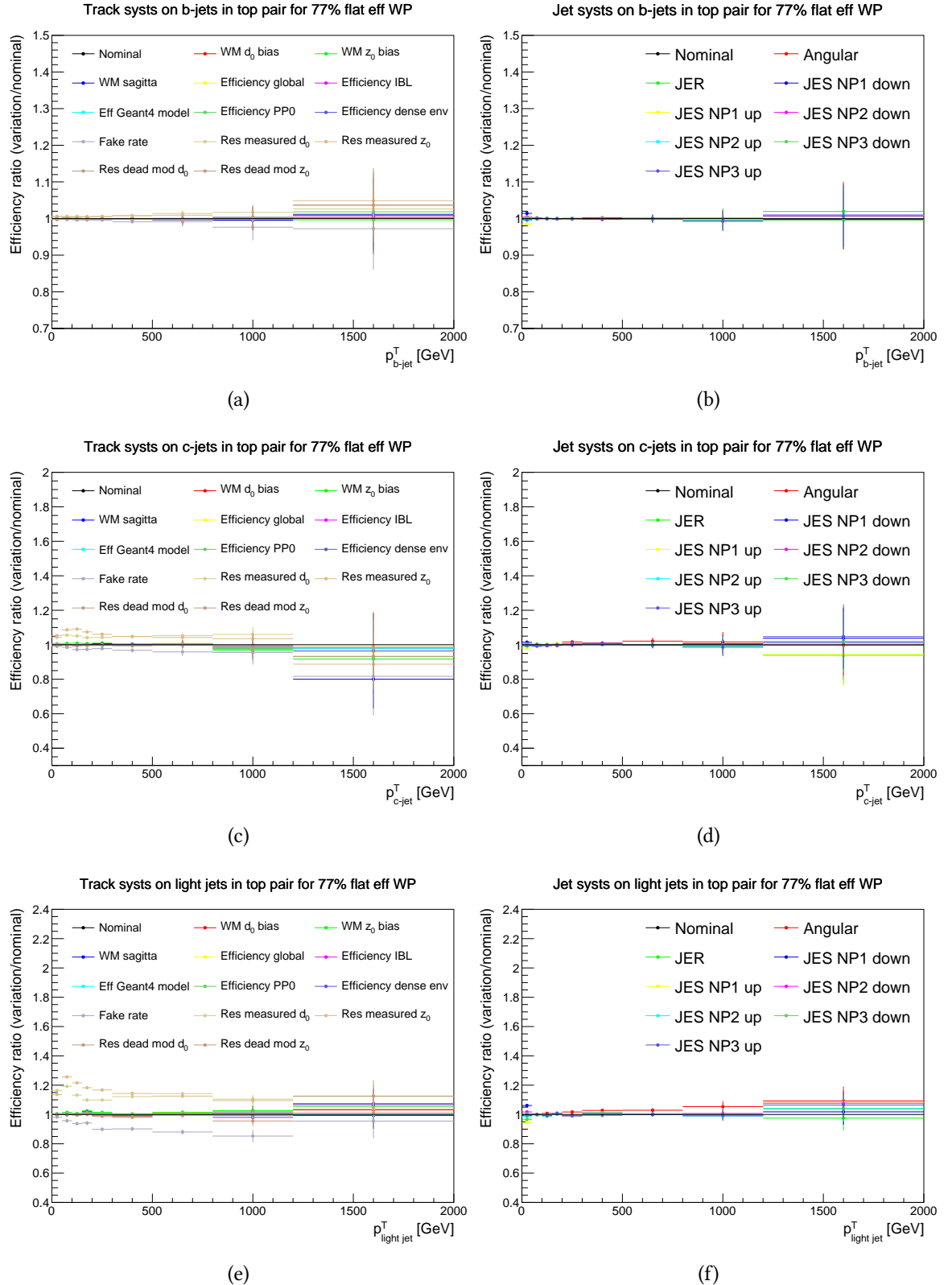


Figure B.2: Ratio of modified and nominal b -tagging efficiencies vs jet p_T in a $t\bar{t}$ sample for the 77% fixed efficiency WP, showing the impact of the individual track (left) and jet (right) systematics on b (top), c (middle) and light (bottom) jets.

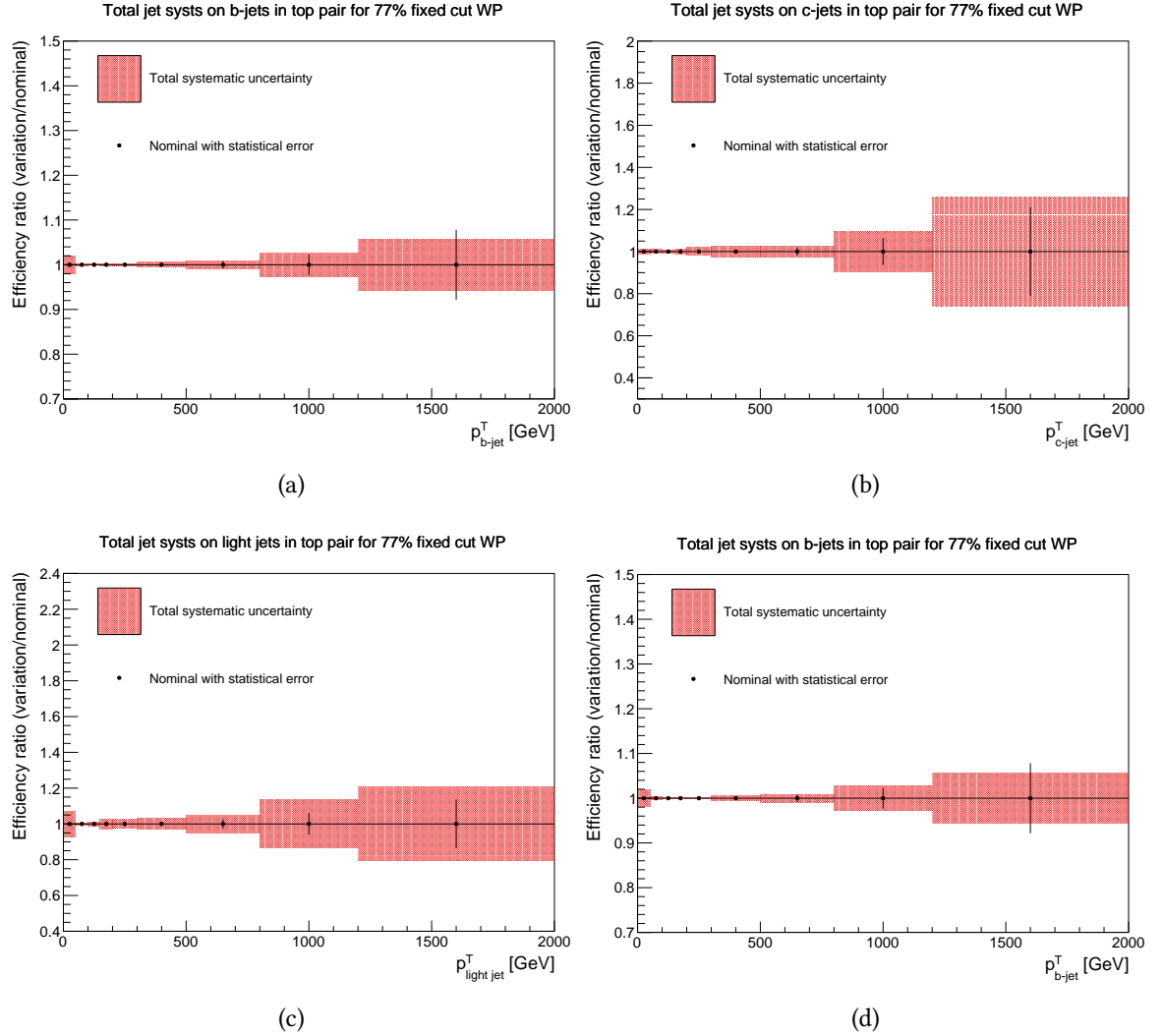


Figure B.3: Relative uncertainty caused by jet systematics on the tagging efficiency vs jet p_T for b (a), c (b) and light jets (c) in a $t\bar{t}$ sample, and for b -jets in a Z' sample (d), for the 77% fixed cut WP.

Bibliography

- [1] Michael E Peskin and Daniel V Schroeder. *An introduction to quantum field theory*; 1995 ed. Westview, Boulder, CO, 1995. Includes exercises.
- [2] S. L. Glashow. Partial Symmetries of Weak Interactions. *Nucl. Phys.*, 22:579–588, 1961.
- [3] Abdus Salam and John Clive Ward. Electromagnetic and weak interactions. *Phys. Lett.*, 13:168–171, 1964.
- [4] Steven Weinberg. A Model of Leptons. *Phys. Rev. Lett.*, 19:1264–1266, 1967.
- [5] H. Fritzsch, Murray Gell-Mann, and H. Leutwyler. Advantages of the Color Octet Gluon Picture. *Phys. Lett.*, 47B:365–368, 1973.
- [6] David J. Gross and Frank Wilczek. Ultraviolet Behavior of Nonabelian Gauge Theories. *Phys. Rev. Lett.*, 30:1343–1346, 1973.
- [7] F. Englert and R. Brout. Broken Symmetry and the Mass of Gauge Vector Mesons. *Phys. Rev. Lett.*, 13:321–323, 1964.
- [8] Peter W. Higgs. Broken Symmetries and the Masses of Gauge Bosons. *Phys. Rev. Lett.*, 13:508–509, 1964.
- [9] Peter W. Higgs. Broken symmetries, massless particles and gauge fields. *Phys. Lett.*, 12:132–133, 1964.

- [10] ATLAS and CMS Collaborations. Measurements of the Higgs boson production and decay rates and constraints on its couplings from a combined ATLAS and CMS analysis of the LHC pp collision data at $\sqrt{s} = 7$ and 8 TeV. *JHEP*, 08:045, 2016.
- [11] The ATLAS Collaboration. Observation of a new particle in the search for the Standard Model Higgs boson with the ATLAS detector at the LHC. *Phys. Lett.*, B716:1–29, 2012.
- [12] The CMS Collaboration. Observation of a new boson at a mass of 125 GeV with the CMS experiment at the LHC. *Phys.Lett.*, B716:30–61, 2012.
- [13] The ATLAS Collaboration. Measurement of the Higgs boson mass from the $H \rightarrow \gamma\gamma$ and $H \rightarrow ZZ^* \rightarrow 4\ell$ channels with the ATLAS detector using 25 fb^{-1} of pp collision data. *Phys. Rev.*, D90(5):052004, 2014.
- [14] The CMS Collaboration. Precise determination of the mass of the Higgs boson and tests of compatibility of its couplings with the standard model predictions using proton collisions at 7 and 8 TeV. *Eur. Phys. J.*, C75(5):212, 2015.
- [15] Leonard Susskind. Dynamics of Spontaneous Symmetry Breaking in the Weinberg-Salam Theory. *Phys. Rev.*, D20:2619–2625, 1979.
- [16] Gerard 't Hooft. Naturalness, chiral symmetry, and spontaneous chiral symmetry breaking. *NATO Sci. Ser. B*, 59:135–157, 1980.
- [17] M. J. G. Veltman. The Infrared - Ultraviolet Connection. *Acta Phys. Polon.*, B12:437, 1981.
- [18] Gianfranco Bertone, Dan Hooper, and Joseph Silk. Particle dark matter: Evidence, candidates and constraints. *Phys. Rept.*, 405:279–390, 2005.
- [19] C. Giunti, C. W. Kim, and U. W. Lee. Running coupling constants and grand unification models. *Mod. Phys. Lett.*, A6:1745–1755, 1991.

- [20] Frank Wilczek David J. Gross, H. David Politzer. The 2004 Nobel Prize in Physics - Popular Information. *Nobel Media AB 2014*, 2004.
- [21] W. M. Alberico and S. M. Bilenky. Neutrino oscillations, masses and mixing. *Phys. Part. Nucl.*, 35:297–323, 2004. [Fiz. Elem. Chast. Atom. Yadra35,545(2004)].
- [22] Makoto Kobayashi and Toshihide Maskawa. CP Violation in the Renormalizable Theory of Weak Interaction. *Prog. Theor. Phys.*, 49:652–657, 1973.
- [23] M. B. Gavela, P. Hernandez, J. Orloff, and O. Pene. Standard model CP violation and baryon asymmetry. *Mod. Phys. Lett.*, A9:795–810, 1994.
- [24] J. Wess and B. Zumino. Supergauge Transformations in Four-Dimensions. *Nucl. Phys.*, B70:39–50, 1974.
- [25] Abdus Salam and J. A. Strathdee. Supersymmetry and Nonabelian Gauges. *Phys. Lett.*, 51B:353–355, 1974.
- [26] Sidney R. Coleman and J. Mandula. All Possible Symmetries of the S Matrix. *Phys. Rev.*, 159:1251–1256, 1967.
- [27] H. Weyl. Electron and Gravitation. 1. (In German). *Z. Phys.*, 56:330–352, 1929. [Surveys High Energ. Phys.5,261(1986)].
- [28] Glennys R. Farrar and Pierre Fayet. Phenomenology of the Production, Decay, and Detection of New Hadronic States Associated with Supersymmetry. *Phys. Lett.*, 76B:575–579, 1978.
- [29] Manuel Drees, Rohini Godbole, and Probir Roy. *Theory and phenomenology of Sparticles: an account of four-dimensional N=1 supersymmetry in high-energy physics*. World Scientific, Singapore, 2004.
- [30] K. Hidaka and A. Bartl. Impact of bosonic decays on the search for the lighter stop and sbottom squarks. *Phys. Lett.*, B501:78–85, 2001.

- [31] Stephen P. Martin. A Supersymmetry primer. *Adv.Ser.Direct.High Energy Phys.*, 21:1–153, 2010.
- [32] Riccardo Barbieri and G. F. Giudice. Upper Bounds on Supersymmetric Particle Masses. *Nucl. Phys.*, B306:63–76, 1988.
- [33] Michele Papucci, Joshua T. Ruderman, and Andreas Weiler. Natural SUSY Endures. *JHEP*, 09:035, 2012.
- [34] Zachary Marshall, Burt A. Ovrut, Austin Purves, and Sogee Spinner. Spontaneous R -Parity Breaking, Stop LSP Decays and the Neutrino Mass Hierarchy. *Phys. Lett.*, B732:325–329, 2014.
- [35] M. C. Gonzalez-Garcia, Michele Maltoni, Jordi Salvado, and Thomas Schwetz. Global fit to three neutrino mixing: critical look at present precision. *JHEP*, 12:123, 2012.
- [36] Lyndon Evans and Philip Bryant. LHC Machine. *JINST*, 3:S08001, 2008.
- [37] The ATLAS Collaboration. The ATLAS Experiment at the CERN Large Hadron Collider. *JINST*, 3:S08003, 2008.
- [38] John M. Campbell, J. W. Huston, and W. J. Stirling. Hard Interactions of Quarks and Gluons: A Primer for LHC Physics. *Rept. Prog. Phys.*, 70:89, 2007.
- [39] Ringaile Placakyte. Parton Distribution Functions. In *Proceedings, 31st International Conference on Physics in collisions (PIC 2011): Vancouver, Canada, August 28-September 1, 2011*, 2011.
- [40] Bora Isildak. *Measurement of the differential dijet production cross section in proton-proton collisions at $\sqrt{s} = 7$ TeV*. PhD thesis, Bogazici U., 2011.
- [41] S. Myers and E. Picasso . The design, construction and commissioning of the CERN large Electron-Positron collider. *Contemporary Physics*, 31(6):387–403, 1990.

- [42] Design Report Tevatron 1 project. Technical Report FERMILAB-DESIGN-1984-01, 1984.
- [43] ALEPH, DELPHI, L3, OPAL, SLD Collaborations, LEP Electroweak Working Group, SLD Electroweak Group, and SLD Heavy Flavour Group. Precision electroweak measurements on the Z resonance. *Phys. Rept.*, 427:257–454, 2006.
- [44] The CDF Collaboration. Observation of top quark production in $\bar{p}p$ collisions. *Phys. Rev. Lett.*, 74:2626–2631, 1995.
- [45] The D0 Collaboration. Observation of the top quark. *Phys. Rev. Lett.*, 74:2632–2637, 1995.
- [46] C Llewellyn Smith. Genesis of the Large Hadron Collider. Genesis of the Large Hadron Collider. *Philos. Trans. R. Soc. Lond. A*, 373(2032):20140037, 2014.
- [47] The ALEPH, DELPHI, L3, OPAL Collaboration, and the LEP Working Group for Higgs Boson Searches. Search for the standard model Higgs boson at LEP. *Phys. Lett.*, B565:61–75, 2003.
- [48] The CDF Collaboration. Combined search for the standard model Higgs boson decaying to a bb pair using the full CDF data set. *Phys. Rev. Lett.*, 109:111802, 2012.
- [49] The D0 Collaboration. Combined Search for the Standard Model Higgs Boson Decaying to $b\bar{b}$ Using the D0 Run II Data Set. *Phys. Rev. Lett.*, 109:121802, 2012.
- [50] Michael Benedikt, Paul Collier, V Mertens, John Poole, and Karlheinz Schindl. *LHC Design Report v3*. CERN Yellow Reports: Monographs. CERN, Geneva, 2004.
- [51] The UA1 Collaboration. Experimental Observation of Isolated Large Transverse Energy Electrons with Associated Missing Energy at $\sqrt{s} = 540$ GeV. *Phys. Lett.*, 122B:103–116, 1983. [,611(1983)].

- [52] The UA2 Collaboration. Observation of Single Isolated Electrons of High Transverse Momentum in Events with Missing Transverse Energy at the CERN anti-p p Collider. *Phys. Lett.*, 122B:476–485, 1983.
- [53] ATLAS Luminosity Public Results. <https://twiki.cern.ch/twiki/bin/view/AtlasPublic/LuminosityPublicResults>.
- [54] Oliver Sim Brüning, Paul Collier, P Lebrun, Stephen Myers, Ranko Ostojic, John Poole, and Paul Proudlock. *LHC Design Report v1*. CERN Yellow Reports: Monographs. CERN, Geneva, 2004.
- [55] The CMS Collaboration. The CMS Experiment at the CERN LHC. *JINST*, 3:S08004, 2008.
- [56] The LHCb Collaboration. The LHCb Detector at the LHC. *JINST*, 3:S08005, 2008.
- [57] The ALICE Collaboration. The ALICE experiment at the CERN LHC. *JINST*, 3:S08002, 2008.
- [58] The TOTEM Collaboration. The TOTEM experiment at the CERN Large Hadron Collider. *JINST*, 3:S08007, 2008.
- [59] The LHCf Collaboration. The LHCf detector at the CERN Large Hadron Collider. *JINST*, 3:S08006, 2008.
- [60] The MoEDAL Collaboration. Technical Design Report of the MoEDAL Experiment. Technical Report MoEDAL-TDR-001, 2009.
- [61] W. W. Armstrong et al. ATLAS: Technical proposal for a general-purpose p-p experiment at the Large Hadron Collider at CERN. *CERN-LHCC-94-43*, 1994.
- [62] The ATLAS Collaboration. ATLAS magnet system: Technical design report. *CERN-LHCC-97-18*, 1997.
- [63] G. Acquistapace et al. CMS, the magnet project: Technical design report. *CERN-LHCC-97-10*, 1997.

- [64] The ATLAS Collaboration. The ATLAS Inner Detector commissioning and calibration. *Eur. Phys. J.*, C70:787–821, 2010.
- [65] Norbert Wermes and G Hallewel. *ATLAS pixel detector: Technical Design Report*. Technical Design Report ATLAS. CERN, Geneva, 1998.
- [66] M Capeans, G Darbo, K Einsweiller, M Elsing, T Flick, M Garcia-Sciveres, C Gemme, H Pernegger, O Rohne, and R Vuillermet. ATLAS Insertable B-Layer Technical Design Report. Technical Report CERN-LHCC-2010-013. ATLAS-TDR-19, Sep 2010.
- [67] Malte Backhaus. The upgraded Pixel Detector of the ATLAS Experiment for Run2 at the Large Hadron Collider. Technical Report ATL-INDET-PROC-2015-015, CERN, Geneva, Dec 2015.
- [68] A. Abdesselam et al. The barrel modules of the ATLAS semiconductor tracker. *Nucl. Instrum. Meth.*, A568:642–671, 2006.
- [69] A. Abdesselam et al. The ATLAS semiconductor tracker end-cap module. *Nucl. Instrum. Meth.*, A575:353–389, 2007.
- [70] E. Abat et al. The ATLAS TRT barrel detector. *JINST*, 3:P02014, 2008.
- [71] E. Abat et al. The ATLAS TRT end-cap detectors. *JINST*, 3:P10003, 2008.
- [72] The ATLAS Collaboration. ATLAS liquid argon calorimeter: Technical design report. *CERN-LHCC-96-41*, 1996.
- [73] The ATLAS Collaboration. *ATLAS tile calorimeter: Technical Design Report*. Technical Design Report ATLAS. CERN, Geneva, 1996.
- [74] The ATLAS Collaboration. *ATLAS muon spectrometer: Technical Design Report*. Technical Design Report ATLAS. CERN, Geneva, 1997.
- [75] The ATLAS Collaboration. Performance of the ATLAS Trigger System in 2015. *Eur. Phys. J.*, C77(5):317, 2017.

- [76] B. Abbott, R. Blair, G. Crone, B. Green, J. Love, J. Proudfoot, O. Rifki, W. P. Vazquez, W. Vandelli, and J. Zhang. The evolution of the region of interest builder for the ATLAS experiment at CERN. *JINST*, 11(02):C02080, 2016.
- [77] The ATLAS Collaboration. *ATLAS level-1 trigger: Technical Design Report*. Technical Design Report ATLAS. CERN, Geneva, 1998.
- [78] The ATLAS Collaboration. Technical Design Report for the Phase-I Upgrade of the ATLAS TDAQ System. *CERN-LHCC-2013-018*, 2013.
- [79] Peter Jenni, Marzio Nessi, Markus Nordberg, and Kenway Smith. *ATLAS high-level trigger, data-acquisition and controls: Technical Design Report*. Technical Design Report ATLAS. CERN, Geneva, 2003.
- [80] M. zur Nedden. The lhc run 2 atlas trigger system: design, performance and plans. *Journal of Instrumentation*, 12(03):C03024, 2017.
- [81] M Shochet, L Tompkins, V Cavaliere, P Giannetti, A Annovi, and G Volpi. Fast TracKer (FTK) Technical Design Report. Technical Report CERN-LHCC-2013-007. ATLAS-TDR-021, Jun 2013. ATLAS Fast Tracker Technical Design Report.
- [82] Matt Dobbs and Jorgen Beck Hansen. The HepMC C++ Monte Carlo event record for High Energy Physics. *Comput. Phys. Commun.*, 134:41–46, 2001.
- [83] Guido Altarelli and G. Parisi. Asymptotic Freedom in Parton Language. *Nucl. Phys.*, B126:298–318, 1977.
- [84] V. N. Gribov and L. N. Lipatov. Deep inelastic e p scattering in perturbation theory. *Sov. J. Nucl. Phys.*, 15:438–450, 1972. [Yad. Fiz.15,781(1972)].
- [85] Yuri L. Dokshitzer. Calculation of the Structure Functions for Deep Inelastic Scattering and e+ e- Annihilation by Perturbation Theory in Quantum Chromodynamics. *Sov. Phys. JETP*, 46:641–653, 1977. [Zh. Eksp. Teor. Fiz.73,1216(1977)].

- [86] Hung-Liang Lai, Marco Guzzi, Joey Huston, Zhao Li, Pavel M. Nadolsky, Jon Pumplin, and C. P. Yuan. New parton distributions for collider physics. *Phys. Rev.*, D82:074024, 2010.
- [87] J. Pumplin, D. R. Stump, J. Huston, H. L. Lai, Pavel M. Nadolsky, and W. K. Tung. New generation of parton distributions with uncertainties from global QCD analysis. *JHEP*, 07:012, 2002.
- [88] Richard D. Ball et al. Parton distributions for the LHC Run II. *JHEP*, 04:040, 2015.
- [89] Richard D. Ball et al. Parton distributions with LHC data. *Nucl. Phys.*, B867:244–289, 2013.
- [90] A. D. Martin, W. J. Stirling, R. S. Thorne, and G. Watt. Parton distributions for the LHC. *Eur. Phys. J.*, C63:189–285, 2009.
- [91] T. Kinoshita. Mass singularities of Feynman amplitudes. *J. Math. Phys.*, 3:650–677, 1962.
- [92] Lee, T. D. and Nauenberg, M. Degenerate Systems and Mass Singularities. *Phys. Rev.*, 133:B1549–B1562, Mar 1964.
- [93] J.A. Aguilar-Saavedra, D. Amidei, A. Juste, and M. Perez-Victoria. Asymmetries in top quark pair production at hadron colliders. *Rev. Mod. Phys.*, 87(arXiv:1406.1798. CERN-PH-TH-2014-101):421. 36 p, Jun 2014. Comments: RevTeX 36 pages. To be published in Reviews of Modern Physics. Fixed fonts in some equations.
- [94] V. V. Sudakov. Vertex parts at very high-energies in quantum electrodynamics. *Sov. Phys. JETP*, 3:65–71, 1956. [Zh. Eksp. Teor. Fiz.30,87(1956)].
- [95] S. Catani, F. Krauss, R. Kuhn, and B. R. Webber. QCD matrix elements + parton showers. *JHEP*, 11:063, 2001.

- [96] Michelangelo L. Mangano, Mauro Moretti, Fulvio Piccinini, and Michele Trecan. Matching matrix elements and shower evolution for top-quark production in hadronic collisions. *JHEP*, 01:013, 2007.
- [97] B. R. Webber. A QCD Model for Jet Fragmentation Including Soft Gluon Interference. *Nucl. Phys.*, B238:492–528, 1984.
- [98] G. Marchesini and B. R. Webber. Monte Carlo Simulation of General Hard Processes with Coherent QCD Radiation. *Nucl. Phys.*, B310:461–526, 1988.
- [99] Bo Andersson, G. Gustafson, G. Ingelman, and T. Sjostrand. Parton Fragmentation and String Dynamics. *Phys. Rept.*, 97:31–145, 1983.
- [100] Torbjorn Sjostrand. Jet Fragmentation of Nearby Partons. *Nucl. Phys.*, B248:469–502, 1984.
- [101] Peter Zeiler Skands. Tuning Monte Carlo Generators: The Perugia Tunes. *Phys. Rev.*, D82:074018, 2010.
- [102] The ATLAS Collaboration. ATLAS Run 1 Pythia8 tunes. Technical Report ATL-PHYS-PUB-2014-021, CERN, Geneva, Nov 2014.
- [103] Torbjorn Sjostrand, Stephen Mrenna, and Peter Z. Skands. PYTHIA 6.4 Physics and Manual. *JHEP*, 05:026, 2006.
- [104] Torbjorn Sjostrand, Stephen Mrenna, and Peter Z. Skands. A Brief Introduction to PYTHIA 8.1. *Comput. Phys. Commun.*, 178:852–867, 2008.
- [105] G. Marchesini, B. R. Webber, G. Abbiendi, I. G. Knowles, M. H. Seymour, and L. Stanco. HERWIG: A Monte Carlo event generator for simulating hadron emission reactions with interfering gluons. Version 5.1 - April 1991. *Comput. Phys. Commun.*, 67:465–508, 1992.
- [106] J. Alwall, R. Frederix, S. Frixione, V. Hirschi, F. Maltoni, O. Mattelaer, H. S. Shao, T. Stelzer, P. Torrielli, and M. Zaro. The automated computation of tree-level

- and next-to-leading order differential cross sections, and their matching to parton shower simulations. *JHEP*, 07:079, 2014.
- [107] Simone Alioli, Paolo Nason, Carlo Oleari, and Emanuele Re. A general framework for implementing NLO calculations in shower Monte Carlo programs: the POWHEG BOX. *JHEP*, 06:043, 2010.
- [108] T. Gleisberg, Stefan Hoeche, F. Krauss, M. Schonherr, S. Schumann, F. Siegert, and J. Winter. Event generation with SHERPA 1.1. *JHEP*, 02:007, 2009.
- [109] Steffen Schumann and Frank Krauss. A Parton shower algorithm based on Catani-Seymour dipole factorisation. *JHEP*, 03:038, 2008.
- [110] D. J. Lange. The EvtGen particle decay simulation package. *Nucl. Instrum. Meth.*, A462:152–155, 2001.
- [111] The ATLAS Collaboration. The ATLAS Simulation Infrastructure. *Eur. Phys. J.*, C70:823–874, 2010.
- [112] S. Agostinelli et al. GEANT4: A Simulation toolkit. *Nucl. Instrum. Meth.*, A506:250–303, 2003.
- [113] The ATLAS Collaboration, M.Beckingham, M.Duehrssen, E.Schmidt, M.Shapiro, M.Venturi, J.Virzi, I.Vivarelli, M.Werner, S.Yamamoto, and T.Yamanaka. The simulation principle and performance of the ATLAS fast calorimeter simulation FastCaloSim. Technical Report ATL-PHYS-PUB-2010-013, CERN, Geneva, Oct 2010.
- [114] ATLAS Trigger Public Results. <https://twiki.cern.ch/twiki/bin/view/AtlasPublic/TriggerPublicResults>.
- [115] T. Cornelissen, M. Elsing, S. Fleischmann, W. Liebig, and E. Moyse. Concepts, Design and Implementation of the ATLAS New Tracking (NEWT). *ATL-SOFT-PUB-2007-007, ATL-COM-SOFT-2007-002*, 2007.

- [116] The ATLAS Collaboration. Vertex Reconstruction Performance of the ATLAS Detector at $\sqrt{s} = 13$ TeV. Technical Report ATL-PHYS-PUB-2015-026, CERN, Geneva, Jul 2015.
- [117] The ATLAS Collaboration. Electron and photon energy calibration with the ATLAS detector using LHC Run 1 data. *Eur. Phys. J.*, C74(10):3071, 2014.
- [118] The ATLAS Collaboration. Photon identification in 2015 ATLAS data. Technical Report ATL-PHYS-PUB-2016-014, CERN, Geneva, Aug 2016.
- [119] The ATLAS Collaboration. Electron efficiency measurements with the ATLAS detector using 2012 LHC proton-proton collision data. *Eur. Phys. J.*, C77(3):195, 2017.
- [120] The ATLAS Collaboration. Electron and photon energy calibration with the ATLAS detector using data collected in 2015 at $\sqrt{s} = 13$ TeV. Technical Report ATL-PHYS-PUB-2016-015, CERN, Geneva, Aug 2016.
- [121] ATLAS Trigger Public Results. <https://twiki.cern.ch/twiki/bin/view/AtlasPublic/ ElectronGammaPublicCollisionResults>.
- [122] The ATLAS Collaboration. Measurement of the photon identification efficiencies with the ATLAS detector using LHC Run-1 data. *Eur. Phys. J.*, C76(12):666, 2016.
- [123] The ATLAS Collaboration. Muon reconstruction performance of the ATLAS detector in proton-proton collision data at $\sqrt{s} = 13$ TeV. *Eur. Phys. J.*, C76(5):292, 2016.
- [124] ATLAS Muon Public Results. <https://twiki.cern.ch/twiki/bin/view/AtlasPublic/ MuonPerformancePublicPlots>.
- [125] Gavin P. Salam. Towards Jetography. *Eur. Phys. J.*, C67:637–686, 2010.

- [126] W Lampl, S Laplace, D Lelas, P Loch, H Ma, S Menke, S Rajagopalan, D Rousseau, S Snyder, and G Unal. Calorimeter Clustering Algorithms: Description and Performance. Technical Report ATL-LARG-PUB-2008-002. ATL-COM-LARG-2008-003, CERN, Geneva, Apr 2008.
- [127] The ATLAS Collaboration. Topological cell clustering in the ATLAS calorimeters and its performance in LHC Run 1. *Eur. Phys. J.*, C77:490, 2017.
- [128] Matteo Cacciari, Gavin P. Salam, and Gregory Soyez. The Anti- k_T jet clustering algorithm. *JHEP*, 04:063, 2008.
- [129] The ATLAS Collaboration. Jet Calibration and Systematic Uncertainties for Jets Reconstructed in the ATLAS Detector at $\sqrt{s} = 13$ TeV. Technical Report ATL-PHYS-PUB-2015-015, CERN, Geneva, Jul 2015.
- [130] The ATLAS Collaboration. Pile-up subtraction and suppression for jets in ATLAS. Technical Report ATLAS-CONF-2013-083, CERN, Geneva, Aug 2013.
- [131] The ATLAS Collaboration. Jet global sequential corrections with the ATLAS detector in proton-proton collisions at $\text{sqrt}(s) = 8$ TeV. Technical Report ATLAS-CONF-2015-002, CERN, Geneva, Mar 2015.
- [132] The ATLAS Collaboration. Data-driven determination of the energy scale and resolution of jets reconstructed in the ATLAS calorimeters using dijet and multijet events at $\sqrt{s} = 8$ TeV. Technical Report ATLAS-CONF-2015-017, CERN, Geneva, Apr 2015.
- [133] ATLAS JetEtMiss Public Results. <https://twiki.cern.ch/twiki/bin/view/AtlasPublic/JetEtmissPublicResults>.
- [134] The ATLAS Collaboration. Tagging and suppression of pileup jets with the ATLAS detector. Technical Report ATLAS-CONF-2014-018, CERN, Geneva, May 2014.
- [135] The ATLAS Collaboration. Performance of b -Jet Identification in the ATLAS Experiment. *JINST*, 11(04):P04008, 2016.

- [136] The ATLAS Collaboration. Performance and Calibration of the JetFitterCharm Algorithm for c-Jet Identification. Technical Report ATL-PHYS-PUB-2015-001, CERN, Geneva, Jan 2015.
- [137] Giacinto Piacquadio and Christian Weiser. A new inclusive secondary vertex algorithm for b-jet tagging in ATLAS. *J. Phys. Conf. Ser.*, 119:032032, 2008.
- [138] R. Fruhwirth. Application of Kalman filtering to track and vertex fitting. *Nucl. Instrum. Meth.*, A262:444–450, 1987.
- [139] L. Breiman, J. Friedman, R. Olshen, and C. Stone. *Classification and Regression Trees*. Wadsworth and Brooks, Monterey, CA, 1984.
- [140] Andreas Hoecker, Peter Speckmayer, Joerg Stelzer, Jan Therhaag, Eckhard von Toerne, and Helge Voss. TMVA: Toolkit for Multivariate Data Analysis. *PoS*, ACAT:040, 2007.
- [141] The ATLAS Collaboration. Optimisation of the ATLAS b -tagging performance for the 2016 LHC Run. Technical Report ATL-PHYS-PUB-2016-012, CERN, Geneva, Jun 2016.
- [142] The ATLAS Collaboration. Calibration of b -tagging using dileptonic top pair events in a combinatorial likelihood approach with the ATLAS experiment. Technical Report ATLAS-CONF-2014-004, CERN, Geneva, Feb 2014.
- [143] The ATLAS Collaboration. Calibration of the b -tagging efficiency for c jets with the ATLAS detector using events with a W boson produced in association with a single c quark. Technical Report ATLAS-CONF-2013-109, CERN, Geneva, Dec 2013.
- [144] The ATLAS Collaboration. Calibration of the performance of b -tagging for c and light-flavour jets in the 2012 ATLAS data. Technical Report ATLAS-CONF-2014-046, CERN, Geneva, Jul 2014.

- [145] The ATLAS Collaboration. Performance of missing transverse momentum reconstruction for the ATLAS detector in the first proton-proton collisions at $\sqrt{s} = 13$ TeV. Technical Report ATL-PHYS-PUB-2015-027, CERN, Geneva, Jul 2015.
- [146] The ATLAS Collaboration. Track Reconstruction Performance of the ATLAS Inner Detector at $\sqrt{s} = 13$ TeV. Technical Report ATL-PHYS-PUB-2015-018, CERN, Geneva, Jul 2015.
- [147] The ATLAS Collaboration. Early Inner Detector Tracking Performance in the 2015 data at $\sqrt{s} = 13$ TeV. Technical Report ATL-PHYS-PUB-2015-051, CERN, Geneva, Dec 2015.
- [148] The ATLAS Collaboration. Tracking Studies for b -tagging with 7 TeV Collision Data with the ATLAS Detector. Technical Report ATLAS-CONF-2010-070, CERN, Geneva, Jul 2010.
- [149] The ATLAS Collaboration. Studies of the ATLAS Inner Detector material using $\sqrt{s} = 13$ TeV pp collision data. Technical Report ATL-PHYS-PUB-2015-050, CERN, Geneva, Nov 2015.
- [150] The ATLAS Collaboration. Performance of the ATLAS Track Reconstruction Algorithms in Dense Environments in LHC Run 2. *Eur. Phys. J.*, C77(10):673, 2017.
- [151] The ATLAS Collaboration. Alignment of the ATLAS Inner Detector with the initial LHC data at $\sqrt{s} = 13$ TeV. Technical Report ATL-PHYS-PUB-2015-031, CERN, Geneva, Jul 2015.
- [152] The ATLAS Collaboration. Study of alignment-related systematic effects on the ATLAS Inner Detector tracking. Technical Report ATLAS-CONF-2012-141, CERN, Geneva, Oct 2012.
- [153] The ATLAS Collaboration. Jet energy scale measurements and their systematic uncertainties in proton-proton collisions at $\sqrt{s} = 13$ TeV with the ATLAS detector. *Phys. Rev.*, D96(7):072002, 2017.

- [154] The ATLAS Collaboration. Jet energy resolution in proton-proton collisions at $\sqrt{s} = 7$ TeV recorded in 2010 with the ATLAS detector. *Eur. Phys. J.*, C73(3):2306, 2013.
- [155] The ATLAS Collaboration. Identification of high transverse momentum top quarks in pp collisions at $\sqrt{s} = 8$ TeV with the ATLAS detector. *JHEP*, 06:093, 2016.
- [156] Christoph Borschensky, Michael Krämer, Anna Kulesza, Michelangelo Mangano, Sanjay Padhi, Tilman Plehn, and Xavier Portell. Squark and gluino production cross sections in pp collisions at $\sqrt{s} = 13, 14, 33$ and 100 TeV. *Eur. Phys. J.*, C74(12):3174, 2014.
- [157] Daniele Alves et al. Simplified Models for LHC New Physics Searches. *J.Phys.*, G39:105005, 2012.
- [158] The ATLAS Collaboration. ATLAS Run 1 searches for direct pair production of third-generation squarks at the Large Hadron Collider. *Eur. Phys. J.*, C75(10):510, 2015. [Erratum: Eur. Phys. J.C76,no.3,153(2016)].
- [159] R. Gröber, Margarete M. Mühlleitner, E. Popenda, and A. Wlotzka. Light Stop Decays: Implications for LHC Searches. *Eur. Phys. J.*, C75:420, 2015.
- [160] C. Patrignani et al. Review of Particle Physics. *Chin. Phys.*, C40(10):100001, 2016.
- [161] Leif Lönnblad and Stefan Prestel. Merging Multi-leg NLO Matrix Elements with Parton Showers. *JHEP*, 03:166, 2013.
- [162] Tanju Gleisberg and Stefan Hoeche. Comix, a new matrix element generator. *JHEP*, 12:039, 2008.
- [163] Fabio Cascioli, Philipp Maierhofer, and Stefano Pozzorini. Scattering Amplitudes with Open Loops. *Phys. Rev. Lett.*, 108:111601, 2012.

- [164] Stefan Hoeche, Frank Krauss, Marek Schonherr, and Frank Siegert. QCD matrix elements + parton showers: The NLO case. *JHEP*, 04:027, 2013.
- [165] Stefano Catani, Leandro Cieri, Giancarlo Ferrera, Daniel de Florian, and Massimiliano Grazzini. Vector boson production at hadron colliders: a fully exclusive QCD calculation at NNLO. *Phys. Rev. Lett.*, 103:082001, 2009.
- [166] Michal Czakon and Alexander Mitov. Top++: A Program for the Calculation of the Top-Pair Cross-Section at Hadron Colliders. *Comput. Phys. Commun.*, 185:2930, 2014.
- [167] Nikolaos Kidonakis. Next-to-next-to-leading-order collinear and soft gluon corrections for t-channel single top quark production. *Phys. Rev.*, D83:091503, 2011.
- [168] Nikolaos Kidonakis. NNLL resummation for s-channel single top quark production. *Phys. Rev.*, D81:054028, 2010.
- [169] Nikolaos Kidonakis. Two-loop soft anomalous dimensions for single top quark associated production with a W- or H-. *Phys. Rev.*, D82:054018, 2010.
- [170] The ATLAS Collaboration. Improved luminosity determination in pp collisions at $\sqrt{s} = 7$ TeV using the ATLAS detector at the LHC. *Eur. Phys. J.*, C73(8):2518, 2013.
- [171] The ATLAS Collaboration. Electron efficiency measurements with the ATLAS detector using the 2015 LHC proton-proton collision data. Technical Report ATLAS-CONF-2016-024, CERN, Geneva, Jun 2016.
- [172] The ATLAS Collaboration. Measurement of the cross section for the production of a W boson in association with b^- jets in pp collisions at $\sqrt{s} = 7$ TeV with the ATLAS detector. *Phys. Lett.*, B707:418–437, 2012.
- [173] M. Bahr et al. Herwig++ Physics and Manual. *Eur. Phys. J.*, C58:639–707, 2008.

- [174] Stefan Gieseke, Christian Rohr, and Andrzej Siodmok. Colour reconnections in Herwig++. *Eur. Phys. J.*, C72:2225, 2012.
- [175] The ATLAS Collaboration. Multi-Boson Simulation for 13 TeV ATLAS Analyses. Technical Report ATL-PHYS-PUB-2016-002, CERN, Geneva, Jan 2016.
- [176] Lorenzo Moneta, Kevin Belasco, Kyle S. Cranmer, S. Kreiss, Alfio Lazzaro, Danilo Piparo, Gregory Schott, Wouter Verkerke, and Matthias Wolf. The RooStats Project. *PoS*, ACAT2010:057, 2010.
- [177] R. Brun and F. Rademakers. ROOT: An object oriented data analysis framework. *Nucl. Instrum. Meth.*, A389:81–86, 1997.
- [178] M. Baak, G. J. Besjes, D. Côte, A. Koutsman, J. Lorenz, and D. Short. HistFitter software framework for statistical data analysis. *Eur. Phys. J.*, C75:153, 2015.
- [179] G. Cowan. *Statistical Data Analysis*. Oxford science publications. Clarendon Press, 1998.
- [180] Glen Cowan. Statistics for Searches at the LHC. In *Proceedings, 69th Scottish Universities Summer School in Physics : LHC Phenomenology (SUSSP69): St.Andrews, Scotland, August 19-September 1, 2012*, pages 321–355, 2013.
- [181] Glen Cowan, Kyle Cranmer, Eilam Gross, and Ofer Vitells. Asymptotic formulae for likelihood-based tests of new physics. *Eur. Phys. J.*, C71:1554, 2011. [Erratum: *Eur. Phys. J.*C73,2501(2013)].
- [182] Robert D. Cousins, James T. Linnemann, and Jordan Tucker. Evaluation of three methods for calculating statistical significance when incorporating a systematic uncertainty into a test of the background-only hypothesis for a poisson process. *Nucl. Inst. and Methods in Physics Research Section A*, 595(2):480 – 501, 2008.
- [183] Alexander L. Read. Presentation of search results: The CL(s) technique. *J. Phys.*, G28:2693–2704, 2002.

- [184] Alan Barr, Christopher Lester, and P. Stephens. $m(T2)$: The Truth behind the glamour. *J.Phys.*, G29:2343–2363, 2003.
- [185] C.G. Lester and D.J. Summers. Measuring masses of semiinvisibly decaying particles pair produced at hadron colliders. *Phys.Lett.*, B463:99–103, 1999.